Universitat Ramon Llull

Ionospheric effects of the 20 November 2003 geomagnetic storm observed from GPS, ground-based and satellite data

Estefania Blanch Llosa

June 2007

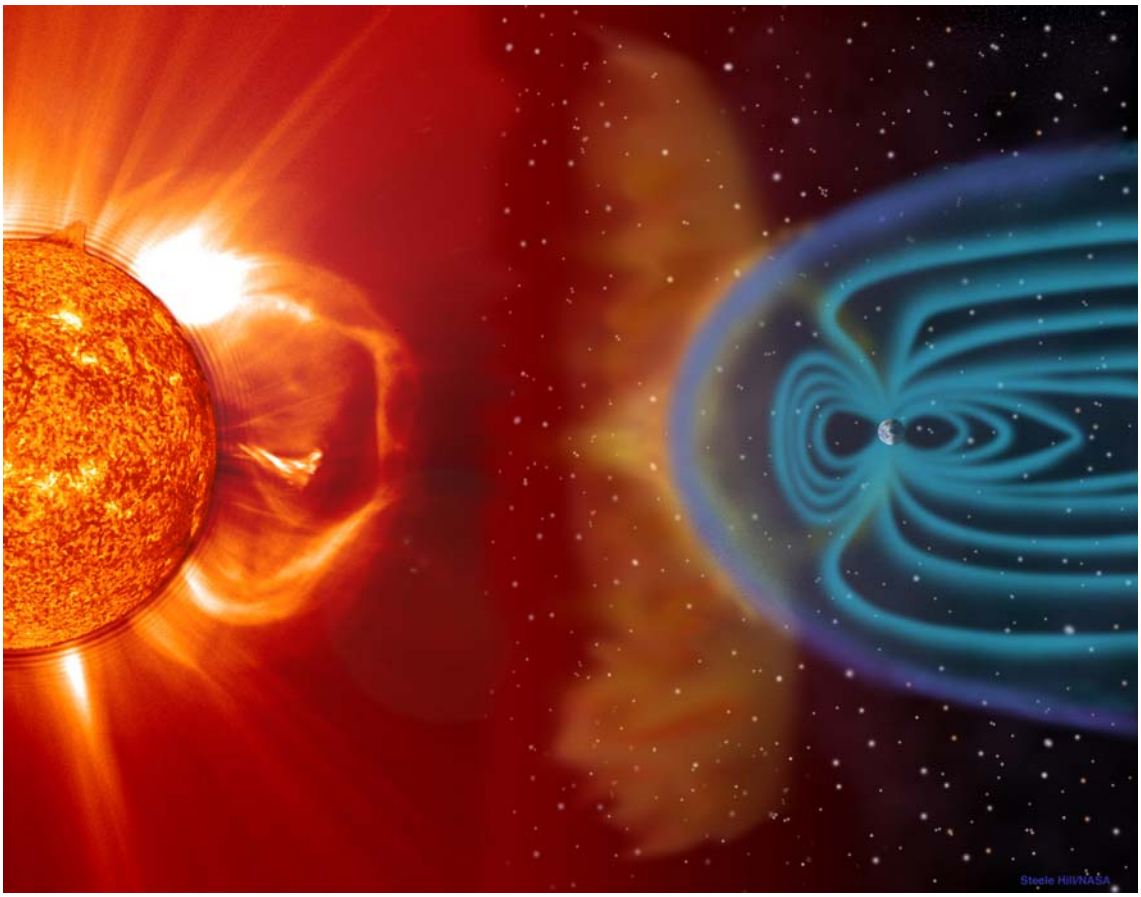

Academic advisors:

Dr. David Altadill

Dr. Juan José Curto

Ionospheric effects of the 20 November 2003 geomagnetic storm observed from GPS, ground-based and satellite data

Estefania Blanch Llosa

June 2007

Individual Research Report submitted to the Ramon Llull University in fulfilment of the requirements for the Diploma of Advanced Studies

Cover image: A composite of Space Weather images comprising a SOHO satellite image of an erupting coronal mass ejection and a simulation of the Earth magnetosphere. Image courtesy of SOHO project.

Academic advisors:

Dr. David Altadill

Dr. Juan José Curto

ACKNOWLEDGEMENTS

This work has been supported by the Spanish project REN2003-08376-C02-02 and partially by the Marie Curie Training Site fellowship HPMT-CT-2001-00229.

I want to acknowledge the constant advice of David Altadill and Juan José Curto from the Ebre Observatory, the contribution of Joseph Boška and Dalia Burešová from the Institute of Atmospheric Physics Czech Republic and Manuel Hernández-Pajares from the Universitat Politècnica de Catalunya. The advice of Arnaud Chulliat during my internship in the Institut de Physique du Globe de Paris and Miquel Torta from the Ebre Observatory for his advice and comments in some parts of the work.

I want to acknowledge Maria Genescà and Maria José Blanca from the Ebre Observatory library for their help in the bibliographic research, Gonzalo Sánchez to manually scale the Ebre Observatory ionograms and P. Luis Alberca from the Ebre Observatory and Ivan Kutiev from the Bulgarian Geophysical Institute for their very useful discussion.

I want to acknowledge the institutions for maintaining geomagnetic and ionospheric observatories and their staff for providing data. The Danish Meteorological Institute Atmosphere Space Research Division for providing the equivalent ionospheric current model and the operational support of the CHAMP mission by the German Aerospace Center (DLR).

ABSTRACT

Intense late-cycle solar activity during November 2003 produced a very strong geomagnetic storm on 20 November 2003 which reached intense geomagnetic activity levels. The aim of this work is to discuss the significant effects observed on the ionosphere over the mid-latitude European sector produced during the geomagnetic storm using data from ground-based European ionosondes, ground-based GPS receivers, ground-based magnetometers and geomagnetic models. These effects are the presence of well developed particle E layer observed at latitudes as low as 37ºN, the uplift and spread of the F region, the presence of two thin belts over the mid-latitude European evening sector one having enhanced electron content and other depressed electron content and the evidence of the equatorward expansion of the auroral oval leading with the observation of the eastward auroral electrojet at latitudes as low as 55ºN.

INTRODUCTION

Geomagnetic storms are the most important Space Weather phenomena from the point of view of the impact on the global magnetosphere-thermosphere-ionosphere system. The storm is supplied by solar wind energy, captured by the magnetosphere, and transformed and dissipated in the high latitude upper atmosphere. It affects the complex morphology of the electric currents, winds, temperature and neutral composition, and it causes changes in the state of ionospheric ionization. Studies of the ionospheric reaction to geomagnetic storms are of great importance because they can impact ground and space based technological systems such as Global Navigation Satellite Systems (GNSS). There are numerous publications on the topic (e.g. Buonsanto, 1999; Danilov, 2001; Lastovička, 2002; Mansilla, 2004) but many features of this phenomenon are still not clear due to big number of different processes interacting in the Earth's atmospheric system.

The great geomagnetic storm occurred on 20 November 2003 was large enough to produce numerous disturbances in the Earth's magnetosphere, thermosphere and ionosphere. The objective of this study is to observe the effects of this very strong geomagnetic storm from ground-based ionosondes to study the variations on the ionospheric vertical structure, from ground-based GPS receivers to study the variation of the Total Electron Content and from ground-based magnetometers and geomagnetic models to study the dynamics of magnetospheric and ionospheric currents. Possible physical mechanisms responsible of these effects are also explained.

Chapter 1 is an introduction to the Solar-Terrestrial physics to understand the drivers of the geomagnetic storms. Chapter 2 is an introductory part dealing with the ionosphere: formation, regions, currents and observation and in chapter 3 the response of the ionosphere during geomagnetic storms is explained. The whole chapter 4 is dedicated to the study of the effects on the ionosphere during the 20 November 2003 geomagnetic storm. It is divided in different sections. In sections 4.1 and 4.2, the data used in the study and the method to process it are described. In section 4.3 the observation of the effects of this geomagnetic storm on the ionosphere observed from different instruments are described with great detail. In section 4.4 possible physical mechanisms responsible of the different effects are discussed. Finally, in chapter 5 conclusions extracted from this study and next steps to follow can be found.

CHAPTER 1: SOLAR - TERRESTRIAL PHYSICS

The solar-terrestrial environment includes the upper part of the terrestrial atmosphere, the outer part of the geomagnetic field and the solar emissions that affect them. The purpose of this section is to summarize points of solar-terrestrial physics starting from the Sun, the solar activity and the magnetosphere in order to understand the mechanisms that generate geomagnetic storms.

1.1 The Sun and solar activity

The Sun is composed mainly of hydrogen (about 92.1%) and helium (7.8%) together with small traces of heavier elements. Solar energy is created deep within the core, where thermonuclear reactions take place due to high pressure and temperature. The dominant process consists of chain reactions called the proton-proton chain where four protons fuse to create a helium nucleus (Phillips, 1992). The energy generated in the core (due to the mass difference) is transported outward by photons in the radiation zone of the Sun, which covers the region between 0.15 and 0.7 solar radii (Scherer et al., 2005). At about 0.7 solar radii at a temperature of $T \approx 2 \cdot 10^6 K$, convection takes over as the dominant mechanism of energy transport. The region between 0.7 and 1 solar radius is thus called the solar convection zone (see figure 1).

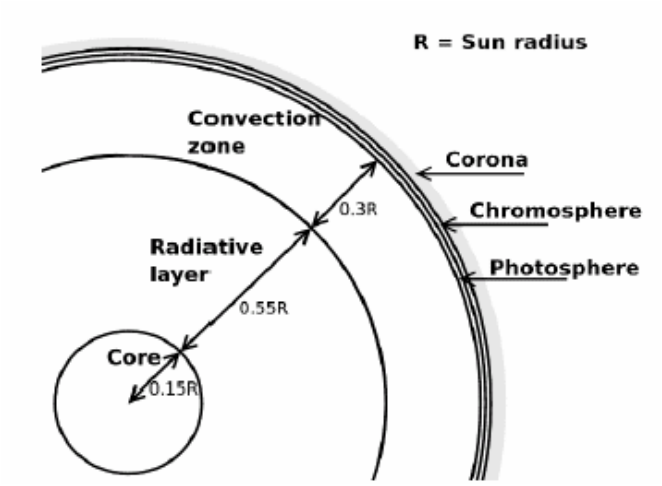

Figure 1. Structure of the Sun. Figure obtained from Space Weather Observation, Research and Distribution, 2006

The solar photosphere is the layer at which the gas becomes opaque to photons and constitutes the visual surface. It has a temperature of about 6000 K, and represents the top of the convection zone. It is covered with a granular pattern that results from the convection cells below the surface. Other important features of the photosphere are sunspots, which are lower temperature zones with intense magnetic fields that accelerate charged particles during solar flares. Above the photosphere, a thick visually transparent layer called chromosphere extends for 2500 km (Phillips, 1992).

Sunspots are regions with a magnetic field stronger than the average $(\Delta \approx 0.4T)$ (Prölss, 2004). The magnetic field inhibits convection and allows the temperature of the sunspots to become lower and appear darker than the surroundings (Kivelson and Russel, 1995). The average sunspot lifetime is 10 days, while size varies from 300 km to 100000 km. No more than about 1% of the Sun's surface is covered by sunspots at any given time (Phillips, 1992).The number of sunspots varies over an approximate 11 year cycle (figure 2) and it is an indication of the overall solar activity. Total solar irradiance follows this cycle, where maximum solar activity corresponds to the peaks of sunspot number.

A solar flare is defined as a sudden release of energy appearing as electromagnetic radiation; from radio waves to X-rays and gamma-rays. Flares occur near active regions (sunspots) when magnetic energy has built up in the solar atmosphere. Particles, including electrons, protons, and heavy nuclei, are heated and accelerated in the solar atmosphere (Prölss, 2004). According to their X-ray brightness in the wavelength range from 1 to 8 Å, solar flares can be classified as X-class, M-class and C-class from more to less energetic. Each class has nine subdivisions ranging from, e.g., C1 to C9, M1 to M9 and X1 to X9.

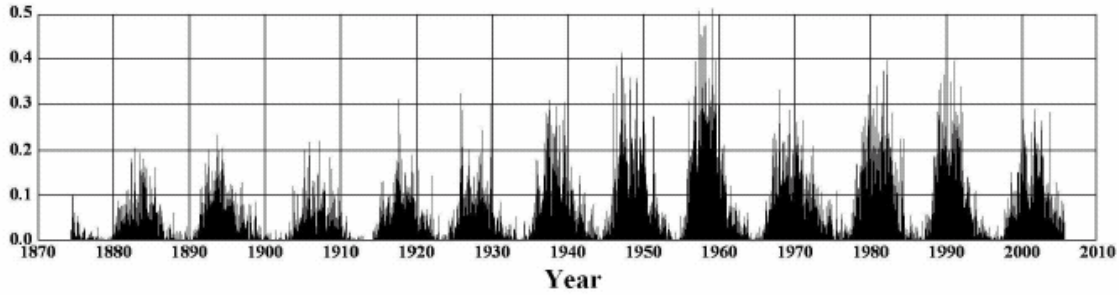

Figure 2. Average daily sunspot area (% of visible hemisphere) as a function of time. Figure obtained from Space Weather Observation, Research and Distribution, 2006.

The solar corona is the outermost atmosphere of the Sun. Coronal gas normally has a temperature of a few million Kelvin, much higher than for the photosphere, which constitutes one of the biggest mysteries about the Sun. It has a typical density of 10^{15} particles/m^3 and it is the region where prominences appear (Phillips, 1992). These are immense clouds of glowing gas, usually associated with regions of sunspot activity that erupt from the upper chromosphere and can result in a Coronal Mass Ejection (CME).

A CME consist of very large structure containing plasma and magnetic fields that are expelled from the Sun and are generally associated with regions of sunspot activity. The ejection speed have a wide range, from 50 km/s for events associated to solar minimum to more that 1000 km/s for the most energetic events (normally associated with solar maximum) (Prölss, 2004). The latter gives a travel time of approximately 42 hours to reach the Earth orbit.

1.2 Solar Wind and Interplanetary Magnetic Field

Solar wind originates in the corona and is an outwardly expanding plasma, essentially consisting of protons and electrons, with small amounts of other ions. It is considered to be the result of a huge difference in gas pressure between the solar corona and interplanetary space, which drives plasma outward despite the restraining influence of solar gravity (Prölss, 2004). Table 1 shows some selected mean properties of solar wind at Earth's orbit.

The solar wind carries with it a weak magnetic field of a few nanoteslas. The field is "frozen in" to the plasma because the electrical conductivity is very large

and the plasma controls the motion of the total magnetoplasma. Although the solar wind flows out almost radially from the Sun, the solar rotation gives the magnetic field a spiral form and at the orbit of the Earth, the field lines run at about 45º to the radial direction. This magnetic field is called Interplanetary Magnetic Field (IMF) (Prölss, 2004).

Table 1. Mean properties of the solar wind at the Earth's orbit (adapted from Prölss, 2004).

Parameter	**Mean value**	**Range**
Composition	96% H^+, 4% (0-20%) He^{++}, e^-	
Density	6 particles/cm^3	0.1-100 particles/cm^3
Velocity	470 km/s	170-2000 km/s
Proton Flux	$3 \cdot 10^{12}$ particles/m^2s	
Energy Flux	0.5 mW/m^2	
Temperature	10^5 K	3500-$5 \cdot 10^5$ K
Particle energy proton	1.1 keV (flow energy)	
Particle energy electron	13 keV (thermal energy)	

1.3 Magnetosphere

As it approaches the Earth, the solar wind interacts with the terrestrial magnetic field compressing the sun-side and creating a long comet-like magnetic tail on the night side. The Earth magnetic field is generated by the rotation of plasma in the Earth's liquid iron-nickel core (Merrill et al., 1996). The volume dominated by the geomagnetic field is called Earth's magnetosphere (figure 3). It acts as a gigantic shield around the Earth by forcing charged particles to flow around the Earth and slow down. The geomagnetic field confines charged particles depending on their energies into either the Van Allen radiation belts or the ring current. The Van Allen belts confine the high energy component of this particle population, where the lowest energies are 1 MeV for protons and 50 keV for electrons. One inner and one outer belt encircle the Earth with a higher concentration of protons and electrons respectively. The ring current consists of a particle population of medium energy confined to the inner magnetosphere (between 2 to 7 earth radii) in the equatorial plane. Ion energies are typically 1-200 keV whereas electron energies are about one order of magnitude lower.

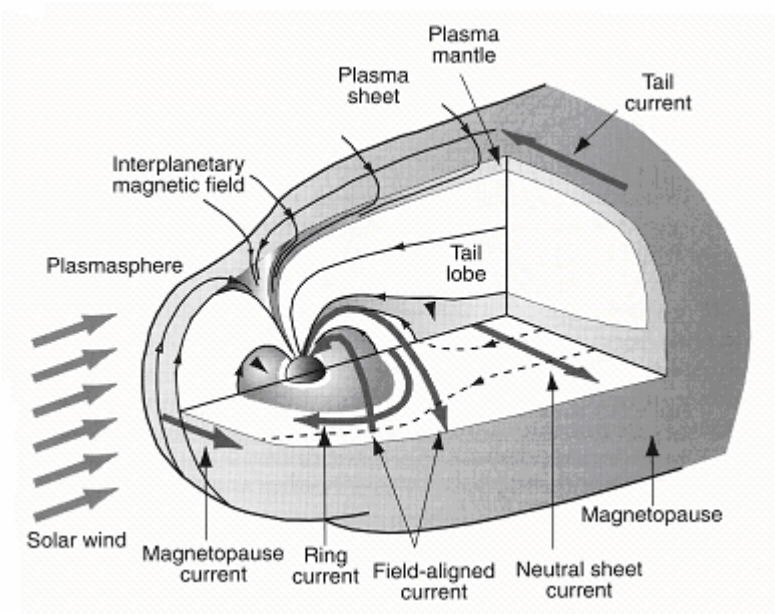

Figure 3. Three dimensional schematic view of the magnetosphere. Image modified from Gombosi 1998.

1.4 Geomagnetic storms

When a CME hits the Earth, the magnetosphere is compressed further and solar particles can penetrate the Earth's atmosphere, mainly in the magnetic polar areas. As first suggested by Dungey (1961), the orientation of the Z component of the IMF has an important influence on the magnetosphere and high-latitude ionosphere as it controls the fraction of the energy in the solar wind flow that can penetrate in the magnetosphere. When Bz is strongly negative, magnetic reconnection between the IMF and the geomagnetic field produces open field lines (see figure 4) which allows energetic particles to be transferred from the solar wind to the Earth's magnetosphere. These particles increase the density of the ring current which creates a magnetic field in the direction opposite to that of the Earth's magnetic field and thus weakens the total magnetic field.

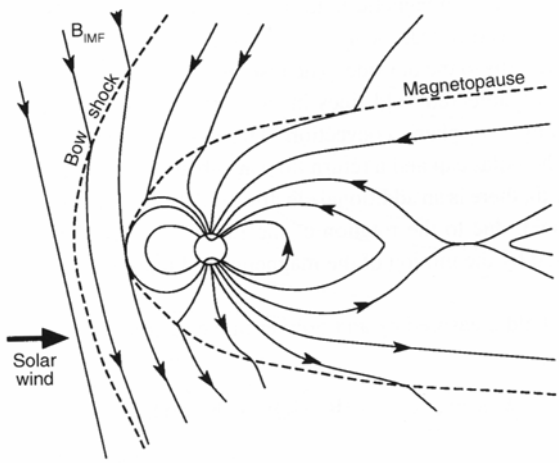

Figure 4. Magnetic field lines reconnection. Figure modified from Gombosi 1998

Such geomagnetic fluctuations are called geomagnetic storms and lead to effects on the magnetosphere-thermosphere-ionosphere system that can affect ground and space infrastructure (Prölss, 2004).

Geomagnetic fluctuations due to geomagnetic storms are observed by ground-based magnetometers and although no two storms are identical it is possible to distinguish three phases: the initial phase, the main phase and the recovery phase. The initial phase is defined as a sudden increase of the magnetic field (Storm Sudden Commencement, SSC) due to the compression of the magnetosphere by the interplanetary shock wave followed by an increase of the magnetic field. This initial phase is not always observed and it last until the IMF Bz turns southward. Once the IMF Bz turns southward, the main phase of the storm starts. During the main phase of the storm, the density of the ring current increases and produces a large decrease in the horizontal component of the magnetic field (Parkinson, 1983). The recovery phase is attributed to the ring current decay (Prölss, 2004) and the total magnetic field returns to its original values. In figure 5 it is shown the three phases of a geomagnetic storm.

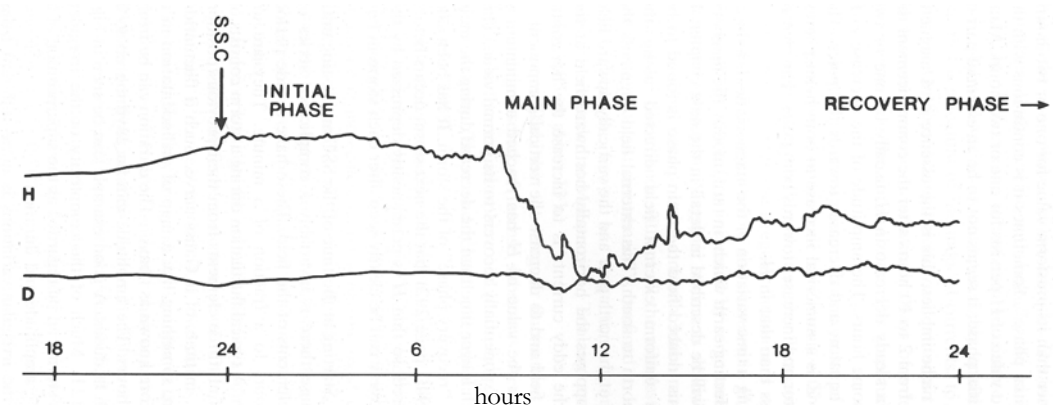

Figure 5. Geomagnetic storm showing all the phases. Figure modified from Parkinson, 1983.

The reduction of the geomagnetic horizontal component due to the ring current effect is expressed by the Dst index which is very useful as an indicator of the intensity and duration of a geomagnetic storm. It is derived from low-latitude magnetograms, in units of nT with a resolution of 1 minute (Hargreaves, 1992). Another useful indicator of geomagnetic activity is the Kp index; which give a measure of the global geomagnetic disturbance in a three hour interval in a

quasi-logarithmic scale. It ranges from 0 to 9 being Kp=5 the level to define a geomagnetic storm. Ap index is derived directly from Kp index to obtain a linear scale of the disturbance. Using Ap index, the level to define a geomagnetic storm is Ap=30 nT (Parkinson, 1983). There are other many indices that indicate the geomagnetic activity at different latitudes. In section 2.3 there are defined the indices that define the magnetic activity at high latitudes. For more information about geomagnetic indices see the International Service of Geomagnetic Indices (http://isgi.cetp.ipsl.fr/).

CHAPTER 2: THE IONOSPHERE

The first suggestions of the existence of a conducting layer in the upper atmosphere go back to the 19th century but the interest doesn't start until 1901 when Marconi first succeeded in transmitting radio waves across the Atlantic. This fact was explained independently by Kennelly, Heavisade and Londge in 1902 as the reflection of the electromagnetic waves from free charge carriers in the upper atmosphere. Since that time the ionosphere has been extensively studied and most of its principal features, though not all, are now fairly well understood in terms of the physical and chemical processes of the upper atmosphere.

Nowadays, the ionosphere is defined as the ionized part of the upper atmosphere (60-2000 km even if the upper limit is not well established) which contains significant numbers of free electrons and positive ions. The medium as a whole is electrically neutral, there being equal numbers of positive and negative charges within a given volume. Although the charged particles are a minority amongst the neutral ones, they have an important influence on the medium's electrical properties influencing the electromagnetic waves propagation (Prölss, 2004).

2.1 Formation

The ionosphere is formed by the ionization of atmospheric gases such as N_2, O_2 and O. At middle and low latitude the energy required comes from solar radiation in the extreme ultraviolet (EUV) and X-ray parts of the spectrum. Once formed, the ions and electrons tend to recombine and to react with other gaseous species to produce new ions. Thus there is a dynamic equilibrium in which the net concentration of free electrons (electron density, N) depends on the relative speed of the production and loss processes. In general terms the rate of change of the electron density is expressed by the continuity equation:

$$\frac{\partial N}{\partial t} = q - L - div(n\vec{v}) \tag{1}$$

where *q* is the ion production rate, *L* is the loss rate by recombination and $div(n\vec{v})$ expresses the loss of electrons by movement, being $\vec{v}$ their mean drift velocity (Hargreaves, 1992).

2.1.1 Ion production rate (q)

The ion production rate can be expressed as

$$q = \eta \sigma n I \tag{2}$$

where I is the intensity of ionizing radiation at some level of the atmosphere and n is the concentration of atoms or molecules capable of being ionized by that radiation, σ is the amount of radiation absorbed by the atom or molecule to be ionized (absorption cross-section) and η is the fraction of the absorbed radiation that goes into producing ionization (ionization efficiency). From eq. 2 it is reasonable to predict that during the day, when the intensity of ionizing radiation varies with the elevation of the Sun, the electron density responds and at night, when the source of radiation is removed, the electron density decays producing the diurnal variation.

Assuming that the concentration of ionizable gas reduces with increasing height ($n = n_0 e^{-z}$) while the intensity of ionizing radiation increases ($I = I_\infty e^{-\tau}$), the ion production rate presents a maximum at some altitude (figure 6).

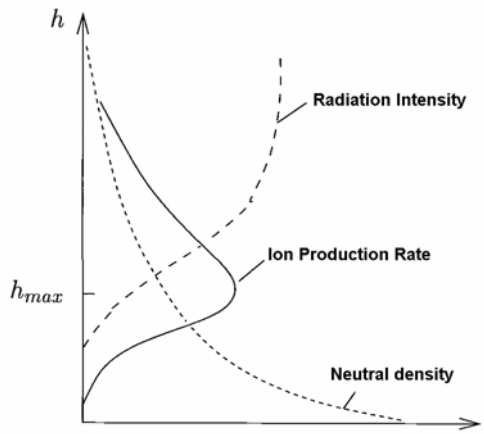

Figure 6. Ion production rate with altitude.
Figure modified from Prölss 2004.

This ion production rate profile is known as the Chapman production function and determines an approximation for the vertical electron density profile (equation 3) (Hargreaves, 1992).

$$q = q_{m0} \exp(1 - z - \sec\chi \cdot e^{-z}) \tag{3}$$

where $z = {(h - h_{mo})}/{H}$ is the reduced altitude of the neutral gas, $H = KT / mg$ is the scale height (see section 2.1.3) and h_{mo} is the height of maximum production rate when the Sun is overhead), q_{m0} is the maximum ionization rate (at h_{mo}) and χ is the zenith angle of the incoming solar radiation. The derivation of the Chapman production function also assumes that the atmosphere is composed of a single species exponentially distributed with constant scale height, the atmosphere is plane stratified, solar radiation is absorbed in proportion to the concentration of gas particles (eq. 2) and the absorption coefficient is constant (monochromatic radiation).

From eq. 3 it is possible to see that the first term is a constant, the second expresses the height variation of the density of ionizable atoms, and the third is proportional to the intensity of the ionizing radiation. Where z is large and positive the ion production rate become independent of χ and it decreases with height due to the reducing density of the neutral atmosphere ($q \rightarrow q_{m0} e \cdot e^{-z}$). In the region bellow the peak, where z is large and negative, the last term of eq. 3 dominates and the ion production rate depends on the solar zenith angle (χ) and both, the bottomside profile and the peak are displaced upward and to the left as χ increases as it is shown in figure 7. This fact has an influence on the daily variation.

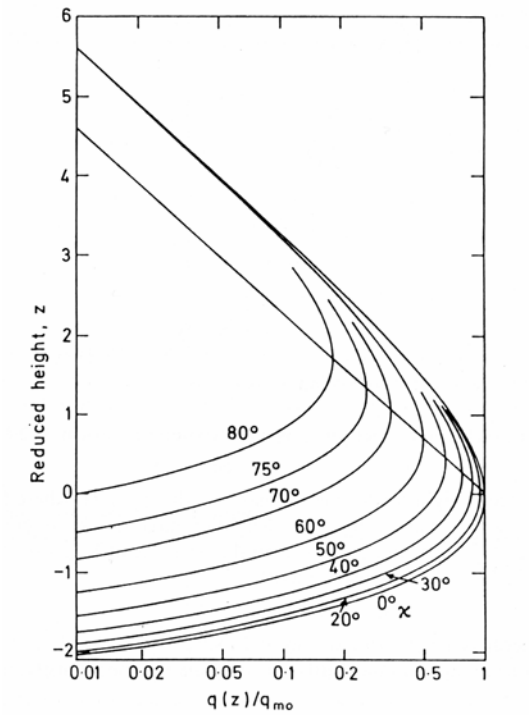

Figure 7. Chapman production function for different solar zenith angles. Figure obtained from Hargreaves 1992.

Another source of ionization it the precipitation of the energetic particles, which are not entirely absent at middle latitudes but are much more important at high latitudes where they provide the dominant source of ionization. Two very significant sources at high latitude are electrons associated with the aurora and protons emitted from the Sun during some solar flares. Depending on the initial energy, the electrons are stopped at different altitudes of the ionosphere as can be seen from figure 8.

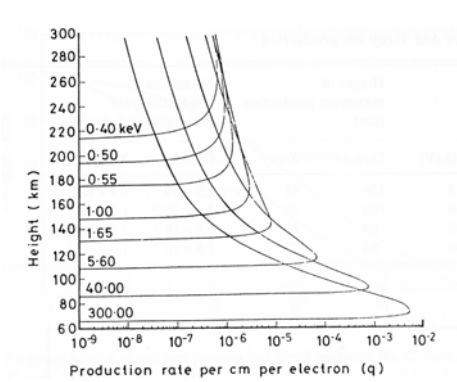

Figure 8. Production rates due to monoenergetic electrons of various initial energies. Figure obtained from Hargreaves 1992.

Energetic protons released from the Sun during a solar flare are more energetic than the auroral electrons. They collide with the atmospheric gas, principally with that of the mesosphere, and leave ionized trails with a concentration of the ionization toward the end of the path. This fact happens below 100 km of altitude with a maximum of the production rate depending on the initial energy of the protons; being maximum at low altitudes (20 km) for high energetic protons (300 MeV) (Hargreaves, 1992).

2.1.2 Loss rate by recombination (L)

The second term of the continuity equation (eq. 1) gives the loss rate of the free electrons by recombination processes. Where no negative ions are present in the ionosphere, the rate of electron loss is:

$$L = \alpha \left[X^{+}\right] N_e = \alpha N_e^{\ 2} \tag{4}$$

where N is the electron density (equal to the ion density $\left[X^{+}\right]$) and α is the recombination coefficient. At the equilibrium, taking the Chapman ion production rate, the electron density is expressed as:

$$N = N_{m0} \exp \tfrac{1}{2}(1 - z - \sec \chi \cdot e^{-z}) \tag{5}$$

A layer with these proprieties (no negative ions are present), is called $\alpha - Chapman$ layer.

In the lower ionosphere, there are a significant number of negative ions. In this case, the negative and positive ions may also recombine with each other and the electron loss rate can be written as

$$L = \alpha_e N_e N_+ + \alpha_i N_- N_+ = (1 + \lambda)(\alpha_e + \lambda \alpha_i) N_e^2 \tag{6}$$

α_e and α_i are the recombination coefficient for the reactions of positive ions with electrons and negative ions respectively, λ is the ratio between negative ion and electrons concentrations and to be electrically neutral, $N_+ = N_e + N_-$. Comparing eq. 6 with eq. 4, it is possible to see that even with presence of negative ions the electron loss rate is still proportional to N_e^2 with different magnitude. In this case, the term $(1+\lambda)(\alpha_e + \lambda\alpha_i)$ is called the effective recombination coefficient (Hargreaves 1992).

Another type of electron loss process is the attachment to neutral particles to form negative ions. This process becomes dominant at the highest levels of the ionosphere and the electron loss rate can be written as:

$$L = \beta N_e \tag{7}$$

where β is the attachment coefficient. In this case, the electron loss rate is linear with N_e. At the equilibrium and taking the Chapman ion production rate, the electron density is expressed as

$$N = N_{m0} \exp(1 - z - \sec\chi \cdot e^{-z}) \tag{8}$$

A layer with these properties is called $\beta - Chapman$ layer. β is expected to vary with height because it depends on the concentration of the neutral molecules. This has important consequences for the form of the ionosphere. The change from α to β behavior occurs at height h_t where

$$\beta(h_t) = \alpha N \tag{9}$$

(Hargreaves 1992).

2.1.3 Loss rate by movement ($div(n\vec{v})$)

The final term of the continuity equation (eq. 1) gives the changes of electron and ion density at a given location due to the movement of the plasma. This movement can be due to density gradients, gravity influence, collisions, and the effects of an electric and magnetic field. In this section it is explained the movement of the plasma due to the influence of the density gradients and gravity; which is called plasma diffusion. Later on, in section 2.3 it is explained in more detail the movement of the ionospheric plasma due to electric and magnetic fields.

Molecules of a gas move down due to the influence of the gravity until the pressure is equalized by the expansion flux due to density gradient. This fact gives a scale height of

$$H = {kT}/{mg} \tag{10}$$

From eq. 10 it is possible to see that the scale height is inversely proportional to the particle mass. As a result, light gases fall off with increasing altitude much more slowly than heavy gases (see He and H in figure 10). If there is a gas mixture consisting of a primary gas and a secondary gas and the primary gas reaches the equilibrium before the minority gas, the last one exhibits a density gradient in the negative z-direction due to the collisions with the majority one and a diffusion flux flows in the direction of increasing altitude as it is shown in figure 9. At any moment, the net velocity is proportional to the density gradient:

$$w = -\frac{D}{N}\frac{\partial N}{\partial h} \tag{11}$$

where $D = {kT}/{mv}$ is the diffusion coefficient (being v the collision frequency) (Prölss, 2004).

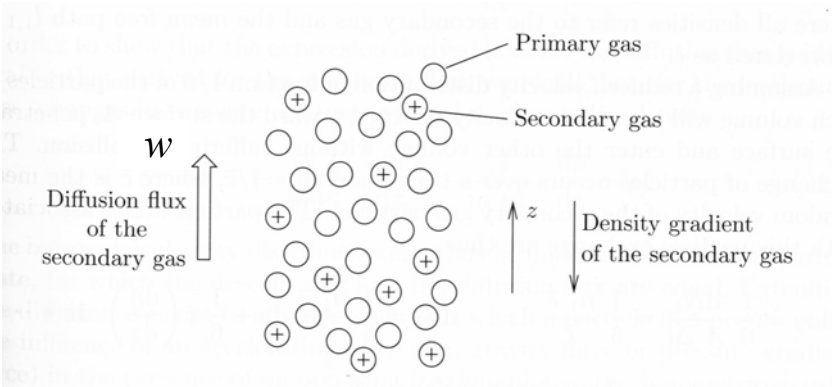

Figure 9. Simple figure scenario where primary and secondary gas particles are assumed to have the same properties. Figure modified from Prölss, 2004.

In the ionosphere, the minority gas is the plasma composed of ions and electrons, and the majority gas is the neutral air and it complicates the whole thing. Initially the ions tend to settle away from the electrons, but the resulting separation of opposite charges produces an electric field E and, as a consequence, a restoring force eE on each charged particle affecting the drift of the plasma. Taking into account the gravity force, the electrostatic force and diffusion and assuming that $m_e << m_i$, $m_e v_e << m_i v_i$, $N_e = N_i = N$ and $w_e = w_i = w$ give a net velocity:

$$w = -\frac{D_p}{N}\left(dN/dh + N/H_p \right) \tag{12}$$

where $D_p = k(T_e + T_i)/m_i v_i$ is now the ambipolar or plasma diffusion coefficient and $H_p = k(T_e + T_i)/m_i g$ is the plasma scale height (Hargreaves, 1992). Thus, the effect of electrons adds an extra term to the ion scale height increasing the plasma scale height. If the ion and electron temperatures are equal, the plasma scale height is twice the scale height of a neutral gas (Gombosi, 1998).

2.2 Regions of the ionosphere

Depending on the neutral composition and the source of ionization, the ionosphere is divided into different regions. As it is shown in figure 10, for a typical temperature profile of 1000 K, molecular nitrogen dominates below 180 km, atomic oxygen becomes the main specie at altitudes between 180 and 700 km, helium takes over in the range from 700 to 1700 km and atomic hydrogen at higher altitudes (not shown here) (Prölss 2004). It is important to point out that this scale height depends highly on the temperature.

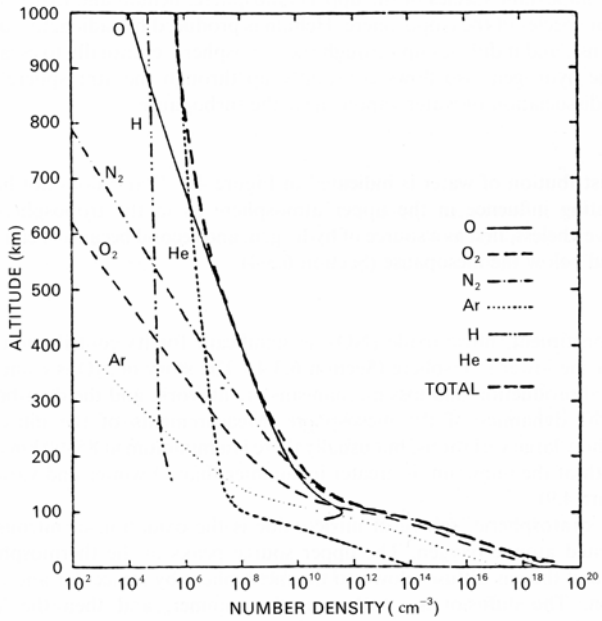

Figure 10. Major components of the atmospheric composition up to 1000 km high for a typical temperature profile. Figure modified from Hargreaves 1992.

Other most important minor species at the lowest part of the atmosphere are NO (which becomes the principal ionizable gas at high latitudes during precipitation events), alkali metals, introduced in the lower ionosphere in meteors and H_2O which is the source of H by dissociation.

2.2.1 D region

The D region is the lowest part of the ionosphere; from 60 to 95 km with a mean electron density of 10^4 cm^{-3} during the day and it vanish at night. This is the most complex part of the ionosphere because there is a mixture of major and minor elements all of them involved in the photochemical reactions and several different sources of ionization contribute significantly to ion production (Hargreaves 1992):

- The $Lyman-\alpha$ line ionizes the NO
- The EUV radiation ionizes O_2 and N_2
- Hard X-rays (0.2-0.8 nm) ionize all constituents; mostly O_2 and N_2
- Galactic cosmic rays become a major ionization source in the lower D region
- Energetic particle from the Sun or of auroral origin ionize the D region at high latitudes

This region is important for radio propagation because it absorbs energy from waves at Middle Frequency (MF), High Frequency (HF) and Very High Frequency (VHF).

2.2.2 E region

The E region is located between 90 to 160 km and it is essentially a $\alpha-Chapman$ layer formed by the 80 to 102.7 nm part of the EUV spectrum which ionizes the O_2 to form O_2^+. The electron density during the day is about 10^5 cm^{-3} and it descends to $5{\cdot}10^3$ cm^{-3} during the night. The fact that is doesn't vanish at night can be due to meteoric ionization (Hargreaves, 1992).

The most remarkable anomaly of the E region is the sporadic E layer (Es). It is observed at constant height (within the E region) and extends to higher frequencies than the regular E layer (Hargreaves, 1992). At high latitudes, Es is produced by energetic electrons from the magnetosphere; at middle latitudes the principal cause is a variation of wind speed with height (wind shear) which, in presence of the geomagnetic field, compresses the ionization (Davis 1990).

Sporadic E is significant in radio propagation since it may reflect signals that would otherwise penetrate to the F region. This effect is known as blanketing.

2.2.3 F1 region

F1 region is located from 160-180 km with an electron density of $5 \cdot 10^5$ cm^{-3} during the day and vanish during the night. The main ion production is attributed to the ionization of O and N_2 by the most heavily absorbed part of the solar spectrum (20-90 nm). As well as the E region, F1 region is an $\alpha - Chapman$ layer. This region never appears in winter at sunspot maximum and is more pronounced in summer at sunspot minimum. When h_t, the transition height between α-type and β-type recombination is larger than $h_m F1$, the height of maximum electron production rate for F1, F1 region appears. During solar minimum ionizing radiations in the X-ray and EUV bands diminish. As a response, the electron density decrease and β diminishes (equation 9). As β decreases with altitude, then h_t will be higher and the probability to observe F1 is larger than during solar maximum when the electron density increases due to the increase of the ionization radiation (Hargreaves 1992).

2.2.4 F2 region

F2 region is observed approximately from 180-2000 km and peaks around 200-400 km with the maximum of the ionospheric electron density (10^6 cm^{-3}) even if the ion production rate reaches the maximum at 140-170 km. This region cannot be a Chapman layer since the atmosphere above the F1 region is optically thin to most ionizing radiation. The fact that the electron density reach the maximum in the F2 region and not in the F1 region is due to the height variation of the recombination processes which forms the F2 region as an upward extension of F1 due to the plasma diffusion even though the production rate is now decreasing with height.

In the F2 region the dominant ionization source is the photoionization of O and the two stage recombination process is:

$O^+ + N_2 \rightarrow NO^+ + N$ with rate $\propto \beta[O^+]$

$NO^+ + e \rightarrow N + O$ with rate $\propto \alpha[NO^+]N_e$

As explained in section 2.1.2, β depends on the concentration of the neutral molecules; then, at low altitude β is large and the first reaction goes quickly and all O^+ is rapidly converted to NO^+; then, the overall rate is governed by the rate of the second reaction giving and α-type process because $[NO^+] = Ne$ for neutrality. At high altitude β is small and the first reaction controls the overall rate. Then $[O^+] = N_e$ and the process appears to be β-type being the transition height, h_t, between 160 and 200 km. As explained before, if $h_m F1 < h_t$ the region below h_t is the F1 and above it is F2; if $h_m F1 > h_t$ F1 does not appear and the whole region is called F region.

Where the recombination is β-type,

$$N_e = q/\beta \propto [O]/[N_2] \tag{13}$$

because the ion production rate depends on the O concentration and the recombination process depends on the N_2 concentration. This fact makes the electron density increase with height until the air density decreases and diffusion becomes more important. Then F2 layer peaks where these two processes are equally important (Hargreaves 1992).

Another important characteristic of the F2 region is that it does not vanish at night. Around 700 km, the ionosphere dominated by O^+ gives way to the protonosphere dominated by H^+. The ionization potential is almost the same for these two ions and therefore, the reaction $H + O^+ \leftrightarrow H^+ + O$ enables ionization

to move readily between ionosphere and protonosphere. During the night, when the radiation source vanishes, the concentration of O+ does not disappear completely due to this connection with the protonosphere. Since F2 region has the greatest concentration of electron and does not vanish at night, it is the region of greatest interest in radio propagation.

In table 2 there is a summary of the altitude and electron density for each layer.

Table 2. Different regions in the ionosphere with their average altitudes and electron density.

Region	**Altitude (km)**	**Electron density (cm-3)**
D	60-90	10^4
E	90-160	$5 \cdot 10^3$-10^5
F1	160-180	$5 \cdot 10^5$
F2	180-2000	10^5-10^6

The typical vertical structure of the ionosphere is shown in figure 11 (left). It is possible to see the diurnal and solar cycle difference due to the variation of incoming radiation. D and F1 regions vanish at night due to the disappearance of the ionization source, and the E and F2 region become much weaker. During low solar activity the ionizing radiation (X-rays and EUV) reduces and the electron density decreases. In figure 11 (right) it is shown the typical ion composition of the dayside ionosphere under solar minimum conditions. As explained before it can be seen that at low altitudes the major ions are O_2^+ and NO^+, near the F2 peak it changes to O^+ and in the topside ionosphere H^+ becomes dominant.

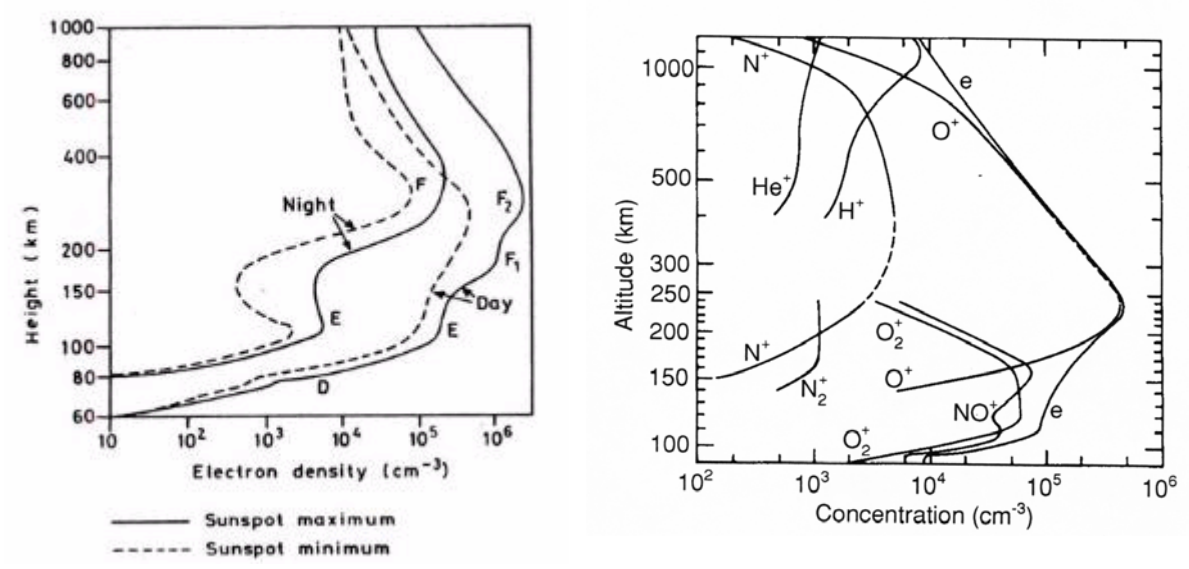

Figure 11. Left: Typical vertical profile of electron density in the midlatidue ionosphere from Hargreaves (1992). Right: Typical composition of the dayside ionosphere at solar minimum from Gombosi (1998)

2.3 Ionospheric currents

The presence of mobile charges (free electrons and ions) in the ionosphere makes the ionosphere highly conducting. Figure 12 shows typical density profiles of both, atmospheric neutral molecules and charged particles at mid latitudes. As neutral density exceeds the plasma density by several orders of magnitude, neutral constituents and their dynamics have an impact on the plasma dynamics (Richmond and Thayer, 2000). Through collisions with the neutral air, some of the motion is transferred to the ionized species driving them along in the same direction as a plasma drift.

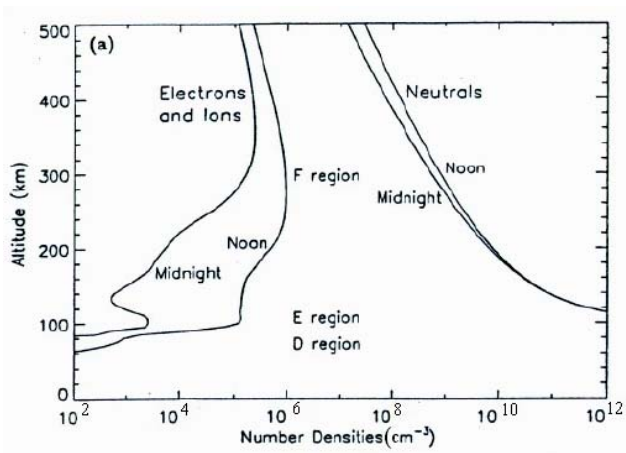

Figure 12. Density profiles of electrons, ions and neutrals. Figure modified from Richmond and Thayer, 2000.

There are, however, two complicating factors, collisions between the charged and neutral particles (collision frequency, υ – the number of times a particle of one kind collides with other particle of other kind) and the presence of the geomagnetic field (gyrofrequency, $\omega = eB/m$ – the frequency at which a charged particles gyrates in the field) (Hargreaves, 1992). Where $\upsilon >> \omega$, collisions prevent the particle from gyrating and the plasma is carried along with the wind and where $\upsilon << \omega$, a perpendicular movement appears. This fact occurs at about 75 km for electrons and 120 km for ions (see figure 13) due to the different mass between the ion and the electron. Between these levels the ions move more or less with the neutral wind and the electrons move across it. The relative movement between ions and electrons and the sufficient plasma density at these heights constitutes an electric current. The separation of charges produces an electric field which in turn also affects the electric current (dynamo effect). Above about 130 km the ions also start to gyrate and to move perpendicular to the wind. Even if the plasma density increases, the drift of ions and electrons in the same direction does not constitute an electric current (Maus, 2006). The region where the wind is more effective in producing an electric current coincides with the E region.

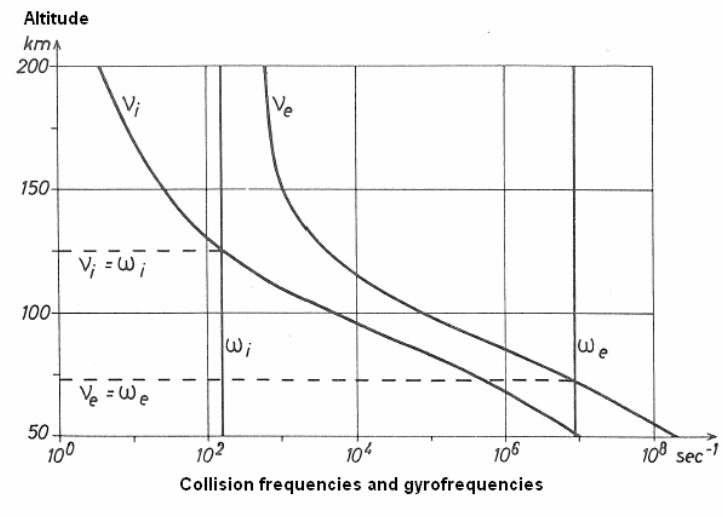

Figure 13. Day side vertical profile of collision frequencies and gyrofrequencies for ions and electrons. The dashed lines define the dynamo region Figure modified from Maus, 2006.

In the presence of electric and magnetic field, the total current vector is given by:

$$\vec{j} = \sigma_P \vec{E}_\perp - \sigma_H (\vec{E} \times \vec{b}) + \sigma_0 \vec{E}_\parallel \tag{14}$$

where σ_P and σ_H are the Pedersen and Hall conductivities respectively, σ_0 is the conductivity along the magnetic field lines, $\vec{b}$ is the unit vector along the magnetic field line and $\parallel$ and $\perp$ refer to vector component with respect to the magnetic field. From equation 15 it is possible to see that ionospheric conductivity depends on the plasma density, gyrofrequency and collision frequency.

$$\sigma_o = N_e e^2 \left(\frac{1}{m_e \nu_e} + \frac{1}{m_i \nu_i} \right) \tag{15a}$$

$$\sigma_P = \frac{N_e e}{B} \left(\frac{\nu_i \omega_i}{\nu_i^2 + \omega_i^2} + \frac{\nu_e \omega_e}{\nu_e^2 + \omega_e^2} \right) \tag{15b}$$

$$\sigma_H = \frac{N_e e}{B} \left(\frac{\omega^2{}_e}{\nu_e^2 + \omega_e^2} - \frac{\omega^2{}_i}{\nu_i^2 + \omega_i^2} \right) \tag{15c}$$

Pedersen and Hall conductivities peak in the E region (where $\upsilon << \omega$) whereas the direct conductivity is of much greater magnitude and it continues to increase with altitude due to the decreasing collisions with the neutral gas and the larger electron density at higher altitudes (Hargreaves, 1992).

At high latitudes, the large magnitude of the direct conductivity allows that electric fields generated in the ionosphere close along the magnetic field lines into the magnetosphere and vice versa. These currents are called field-aligned currents (see figure 14). At mid latitudes much of the ionospheric current is generated by the ionospheric wind dynamo which on the average produces global current vortices on the dayside of the Earth, counterclockwise in the northern hemisphere and clockwise in the southern hemisphere. These currents are called the Sq currents (see figure 14) and produce the quiet time diurnal

variation of the geomagnetic field. At low latitudes, near the magnetic equator, there is an intensification of the eastward current that is called equatorial electrojet (see figure 14).

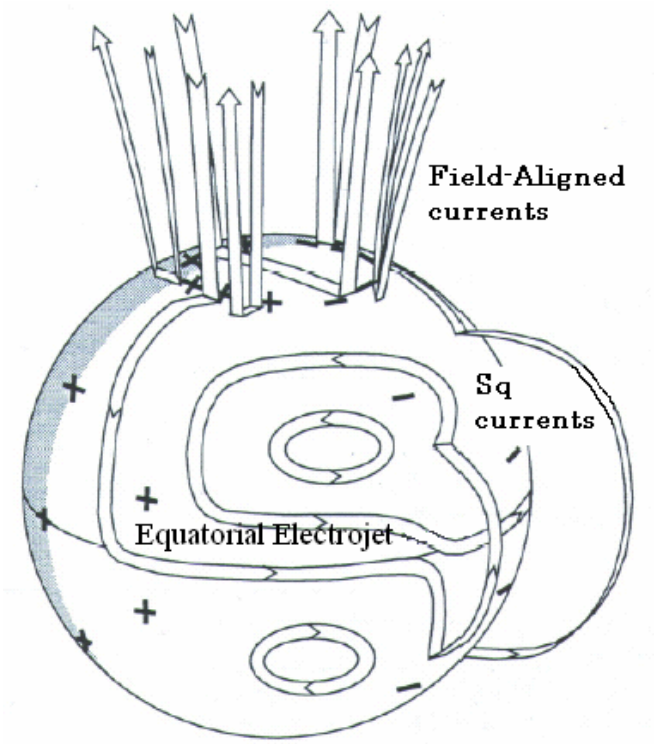

Figure 14. Ionospheric electric currents viewed from the dayside of the Earth. Image modified from Richmond and Thayer, 2000.

During magnetic storms the global ionospheric electric currents and their associated magnetic variations increase in magnitude. At high latitudes, this increase is intensified due to the energy transferred from the solar wind to the ionosphere trough the field-aligned currents. Hall currents in the polar oval intensify and generate the auroral electrojets as a circular belt. As shown in figure 15, these current jets flow westward in the morning sector and eastward in the evening sector (Prölss, 2004).

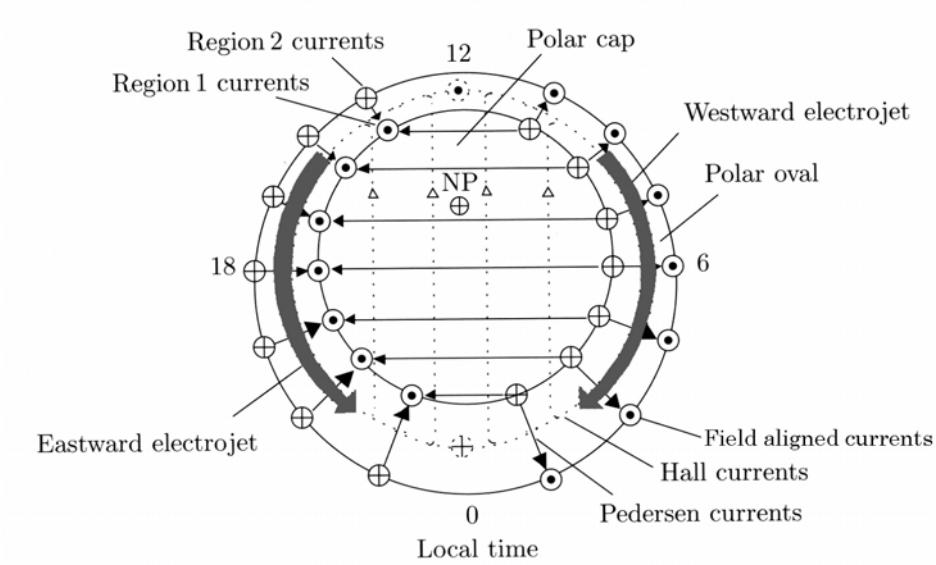

Figure 15. Horizontal distribution of electric currents in the polar ionosphere. Figure modified from Prölss, 2004.

Usually, the effects on the total magnetic field of the auroral electrojets are observed at high latitudes. During large geomagnetic storms, the distribution of the field aligned currents move equatorward and the effects can be observed to mid latitudes (Iijima and Potemra, 1976). The effects of the auroral electrojet are more intense than the effects of the ring current observed at low latitudes because the aural electrojets occur in the E layer and it is closer to the Earth. Auroral electrojets produce both, positive and negative disturbances. Deviations in the local afternoon sector tend to be positive and those in the night and morning sectors are mostly negative due to the eastward and westward auroral electrojet respectively (Prölss, 2004). AU is the magnetic index that describes the intensity of the eastward electrojet and AL characterizes the combined effect of the morning and midnight westward electrojet. AE is the auroral electrojet formed by subtracting the two indices: $AE = AU - AL$.

2.4 Observation methods

2.4.1 Ground-based Ionosonde

The ground-based ionosonde is the most conventional equipment for measuring the vertical electron density profile. An ionosonde emits radio waves at different frequencies, usually from 1 to 30 MHz, and measures the time used by the pulse to go up and down once reflected in the ionosphere. Altitude at which the pulse was reflected can be thus deduced.

The refractive index (n) for an ionized medium with no magnetic field is:

$$n^2 = 1 - \frac{f_N^2}{f^2} \tag{16}$$

where f is the frequency of the emitted wave and f_N is the plasma frequency which depends on the electron density as:

$$N = \left({f_N}^2 (MHz) \big/ 80.6 \right) \cdot 10^6 \, cm^{-3} \tag{17}$$

As the electron density increases with altitude, f_N increases and the refractive index becomes smaller. Where $f_N > f$, the refractive index is imaginary and the radiowave cannot propagate. Therefore, the radiowave is reflected at the level where $f_N = f$; where the plasma frequency equals the wave frequency. As the wave frequency increases, the pulse can penetrate to higher altitudes in the ionosphere until the frequency of the wave equals the critical plasma frequency fo. This frequency is related to the maximum electron density of each layer by the eq. 17. Measuring the time that the echo is received by the ionosonde and assuming that the wave travels at the speed of the light, it is calculated the altitude where the pulse was reflected. This altitude is called “virtual altitude” since the wave is not exactly traveling at the speed of the light

c, but at the velocity group $u = c/n$ (Hargreaves, 1992). This velocity group is calculated afterwards to obtain the real-height vertical electron density profile N(h). In Appendix A there is a list of the main ionospheric parameters obtained with an ionosonde.

A virtual height versus frequency record is called ionogram. Examples of night and day time ionograms for a mid latitude station on a spring day are detailed in figure 16. The X-axis corresponds to the frequency and the Y-axis to the virtual height. Due to the presence of the geomagnetic field, there are two different values of the refractive index, implying that waves can propagate at two speeds. These are called the ordinary and the extraordinary wave and have different reflection conditions (Hargreaves, 1992). Because the ordinary wave has the same conditions that a wave propagating without magnetic field, the echoes obtained from it are of interest. In figure 16, the red traces are the echoes of the ordinary wave, and the green are the traces for the extraordinary wave.

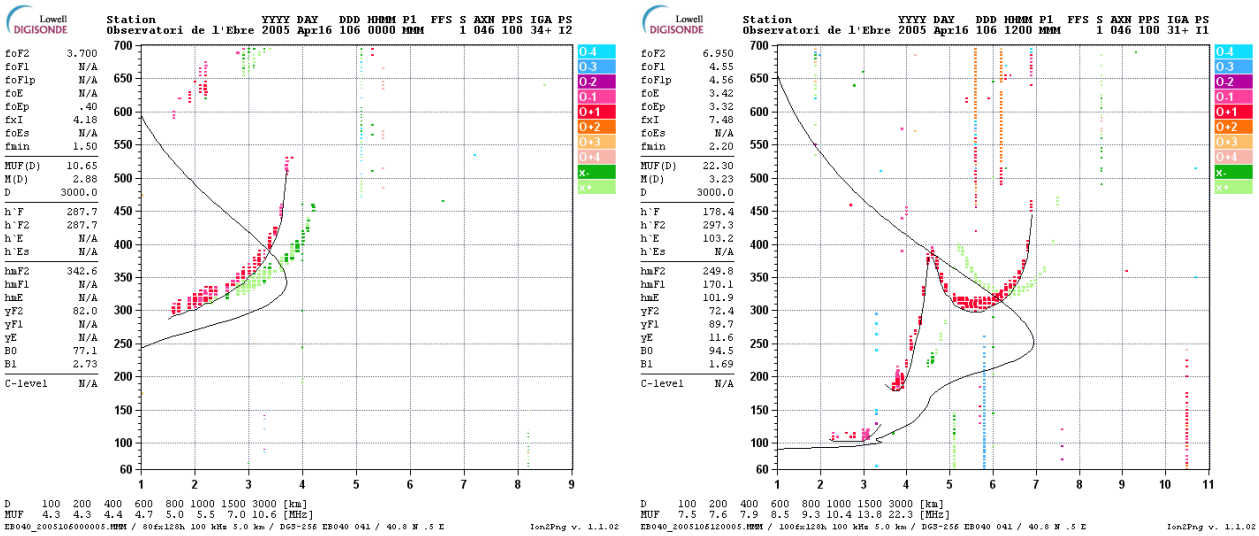

Figure 16 Left: Night time ionogram (0:00 UT). Right: Day time ionogram (12:00 UT). Ionograms obtained from the Ebre Observatory UMLCAR Digisonde (www.obsebre.es)

From figure 16 it is possible to see that at night only F region echoes are present. As explained in previous section, the F1 layer disappears during the night because the ionization is controlled by the solar radiation. The E region doesn't disappear completely but the electron density decreases so much during the night that the ionosonde can't detect it (same for D region).

There are different kinds of ionosondes and each one calculates the vertical electron density profile, N(h), (black line in the ionograms in fig. 16) using different models. The most common ionosonde used nowadays is the digisonde developed by the University of Massachusetts Lowell's Center for Atmospheric Research (UMLCAR) which allows real time ionospheric data. There is a global network of UMLCAR digisondes that provide good information for Space Weather purposes.

Nevertheless, the ground-based ionosonde technique has several limitations:

- High resolution data only up to the ionospheric F region maximum electron density height (hmF2).
- Low resolution at low altitudes (D and night E region)

2.4.2 Incoherent Scatter Radars

The incoherent scatter technique makes possible the study of the topside of the ionosphere (which is impossible from ground-based ionosondes) and the measurement of a variety of other properties of the upper atmosphere such as ion composition, electric field strength, conductivity and currents. An example of the vertical electron density profile obtained from incoherent scatter radar is shown at left in figure 17.

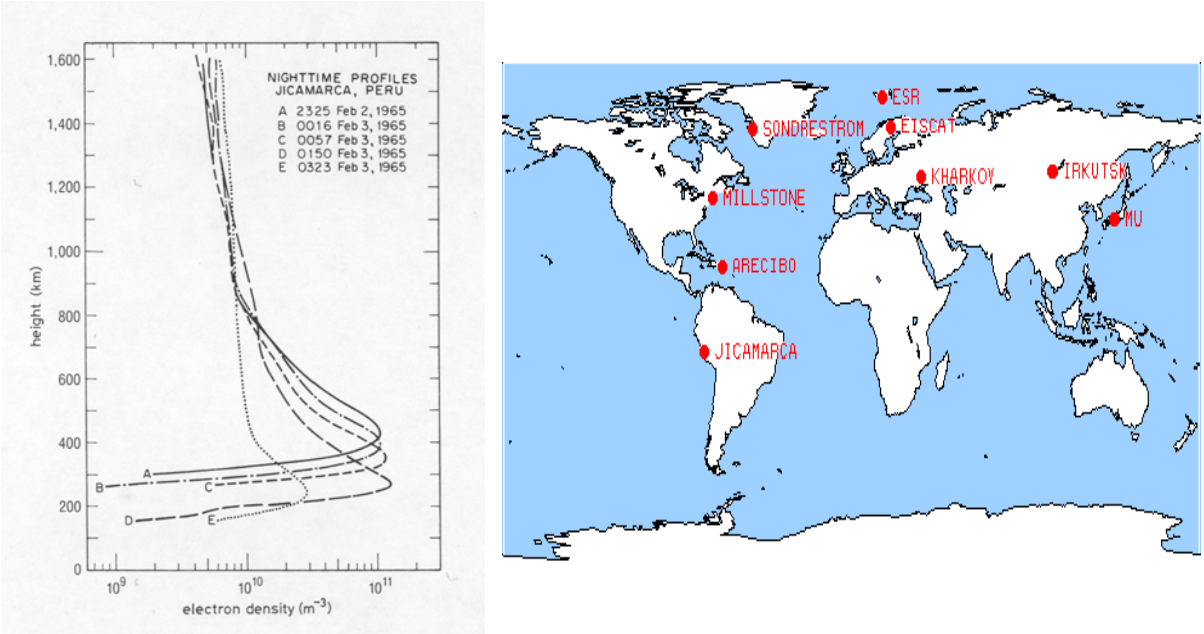

Figure 17. Left: Electron density profiles at Jicamarca, Peru, obtained with the incoherent scatter technique. Figure obtained from Davies (1990). Right: World's operational incoherent scatter radars. Image obtained from MIT Haystack Observatory web (http://www.haystack.mit.edu/).

The incoherent scatter technique is based on the classical Thomson scattering of waves from individual electrons. The echo is the result of the scattering of electromagnetic energy, radiated from the radar, by electrons in the ionosphere, which are controlled by the much slower and massive positive ions. Most of the power is due to scattering from electron density fluctuations caused by the presence of these ions and the frequency spectrum of the received signal provides information about their temperature, composition and velocity. The total returned power depends on the number of electrons and gives an estimation of the ionospheric electron density (Davis, 1990).

The main limitation of the incoherent scatter radar is that it is very expensive to build and operate that there exist relative few and studies from their data can only be local. In figure 17, at right, it is shown the distribution of the current incoherent scatter radar network.

2.4.3 Ground-based GPS receivers

Global Positioning System (GPS) is a very useful tool to estimate the spatial position of a receiver on the Earth. However, as a secondary product, it is able to provide the vertical ionospheric electron content; and with a wide network of receivers, the Total Electron Content (TEC) at global scale. The TEC is the integral with height of the ionospheric electron density profile (Appendix A) and it is a parameter widely used in studies of the near-Earth plasma environment.

The space segment of the GPS consists on a constellation of 24 satellites distributed in 6 orbital planes at about 20000 km of altitude. The satellites are distributed within their planes so that from almost any place of the world at least four are above the horizon at any time. Nowadays there is a global network of about several thousands permanent ground GPS receivers. About 300 are managed by the International GPS Service (IGS) (see figure 18).

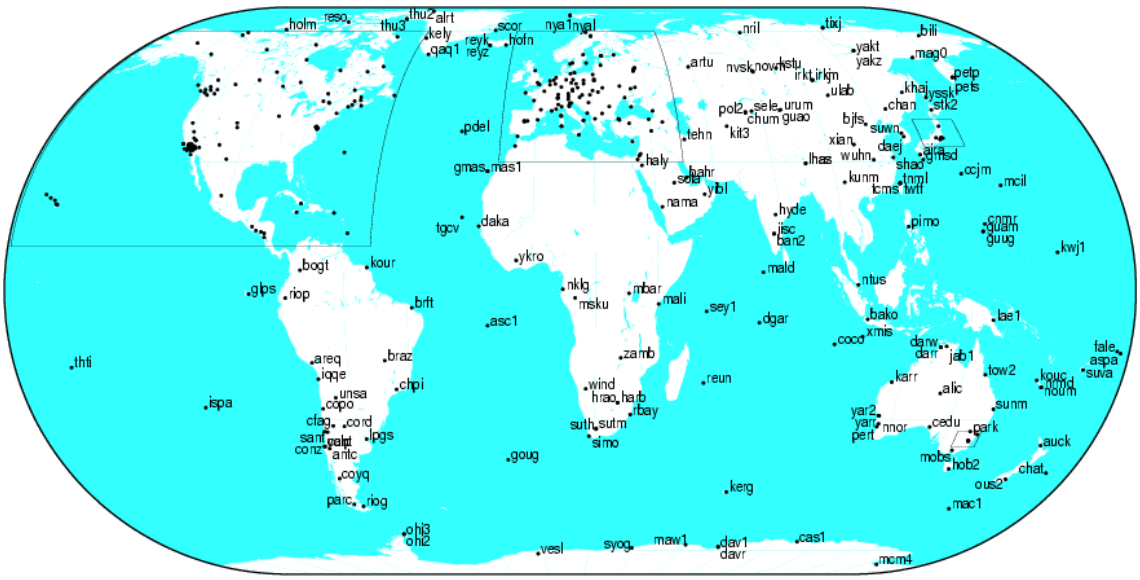

Figure 18. IGS network of permanent GPS receivers. Image obtained from the International GNSS Service web (http://igscb.jpl.nasa.gov).

Each satellite transmits two carrier frequencies at L-band, L1 at 19.0 cm and L2 at 24.4 cm which are biased due to the propagation through the atmosphere as well as the existence of some receiver and satellite clocks errors and carrier phase ambiguities.

$$\begin{aligned} L1_R^S &= \rho_R^S + c(dt_R - dt^S) + rel_R^S + T_R^S - \alpha_1 I_R^S + \lambda_1 B1_R^S + \omega_{L1} + m_{L1,R}^S + \varepsilon_{L1,R}^S \\ L2_R^S &= \rho_R^S + c(dt_R - dt^S) + rel_R^S + T_R^S - \alpha_2 I_R^S + \lambda_2 B2_R^S + \omega_{L2} + m_{L2,R}^S + \varepsilon_{L2,R}^S \end{aligned} \quad (18)$$

where ρ is the geometric distance, dt is the clock offset, rel is the relativistic effect, T is the delay produced by the troposphere, α is the effect of the ionosphere depending on the frequency ($\alpha_i = 40.3/f_i$), I is the Total Electron Content along the propagation path, B is the phase ambiguity, ω is due to the polarization of the signal (wind-up), m is the multipath and ε is noise. Superindex S and subindex R mean satellite and receiver respectively.

With a dual-frequency receiver it is possible to cancel the part which is independent of the frequency (geometric distance, clock offsets, relativistic effects and tropospheric effects) by computing the so-called ionospheric combination which is the difference between these two frequencies.

$$LI = L1 - L2 = (\alpha_2 - \alpha_1)I + \tau_R + \tau^S \quad (19)$$

where τ_R and τ^S are constants associated to the frequency dependent delays of the receiver and the satellite. From eq. 19 it is possible to estimate the Total Electron Content (I) (Juan et al., 1997). Using this technique, global and regional networks of GPS receivers are capable of providing TEC over large geographic areas (with the exception of large ocean areas where ground-based GPS receivers cannot easily be deployed) in near-real time.

On May 1998 IGS created the Ionosphere Working Group and five different centers started computing and making available several GPS-derived ionospheric products (mainly Vertical Total Electron Content (VTEC) maps). The five different centers that currently deliver VTEC maps to IGS are Jet Propulsion Laboratory, European Space Agency, Center for Orbit Determination in Europe, Universitat Politècnica de Catalunya and Energy Mines and Resources of

Canada. They use different algorithms to generate grids of VTEC with time resolution of at least 2 hours (Brunini et al., 2004).

CHAPTER 3: IONOSPHERIC STORMS

The regular behavior of the ionosphere (section 2.2) becomes disturbed during geomagnetic storms. As already introduced in section 1.4, geomagnetic storms affect the magnetosphere-thermosphere-ionosphere system. Ionospheric disturbances due to the effects of a geomagnetic storm are called ionospheric storms and the same for the magnetosphere (magnetospheric storms) and thermosphere (thermospheric storms). Depending on the onset of the storm, latitude and season, the ionosphere reacts by increasing the electron density (positive ionospheric storm) or decreasing (negative ionospheric storm). These changes in the electron density produce significant modification in the ionospheric radio transmission. In figure 19 there is shown the ionospheric density profile for both cases.

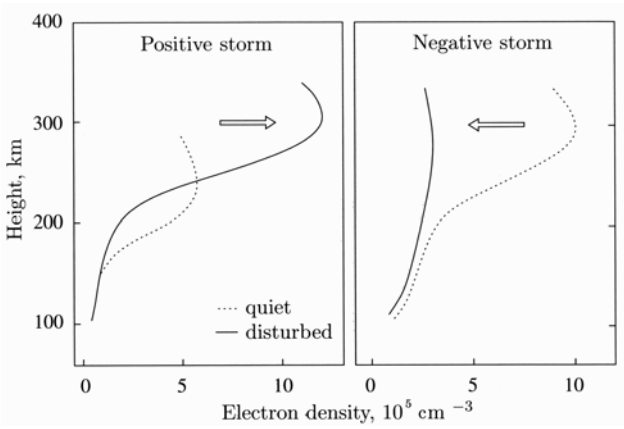

Figure 19. Electron density profiles as observed during a positive (left) and negative (right) ionospheric storm. The dotted profiles represent quiet-time references. Figure modified from Prölss, 2004.

All three terms in eq. 1, independently or a combination of them can cause the observed density changes, an increase/decrease of the production rate or a

decrease/increase of the loss rate (by both, recombination or movement mechanisms) can cause positive/negative effects respectively (Prölss, 2004).

3.1 Negative ionospheric storms

The decrease of electron density is due mainly to changes in the neutral gas composition (Prölss, 1993). During a geomagnetic storm there is a heating of the auroral region due to the energy deposited by precipitating particles and Joule dissipation of electric currents (figure 20, left) (Danilov and Lastovicka, 2001). This heat produces changes in the neutral gas composition by increasing the concentration of N_2 and decreasing the concentration of O (figure 20, right). Such a region is called “composition bulge”.

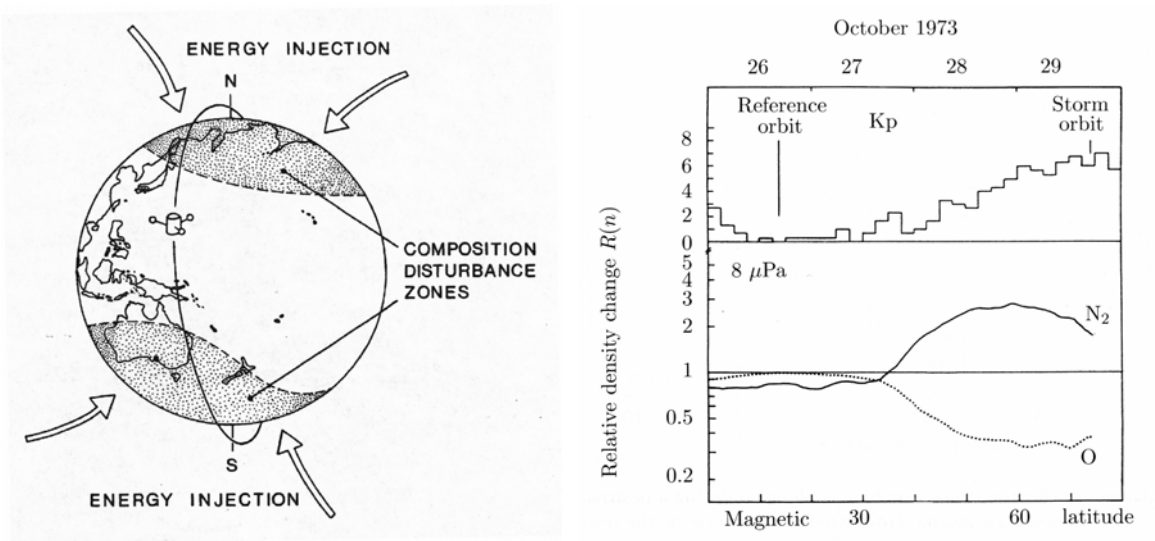

Figure 20. Left: Neutral composition disturbance zones during a geomagnetic storm. Image obtained from Prölss, 1995. Right: Relative density changes observed during a geomagnetic storm at a constant pressure level of 8μPa which corresponds approximately to an altitude of 300 km. The upper panel shows the magnetic activity during the storm by the kp index. Image modified from Prölss, 2004.

As explained in section 2.2, the ion production rate depends on the O concentration ([O]), and the recombination process on the N_2 concentration ([N_2]). If there is a decrease of [O], the ion production rate decreases and if there is an increase of [N_2] the recombination process increases leading with a decrease in the electron density. This fact together with an increase of the recombination rate due to the higher temperature produces the negative

ionospheric storm (Danilov and Lastovicka, 2001). The composition bulge can be moved to middle latitudes either by the background quiet-day thermospheric circulation (equatorward) or by the storm circulation driven by the high latitude heat input and brought into the dayside by Earth's rotation (Fuller-Rowell, 1994). Moreover, the transport of the composition bulge also has a seasonal dependence. In winter, the daytime thermospheric circulation is poleward and it confines the negative phase to high latitudes. In summer or during the winter nighttime period, the background thermospheric circulation is also equatorward and the zone of disturbed composition can move to lower latitudes. This leads to a rather frequent occurrence of the negative phase at middle latitudes at night in winter and during summer (night and daytime) (Fuller-Rowell, 1996).

Accordingly, all ionosonde stations located underneath the zone of disturbed composition should observe negative ionospheric storm effects.

3.2 Positive ionospheric storms

The origin of positive ionospheric storms is less clear and more mechanisms are involved depending on the latitude. At auroral and sub-auroral latitudes there is a large increase of electron density due to the direct energetic particle precipitation (Prölss, 1995) while at mid and low latitudes, the mechanisms responsible of the positive ionospheric storm can be the Traveling Atmospheric Disturbances (TAD), changes in the large-scale thermospheric wind circulations, electric field perturbations and changes in the neutral gas composition. All these mechanisms uplift the F layer to higher altitudes (along geomagnetic fields) where the loss rate by recombination decreases and lead to an increase of the electron density (Prölss, 1995). The energy injected into the upper atmosphere will generate TADs which are pulse-like atmospheric perturbations which propagate from auroral to lower latitudes at high velocity (600 m/s) carrying along meridional winds (150 km/s). In 1-3 hours, TADs arrive at mid latitudes and produce an increase of the vertical drift that uplift the F layer for a short period (2 hours) increasing the electron density. This mechanism is applicable only to the daytime ionosphere because the lack of ionization production at night does not

allow the formation of large positive storm effects (Prölss, 1995) (figure 21).

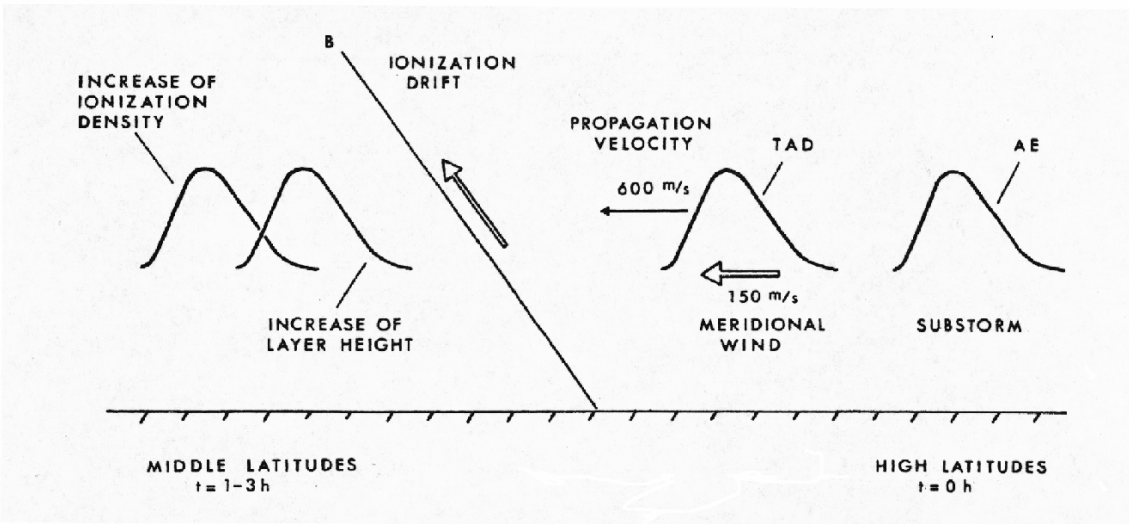

Figure 21. Short-duration positive ionospheric storm cause by a TAD. Image obtained from Prölss, 1995.

Change in the global wind circulation is the responsible of the longer lasting positive storms. As explained before, the background thermospheric circulation is disturbed during the storm and the poleward winds on the dayside can be diminished or even reversed leading to a persistent uplift of the F layer (Prölss, 2004). All these mechanisms need several hours to produce positive ionospheric effects. Long-lasting positive ionospheric storms that occur almost immediately after the onset of the storm (SSC) are due to electric field perturbation. An eastward electric field can uplift the F layer through $\vec{E} \times \vec{B}$ drift increasing the electron density (Huang et al. 2005). The enhancement of the ionospheric electric field can last for many hours and is related to the penetration of the interplanetary electric field (Huang and Foster, 2005).

In figure 22 there is a sequence of both ionospheric storm effects. It is shown how the composition bulge (zone of depleted [O]/[N_2]) expands equatorward in the night side and arrives into the dayside during the recovery phase of the storm due to the Earth's rotation. It is shown also the propagation of the TADs to lower latitudes in 1-3 hours after the onset of the storm. 1 and 2 mean stations that will observe positive and negative effects respectively.

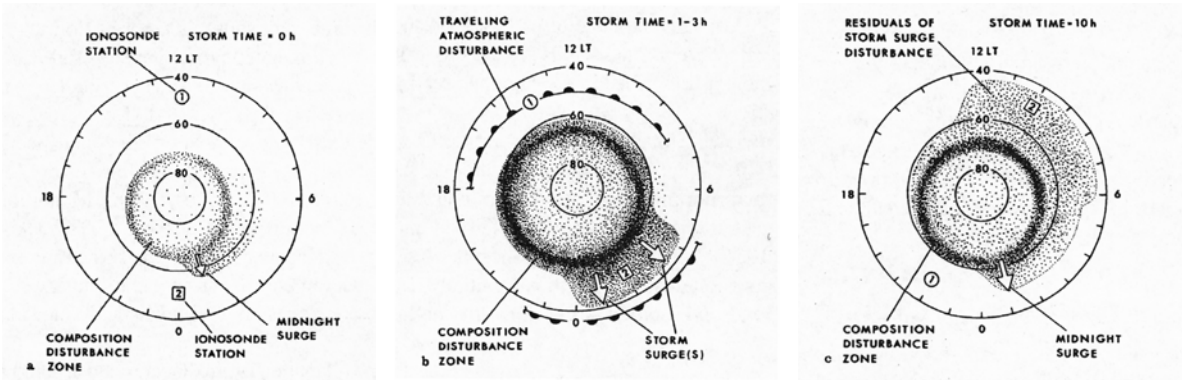

Figure 22. Time sequence of ionospheric storm effects. View from above onto the northern hemisphere for 80, 60 and 40 magnetic latitudes. The dotted area identifies regions with depleted [O]/[N2]. Image modified from Prölss, 1995.

CHAPTER 4: IONOSPHERIC EFFECTS OF THE 20 NOVEMBER 2003 GEOMAGNETIC STORM

The 20 November 2003 was the second largest storm since 1957 in terms of the Dst index values (Ebihara et al., 2005). The IMF dropped to large negative values allowing the penetration of a large amount of energetic particles in the ring current and in the auroral oval. The Helio-Geophysical conditions of this storm are explained in detail in section 4.3.1. As it was a very large geomagnetic storm, large effects on the magnetic field and on the ionosphere were observed.

The effects of the ring current and the auroral electrojets on the ground magnetic field were observed from ground-based magnetometers. The effects on the vertical structure of the ionosphere were observed from ground-based ionosonde. The effects on the total electron content over Europe were observed from ground-based GPS receivers. The external magnetic field was deduced from ground-based magnetic data extracting the contributions of the core, mantle and lithosphere using a geomagnetic model.

The most remarkable effects were the observation of a particle E layer at mid-low latitudes, the uplift and spread of the F region, both, positive and negative ionospheric storms at different latitudes and the displacement of the eastward auroral electrojet at latitudes as low as 55º N.

4.1 Data

4.1.1 Helio-Geophysical conditions data

The Helio-Geophysical background for the November 2003 event was obtained from several data sources. The IMF data were obtained from ACE MAG Level 2 data, and the solar wind velocity and density were obtained from ACE SWEPAM Level 2, both provided by the ACE Science Center (ASC) (http://www.srl.caltech.edu/ACE/ASC/). ACE satellite orbits the L1 libration point, which is the point of Earth-Sun gravitational equilibrium about 1.5 million km from the Earth and 148.5 million km from the Sun. With a semi-major axis of approximately 200000 km the elliptical orbit affords ACE a prime view of the Sun. Proton fluxes and the magnetic field component parallel to the Earth's rotation axis (Hp) at geostationary orbit distance from the Earth were obtained from GOES-10 satellite data (longitude of 135º W) at the Space Environment Center (http://sec.noaa.gov/Data/). The geomagnetic activity indices Ap and Dst were obtained from the International Service of Geomagnetic Indices (ISGI) of the International Association of Geomagnetism and Aeronomy (IAGA) at http://isgi.cetp.ipsl.fr/.

4.1.2 Ground-based ionosonde

The effects on the vertical structure of the ionosphere and on the electron density in the E layer during the geomagnetic storm were observed from ground-based UMLCAR digisondes (except that of Sodankyla). Figure 23 shows the spatial distribution of these stations and their coordinates can be found in Appendix B.

Data from Pruhonice, El Arenosillo and Sodankyla were supplied directly from these observatories and Chilton data were obtained via ftp from the World Data Center C1 (WDCC1) at Rutherford Appleton Laboratory (RAL), ftp://wdcc1.bnsc.rl.ac.uk/. The rest of the data were retrieved from the Digital Ionospheric Data Base (DIDBase) at the University of Massachusetts Lowell's Center for Atmospheric Research (UMLCAR) (http://umlcar.uml.edu/DIDBase/) where data from the global network of the UMLCAR digisondes are collected. Ebre data couldn't be used because during that period the ionosonde was out of order due to lighting damage.

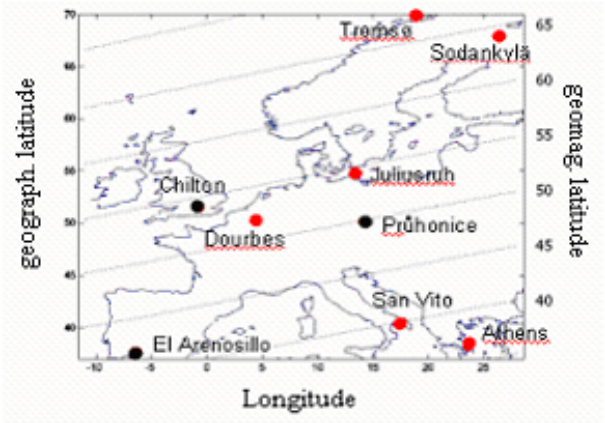

Figure 23. Spatial distribution of the ground-based digisondes to extract the electron density in the E layer. Black dots show the stations used to observe the effects on the vertical structure.

4.1.3 Ground-based GPS receivers

The Total Electron Content of the ionosphere was estimated from ground-based GPS dual-frequency receivers. Data from 928 GPS stations in the Northern Hemisphere (150 belonging to the International GPS Service network) were used to generate global maps with a high time resolution of 10 minutes with an accuracy of a few TECUs (1 TECU=10^{16} electrons/m^2) to show the Vertical Total Electron Content (VTEC) evolution during the geomagnetic storm.

4.1.4 Ground-based magnetometers

To study the effects of the external magnetic field contribution on the ground magnetic field, data from magnetic observatories distributed around Europe were used. Data are fully available from the website of the INTERMAGNET organization (http://www.intermagnet.org/). Data from 26 observatories were collected, which give a good coverage over Europe (see figure 24 for the spatial distribution and Appendix C for coordinates).

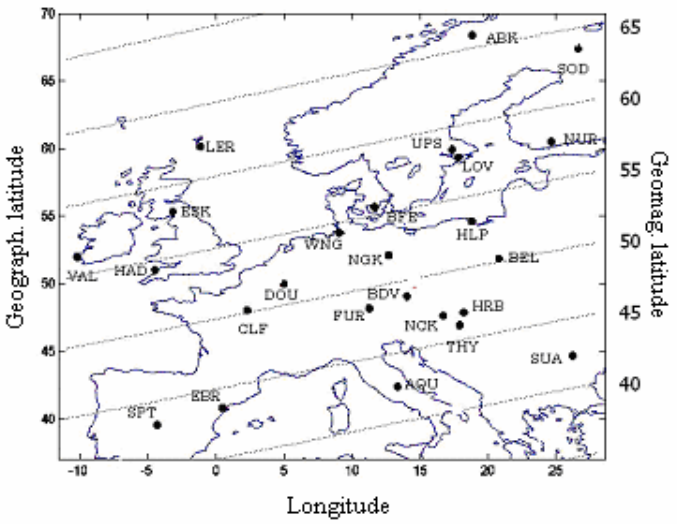

Figure 24. Spatial distribution of the ground-based magnetometers. Dotted lines indicate the geomagnetic latitude.

4.1.5 Geomagnetic model

The geomagnetic model used to estimate the external magnetic field contribution during the disturbed day was the POMME3 model. POMME3 model, the Third generation of the Postdam Magnetic Model of the Earth (Maus et al., 2006), extracted from 5 years of CHAMP satellite data, provides an estimation of the Earth's core, crustal, magnetospheric and induced magnetic fields for quiet days. The major innovations of this model, comparing with previous versions and with the Comprehensive Model 4 (CM4) (Sabaka et al., 2004), is that the internal field is represented to spherical harmonic degree 90 and that the magnetospheric contribution is decomposed in two parts: the contribution of the tail and magnetopause currents and that of the ring current. These two parts are parameterized by the IMF Y component and the new Est (external) and Ist (internal) indices as an improved parameterization of the classical Dst index (Maus and Lühr, 2005).

POMME3 model can be downloaded from http://www.gfz-potsdam.de/pb2/pb23/SatMag/pomme3.html. IMF data were obtained from the Goddard Space Flight Center Space Physics Data Facility (http://omniweb.gsfc.nasa.gov) and Est/Ist data from the National Geophysical Data Center (NGDC) (ftp://ftp.ngdc.noaa.gov/STP/ GEOMAGNETIC_DATA/INDICES/EST_IST/). For

more details about POMME3 model see Maus et al. 2006 since this is not the topic of this study.

4.2. Method

4.2.1 Electron density profile and electron density in the E layer

First step to obtain the electron density profile was to edit the ionograms traces to avoid any mistake of the Automatic Real Time Ionogram Scaler with True Height algorithm (ARTIST) with the Digisonde Ionogram Data Visualization/Editing Tool (SAO-X). Once the ionograms were revised, the true height electron density profiles N(h) were computed with the True Height Profile Inversion Tool (NHPC 4.3) included on SAO-X. The NHPC program calculates the bottomside profiles, from the bottom of the E layer to the peak of the F region, by expressing the profile in terms of shifted Chebyshev polynomials containing the starting plasma frequency and the critical frequency of each layer and describing the E-F transition with a valley model derived from incoherent scatter observation at Arecibo (Huang and Reinisch, 1996). The topside profiles are calculated by approximating the electron density profile above the F2 layer peak to an $\alpha - Chapman$ function with a constant scale height that is derived from the bottomside profile shape near the F2 peak (Reinisch and Huang, 2001). The software is available at the website of the Center for Atmospheric Research of the University of Massachusetts Lowell (UMLCAR) (http://umlcar.uml.edu/).

Once the true height electron density profiles were calculated, the electron density in the E layer was extracted using equation 17.

4.2.2 Total Electron Content

The Total Electron Content (TEC) of the ionosphere was calculated by the UPC/gAGE group of the Universitat Politècnica de Catalunya. They calculate the TEC by solving the ionospheric combination differences

$$\frac{\Delta L_I}{k} = \int_{\vec{r}^T(t^T+\tau)}^{\vec{r}_R(t_R+\tau)} N_e \, ds - \int_{\vec{r}^T(t^T)}^{\vec{r}_R(t_R)} N_e \, ds = \sum\sum\sum (N_e)_{i,j,k} \left[\Delta s_{i,j,k}^{t+\tau} - \Delta s_{i,j,k}^{t} \right] \tag{20}$$

for a two-layer model of the ionosphere assuming that the electron density in each cell is constant (see figure 25). In eq. 20 L_I is the ionospheric combination, i, j, k are the indices for each cell corresponding to local time, geodetic latitude and height; $(N_e)_{i,j,k}$ is the corresponding free electron density and $\Delta s^t_{i,j,k}$ is the length of the ray path crossing the corresponding cells at time t.

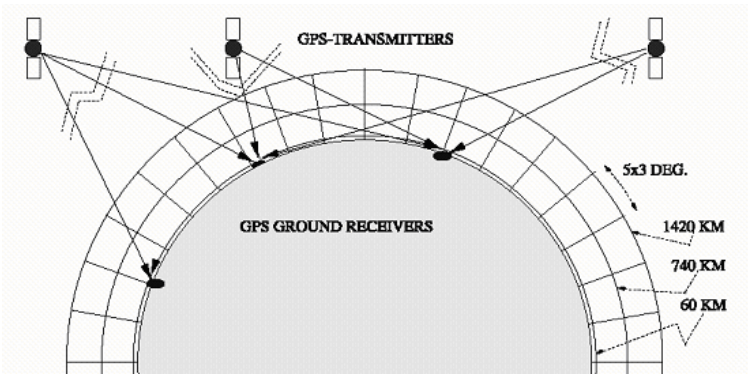

Figure 25. Layout of the two-layer tomographic model of the ionosphere. Figure modified from Hernández-Pajares et al. 2002.

The precision and computation load depend on the size of the cells. Large cells allow less computation time but give a very low resolution that can represent more than 50% of the TEC. Very small cells produce a very good resolution but too much unknowns to be solved. The size of the cells used for this computation was of 5x3 degrees in local time and latitude respectively which give 1 TECU resolution and 6000 unknowns. As it is showed in figure 25, the boundary heights of this tomography are 60-740-1420 km. The two-layer tomography allows a certain vertical structure improving the estimation of the TEC comparing with one-layer model. For more details of the algorithm see Juan et al. 1997 and Hernández-Pajares et al. 1999.

To generate the TEC maps over the Northern Hemisphere, the ionospheric tomographic voxel model was solved by running a Kalman filter fed with data from about 150 worldwide distributed GPS receivers belonging to the International GPS Service (IGS) network for every 10 min (see more details in Hernández-Pajares et al., 2002). Afterwards, to reach the maximum available resolution, the overall available GPS receiver measurements in the Northern Hemisphere (more than 900) were used.

4.2.3 External magnetic field contribution

The external magnetic field on the 20 November 2003 was estimated by subtracting from the observations the core and crustal contributions obtained from POMME3 model. Ring, tail and magnetopause contributions were extracted using POMME3 model with the corresponding IMF-By and Ist/Est indices to observe small-scale effects of the external fields. Sq and local crustal contributions were extracted calculating the difference between the average value over the five quietest days of the month (as recommended by Mandea and Langlais, 2002) from the observations and that obtained with POMME3 model.

It is important to mention that POMME3 model has been used as an attempt to model the storm-time magnetospheric field contributions knowing that it is designed to describe the internal and external magnetic fields on quiet days. When extracting the magnetospheric contribution it is assumed that there are no changes in the geometry of the quiet-time ring current and tail current during the storm or that they do not impact the ground magnetic field and are modulated only by the Dst and Ist/Est indices. This unmodelled part of the magnetospheric contribution of the POMME3 model during storm time period will be observed as a large-scale residue (discussed in section 4.4.3).

4.3. Observations

4.3.1. Helio-Geophysical conditions of 20 November 2003 geomagnetic storm

The Helio-Geophysical conditions during the 19–21 November 2003 event are represented in figure 26.

At 7:30 UT the solar wind parameters recorded at ACE satellite became dramatically disturbed. The solar wind velocity increased suddenly to very high values (3 times superior to normal values) at the same time that the solar wind density increased (plots (b) and (c) of figure 26 respectively). The Z component of the Interplanetary Magnetic Field (IMF Bz) also became disturbed at 7:30 UT and dropped rapidly to strong negative values. IMF Bz remained negative from 11:00 to 23:00 UT reaching its minimum of -50 nT at 15:00 UT (plot (a) from

figure 26). Plot (d) shows the GOES observation of the Hp component (approximately parallel to the Earth's rotation axis) of the magnetic field at geostationary altitude. The reversal of the Hp component to negative values indicates that the magnetopause, typically located at 10 R_E moved inside the geostationary orbit (6.6 R_E). This event is called magnetopause crossing and is caused by extreme conditions of solar wind pressure, often coupled with a strong southward interplanetary magnetic field components (Allen et al., 1989).

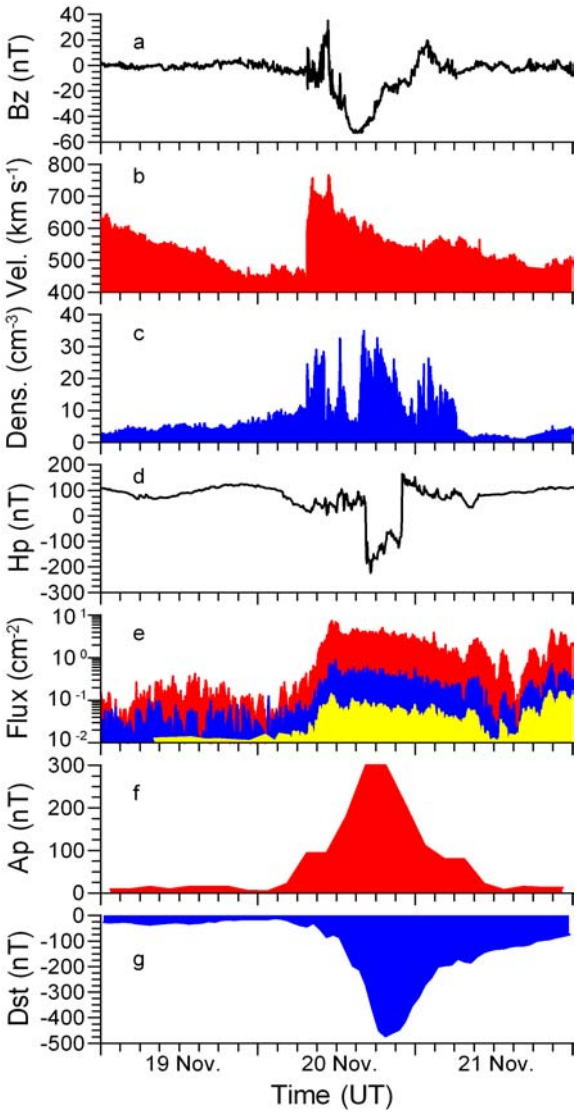

Figure 26. Helio-Geophysical conditions for the 20 November 2003 geomagnetic storm.
Plot (a) shows the IMF Bz component (GSM coordinate system), plot (b) shows solar wind velocity, and plot (c) shows the solar wind density. Plot (d) shows the magnetic field component parallel to the Earth's rotation axis, and plot (e) shows the proton flux (on red for proton with energy 4–9MeV, on blue for 9–15MeV, and on yellow for 15– 40MeV). Plots (f) and (g) show the 3-h Ap and hourly Dst geomagnetic activity indices, respectively. Figure obtained from Blanch et al. 2005.

These values of the solar wind parameters were favourable to produce a very strong geomagnetic storm which started on 20 November 2003 at 8:03 UT. The Ap index (plot (f) in figure 26) reached 300 nT between the 3-h intervals from 16:30-19:30 on 20 November and the Dst index (plot (g) in figure 26) dropped to superstorm values of -472 nT at 19:00 UT. In plate 6, the X components of the

magnetic field recorded at all stations used in the study are shown. From there it is possible to observe the different phases of the geomagnetic storm at different latitudes described in section 1.4. In figure 27, magnetograms from different latitudes for a longitudinal sector are shown. At high latitudes stations, effects of the auroral electrojets are visible (red circle) and they are more intense than the effects of the ring current (blue circle) which are more clearly observed at lower latitudes (from 50º N).

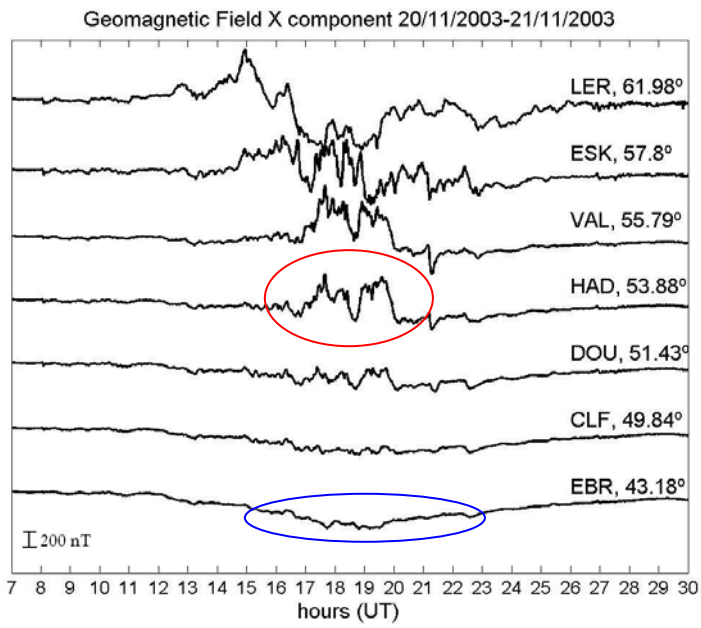

Figure 27. Ground magnetic field for different observatories located from -10º to 5 º longitudes from 7:00 UT of 20th November 2003 to 6:00 of 21st November 2003 sorted from higher to lower geomagnetic latitude.

4.3.2 Effects on the vertical structure of the ionosphere

The effects on the vertical structure of the ionosphere of the strong geomagnetic storm occurred on 20 November 2003 were studied at the three ionospheric stations shown with black points in figure 23. Figure 28 presents some ionograms recorded at Chilton and El Arenosillo showing distinct features of ionospheric effects caused by the event.

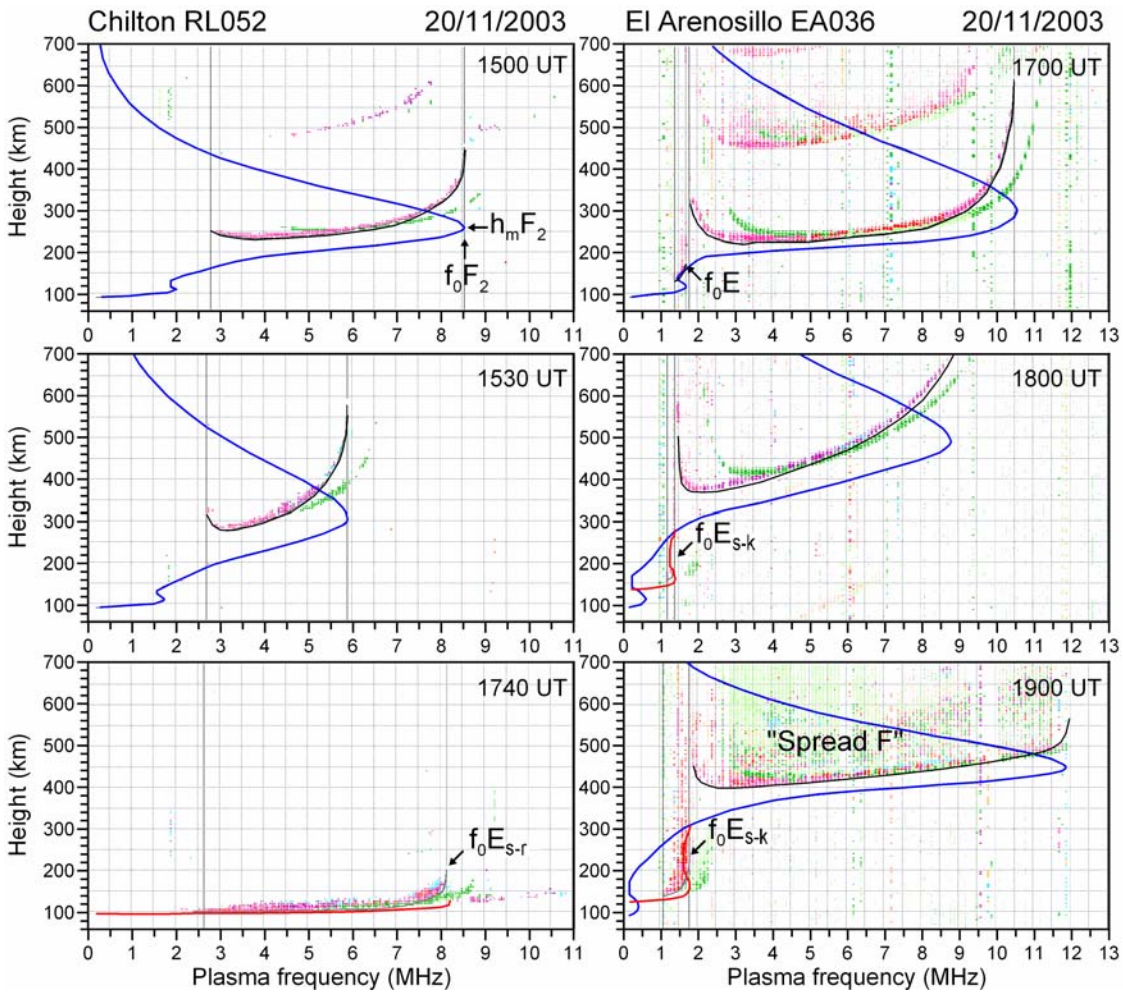

Figure 28. Ionograms obtained from Chilton (left) and El Arenosillo (right) during the evolution of the geomagnetic storm. Figure adapted from Blanch et al. 2005.

Above Chilton, the critical frequency of the F2 layer, foF2, started to become smaller and the F2 layer electron density peak altitude, hmF2, increased rapidly after 15:00 UT. A sporadic E layer was observed at the height of 110 km with a corresponding density much larger than under quiet conditions. This Es layer was exhibited for several hours, from 16:40 UT to 22:30 UT, approximately, and it hid the F-region evolution (blanketing effect). Quite similar ionospheric responses to storm-induced disturbances, as the ones observed above Chilton station, were observed above the Pruhonice observatory. At 16:55 UT a thick Es layer appeared and it lasted for several hours (Fig. 29). Comparing with that of Chilton, the Es layer over Pruhonice was observed at higher altitudes (from 120 to 150 km) and also hid the F region behaviour most of the time until midnight.

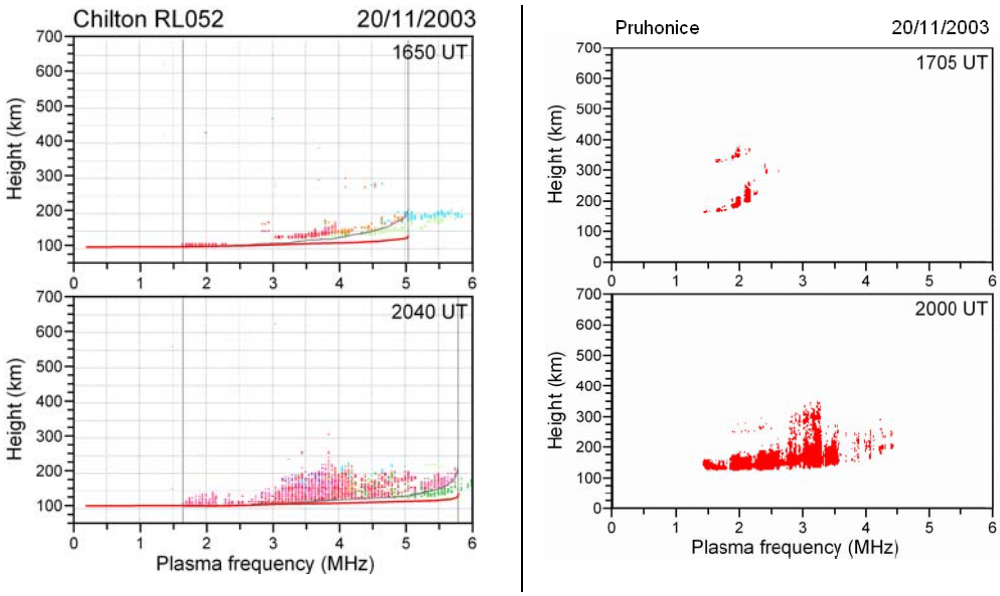

Figure 29. Left: Ionograms from Chilton station. Right: Ionograms from Pruhonice station. Figure adapted from Blanch et al. 2005.

On the contrary, from 18:00 UT to 23:00 UT, El Arenosillo ionosonde recorded a significant increase in foF2 and hmF2, and a strong spread F condition (echoes due to irregularities on the electron density) was clearly observed, lasting practically the whole night of 20 November. The Es layer also appeared above this mid-low latitude station, although not as strong as over the other two stations, and it did not hide the F region on the ionograms (right ionograms in Fig. 28). This sporadic E layer persisted only three hours over the El Arenosillo station.

In figure 30 it is compared the evolution of the plasma frequency as a function of time above Chilton and El Arenosillo during this storm with that of the previous day (considered as a reference). It can clearly be seen that the contour plot of fig. 30, corresponding to Chilton for the disturbed day, only accounts for the contribution of the Es layer during the time interval 16:50–22:30 UT, approximately. There are no F-region profiles available for that time interval because of the blanketing effect. However, direct comparison of the plasma frequency evolution above El Arenosillo between the pre-storm and the storm day, allows observing that the daily variation of 20 November behaves quite similar to that observed for the previous day, up to early afternoon, despite the larger density around midday. In the early evening, an enhancement of plasma frequency (by a factor of 3 to 4) is clearly stated during the initial phase of the

storm (from 18:00 UT onwards). Simultaneously, the F region is lifted and one can see that it also spreads in altitude (see figure 30).

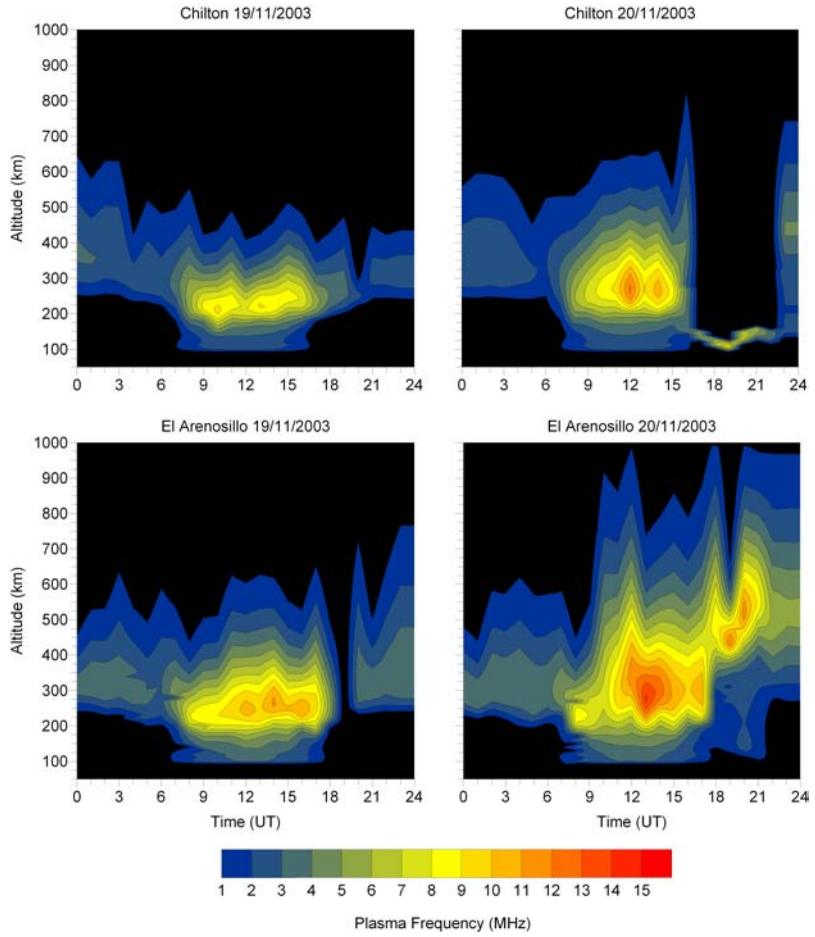

Figure 30. Time-altitude cross-section plots of plasma frequency above Chilton (top plots) and El Arenosillo (bottom plots). Figure obtained from Blanch et al. 2005.

4.3.3 Effects on the electron density in the E layer

The sequence of the plots in plate 5 shows the evolution of the effects of the geomagnetic storm on the electron density in the E layer over Europe. Dotted lines represent the geomagnetic latitude, dots represent the location of the ionosondes in geographic coordinates (see also fig 23) and electron density levels (in cm^{-3}) are represented by a color code. The lowest value of the color scale for the electron density is the minimum that the ionosonde can detect; $1.24 \cdot 10^4$ cm^{-3} taking into account eq. 17 with a frequency of 1MHz (the minimum detectable by the digisonde). Looking at the sequence it is possible to see that the electron density in the E layer have normal values (defined in table 2) before the storm started and also some hours later. The first significant effects of the

storm are observed at 14:00 UT, 6 hours after the onset of the storm, at the Abisko station around 65º geomagnetic latitude, showing electron densities in the E layer larger than $4 \cdot 10^5$ cm^{-3} (see normal values in table 2) while at the rest of latitudes there are no effects. At 16:00 UT, the effect of the enhancement of the electron density appears at sub-auroral station of Juliusruh, in Germany. At that moment there were still no visible effects at lower latitudes. One hour later, the electron density at Juliusruh becomes larger than 10^6 cm^{-3} (normal values for F region, see table 2) and the first effects appear over Chilton. At 18:00, the electron density in the E layer strongly increases at all stations located between 45º and 55º. It is important to notice that there are no ionosonde data available for this time at higher latitudes due to the absorption in the E layer by the enhanced electron density. The maximum of the effects in the electron density occurred at 19:00 UT with values larger than 10^6 cm^{-3} over 55º geomagnetic latitudes, larger than $2 \cdot 10^5$ cm^{-3} at 50º geomagnetic latitude and values around 10^5 cm^{-3} at latitudes lower than 40º geomagnetic latitude. Except for the observation of an increase over Chilton at 22:00 UT, maybe due to local effects, the electron density started to decrease slowly and reached its normal values early in the morning on 21st November.

4.3.4 Effects on the Total Electron Content

In figure 31 the effects of the geomagnetic storm on the Vertical Total Electron Content over the European sector are presented. The color scale indicates the levels of VTEC in units of 0.1 TECU (10^{15} m^{-2}). It is possible to observe that under quiet conditions (snapshot 30a), VTEC values are lower at the nightside and at high latitudes. VTEC starts to increase around the auroral oval down to around 60º N at the initial phase of the storm (snapshot 30b).

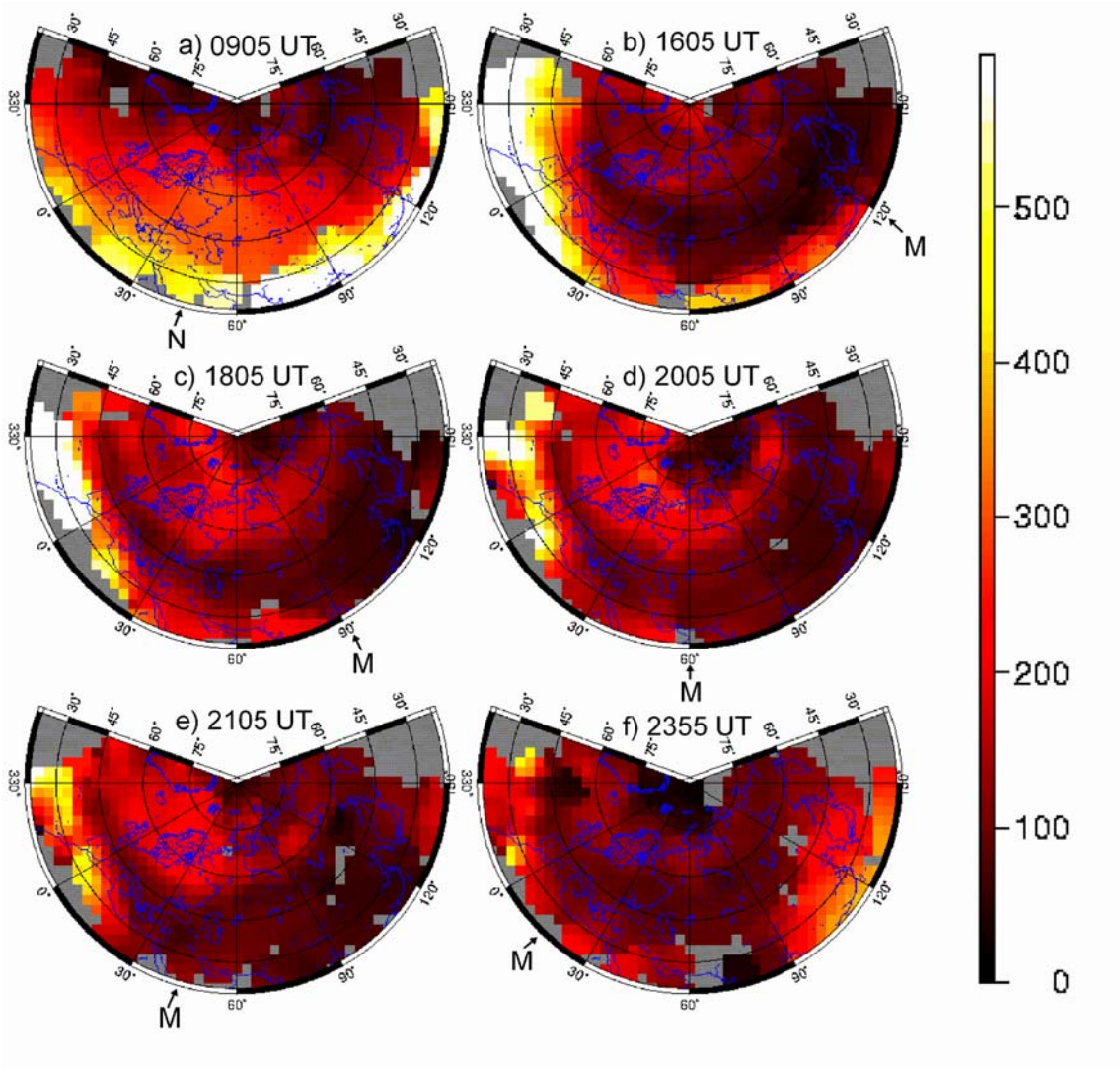

Figure 31. Spatial distribution of the VTEC over Europe for the 20th November 2003. N means noon and M midnight. Figure modified from Blanch et al. 2005.

From 18:00 to 21:00 UT (snapshots c, d, e), the increase of electron density in the auroral oval is clearly seen. At the same time, it can be noticed the existence of a thin latitudinal belt between 55º-45º N, with lower VTEC values than those at the higher latitude, extending into the longitude sector 350º–30º E, being wider into the longitude sector 50º–120º E. Additionally, an enhancement of the VTEC is clearly stated on the latitudinal belt between 45º-30º N into the longitude sector 330º–60º E approximately.

This effect was expected to be observed from the ground ionosonde data; but the anomalous storm Es layer hid the F-region evolution above Chilton and Pruhonice.

4.3.5 Effects on the external magnetic field

In plate 1 the evolution of the X component (northward) of the external magnetic field contribution during the storm is shown. Circles indicate the position of the magnetic observatories whose data were used in this study (see also fig. 24) and dotted lines are isolines of geomagnetic latitude. The first effects of the storm on the external magnetic field were observed at 9:00 UT (one hour later the onset of the storm) at high latitudes as a positive contribution; being stronger one hour later. At 12:00 UT, the positive effect expanded equatorward. At the same time, a negative contribution was observed at lower latitudes in the map. At 13:00 UT, the external magnetic field contribution became negative at high latitudes, positive from 65º to 55º N geomagnetic latitudes and negative at lower latitudes. These effects became stronger at 14:00 UT. From 14:00 UT to 19:00 UT, the positive effect moved to lower latitudes and to the west. The negative contribution at high latitudes moved down to 60º N and the negative contribution at lower latitudes became more negative with a maximum at 19:00 UT when the positive structure disappeared. From 20:00 UT onwards, most of the contribution of the X component is negative and at 24:00 UT starts to decrease in intensity.

The X component of the magnetospheric contribution estimated by POMME3 model is shown in plate 2. At 13:00 UT, the magnetospheric field starts to become slightly negative at the lowest part of the map. This effect is more visible at 14:00 UT. This negative contribution extends poleward and increasing in intensity reaching the maximum at 19:00 UT. After that, it starts to move back to normal values.

In plate 3 it is shown the X component of the external contribution once its magnetospheric part was extracted. The evolution of the effects follow the same pattern that the effects of the total external field with the exception of the negative part of the lowest part of the map. In this case it reaches negative values but less intense. Finally, at 20:00 UT, when the positive structure disappears, it is possible to observe that the remnant contribution is of about -100 nT all over Europe in comparison to the -400 nT for the total external field.

In plate 4 it is shown the Z component of the external contribution once its

magnetospheric part was extracted. First significant effects appear at 12:00 UT at high latitudes being negative at around 65º geomagnetic latitudes and slightly positive at about 60º geomagnetic latitudes. These effects intensify at 13:00 UT and mostly at 15:00 UT when the negative and positive structures are clearly observed and moved to lower latitudes. At 16:00 UT, it is possible to observe a positive contribution at high latitudes, a negative contribution from 55º to 65º N geomagnetic latitudes and a positive contribution from 45º to 55º N geomagnetic latitudes. During the sequence from 14:00 UT to 19:00 UT it is possible to observe that the negative structure moves slightly equatorward down to 55º and in the west direction. At the same time, the positive structure observed at lower latitudes also moved equatorward down to 40º. At 20:00 UT both, positive and negative structures disappeared from the map leading with a positive contribution only at high latitudes.

4.4. Discussion

4.4.1 Effects on the vertical structure

According to the Report UAG23A of the World Data Center A (1978) and its revised edition (1986), the Es layer observed in the Pruhonice ionograms before 20:00 UT (fig. 29), and that in the lower-middle latitude station El Arenosillo ionograms from 18:00 to 19:00 UT (Fig. 28) are classified as Es layer k-type (particle E). A particle E layer is a thick layer which is sometimes seen at greater heights up to about 170 km in the nighttime, having much higher critical frequency than a normal E layer. It is produced by precipitating particles moving into the lower atmosphere during ionospheric disturbances. See the upper panel of the figure 32 for an example. The Es layer observed in the Chilton ionograms before 20:00 UT (fig. 28 and fig. 29) is classified as standard r-type (retardation). A r-type layer is an obliquely reflected particle E layer whose trace shows an increase in virtual height near the top frequency. As the critical frequency of the E region exceeds the lowest frequency of F layer, the trace can blanket partially or completely F layer traces. If the critical frequency of the E region does not exceed the lowest frequency of F layer, the Es is classified as a particle E layer (k-type Es). See the middle panel of figure 32 for an example of Es r-type layer. The Es layer present in the Chilton and Pruhonice ionograms recorded after

20:00 UT (fig. 29) are classified as the standard a-type (auroral). Auroral Es types are usually observed only at high latitudes (King, 1962) but can be observed at mid-latitudes in association with auroral activity (Brown and Wynne, 1967). See the bottom panel of figure 32 for an example of an Es a-type layer.

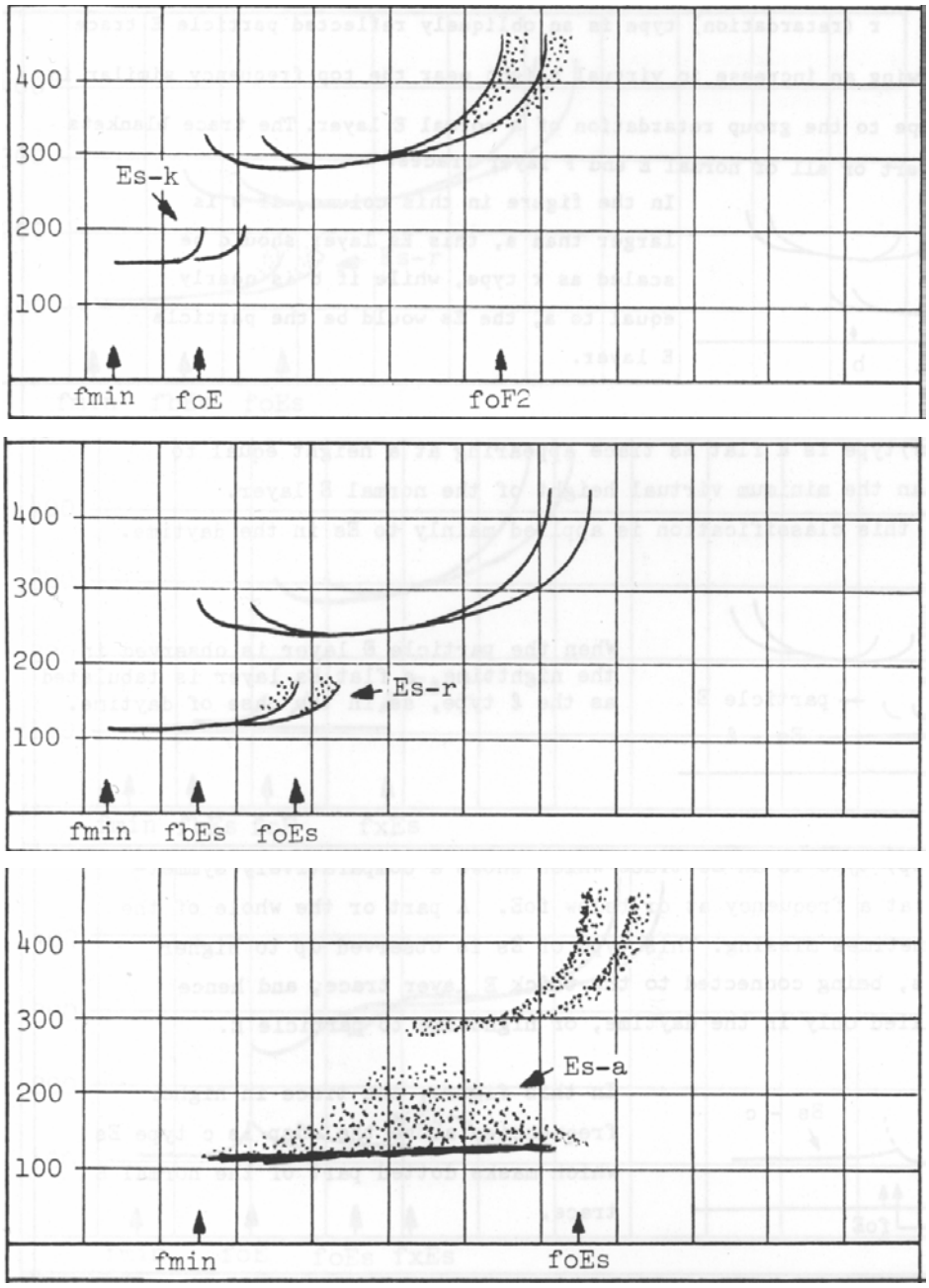

Figure 32. Examples of Es layer. Top panel k-Es (particle), middle panel r-Es (retardation), bottom panel a-Es (auroral). Figures obtained from the URSI Manual of ionogram scaling, 1986.

In the E region, the effects of a geomagnetic storm depend on latitude. At high latitudes, the particle precipitation into the auroral oval is the responsible of the formation of the auroral Es layer (Lastovicka, 2002). The formation of the particle

E layer observed at mid latitudes is assumed to be due to the precipitation of energetic neutral atoms with energies of 1-100 keV from the ring current zone according Lyons and Richmond (1978) and Tinsley (1979). These energetic neutral particles are formed as result of a charge-exchange interaction of the ring current ions with neutral hydrogen and are no longer bound by the Earth's magnetic field. Some of them escape to the interplanetary space and others are injected to the Earth's upper atmosphere. Particles that enter in the atmosphere interact with gas particles and lose part of their energy which is spent on ionization.

According to Prölss (1995) and references therein, the uplifting of the F layer is produced by vertical drift of the plasma along the inclined field lines induced by an increase of the electric fields of magnetospheric origin or by an enhancement of the equatorward horizontal thermospheric circulation. The uplift of the F layer produces both, the spread-F condition and an increase in the electron density (see figure 30) due to the lower electron loss rate at higher altitudes (Lastovicka, 2002).

4.4.2 Effects on the Total Electron Content

Direct comparison between figures 30 and 31 shows that this storm caused positive and negative effects at different latitudes in the European evening sector. As introduced in section 3.1, the negative storm effect can be explained by changes in the neutral composition and its equatorward expansion. The positive storm effect observed at high latitudes is due to direct particle precipitation as it was explained in section 3.2. As also discussed in section 3.2, the positive latitudinal belt observed at 45º-30ºN could have been caused by large gravity waves (TADs) but only if its duration was lower that a few hours. As the observed enhancement of VTEC was a long-lasting effect, persisting for more than 10 hours after onset, it might be caused by change in the neutral composition. Burns et al. (1995) demonstrated that there are strong enhancements in the $[O]/[N_2]$ ratio in the evening sector of the winter middle latitudes during geomagnetic storms. Enhancements of $[O]/[N_2]$ can reach a small band of 10º of latitude wide between 40º and 50º. These changes in the $[O]/[N_2]$ ratio occur because pressure gradient forces driven by Joule heating in

the polar region push air depleted of N_2 from higher latitudes in the winter hemisphere into this middle-latitude region. Thus, from eq. 13, an enhancement of $[O]/[N_2]$ rate produces an increase of the electron density. Penetration of electric field as a possible explanation of positive effect was also rejected because the positive belt was not observed immediately after the onset of the storm.

Therefore, it is believed that the changes in the neutral composition generated by the storm are the cause of the VTEC effects at mid latitudes and particle precipitation is the cause of the enhancement of the total electron content at high latitudes.

4.4.3 Effects on the external magnetic field

It has been seen that the external magnetic field was strongly disturbed during the main phase of the storm (14:00-19:00 UT). From the X component (plate 1) it is possible to distinguish two different features. A large-scale effect observed at latitudes lower that 55º and a small-scale effect that move equatorward from high latitudes.

The large scale effect is identified as the ring current effect that weakens the X component of the total magnetic field (plate 2). The small-scale effect was supposed to be a local effect due to the increase of the electron density in the E region that intensified electric currents in the ionosphere. Comparing the evolution of this small-scale effect (plates 1, 3 and 4) with that of the electron density in the E layer (plate 5) it is possible to observe that the small-scale structure move to the west direction while the increase of the electron density in the E layer move equatorward but not to the west. Moreover, once the small-scale structure evacuates from the west, there are still large values of the electron density in the E layer. For this reason it is concluded that the increase of the electron density in the E layer is not the direct cause of this structure. If the increase of the electron density produced any effect, it could be neglected by the more intense effect of this small-scale structure. As the small-scale structure, is fixed in local time, it suggests that it will be due to a magnetospheric part not modeled by the POMME3 model. As explained in section 4.2.3, POMME3 model

reproduces the ring, tail and magnetopause contributions, but not the field aligned currents (FACs) and auroral electrojet contributions. In section 2.3 was explained that during geomagnetic storms, the intensity of the FACs increases and it produces an intensification of the auroral electrojets. From figure 15 it is observed that in the dusk sector, the auroral electrojet is directed eastward and the closing current is oriented westward producing a positive and a negative effect respectively which can be identified as the effects observed on the external magnetic field. This fact leads to the hypothesis that the auroral oval expanded equatorward and the effects of the auroral electrojets could be observed to lower latitudes than usual. Looking to the auroral indices (defined in section 2.3) it is possible to see that the AU index, which describes the intensity of the eastward electrojet, was close to 0 and even changed to negative values during this period. This means that the eastward electrojet was weakened (or disappeared) or that the observatories that measured it did not observe it because the eastward auroral electrojet was moved to lower latitudes (figure 33).

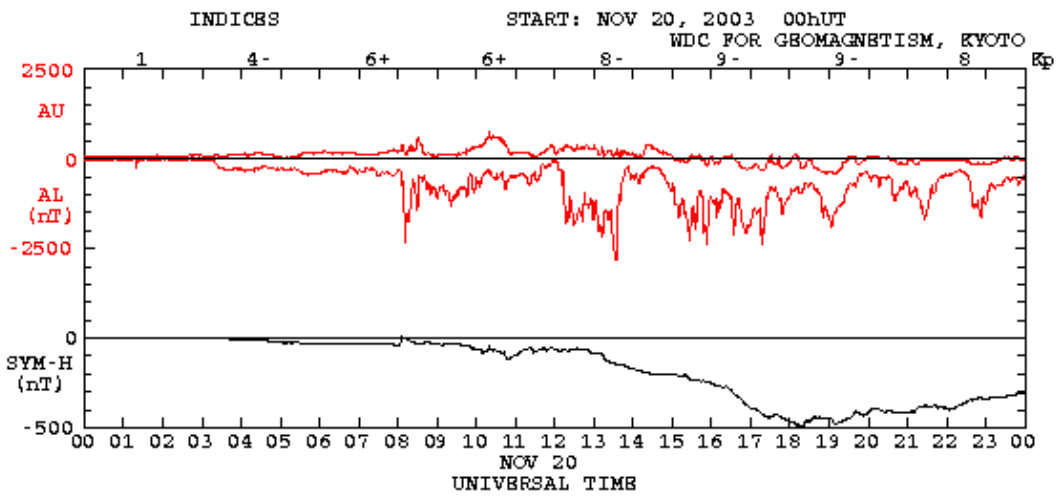

Figure 33. Auroral indices, AU and AL. SYM-H is the symmetric disturbance field in H (is essentially the same that Dst index for 1 minute data). Data obtained from the World Data Center Kyoto.

Popov et al. (2001) defined a numerical method to model the equivalent ionospheric currents using magnetic field observation from meridian magnetometer chain data. The Danish Meteorological Institute applies this method with data from the Greenland magnetometers chain to estimate the equivalent ionospheric current from 65º to 85º geomagnetic latitudes. In the

upper panel of figure 34, the equivalent ionospheric currents obtained with this method for a referenced day (19th November 2003) are depicted. It is possible to observe the westward current in the morning sector at geomagnetic latitudes below 75º and the eastward current in the evening sector that peaks between 75º and 70º geomagnetic latitudes. In the bottom panel of figure 34, the ionospheric equivalent current for the disturbed day (20th November 2003) are shown. In this case, in the evening sector not any eastward current can be seen. As with the AU index, this fact can be explained by a weaker eastward electrojet or by its displacement to lower latitudes.

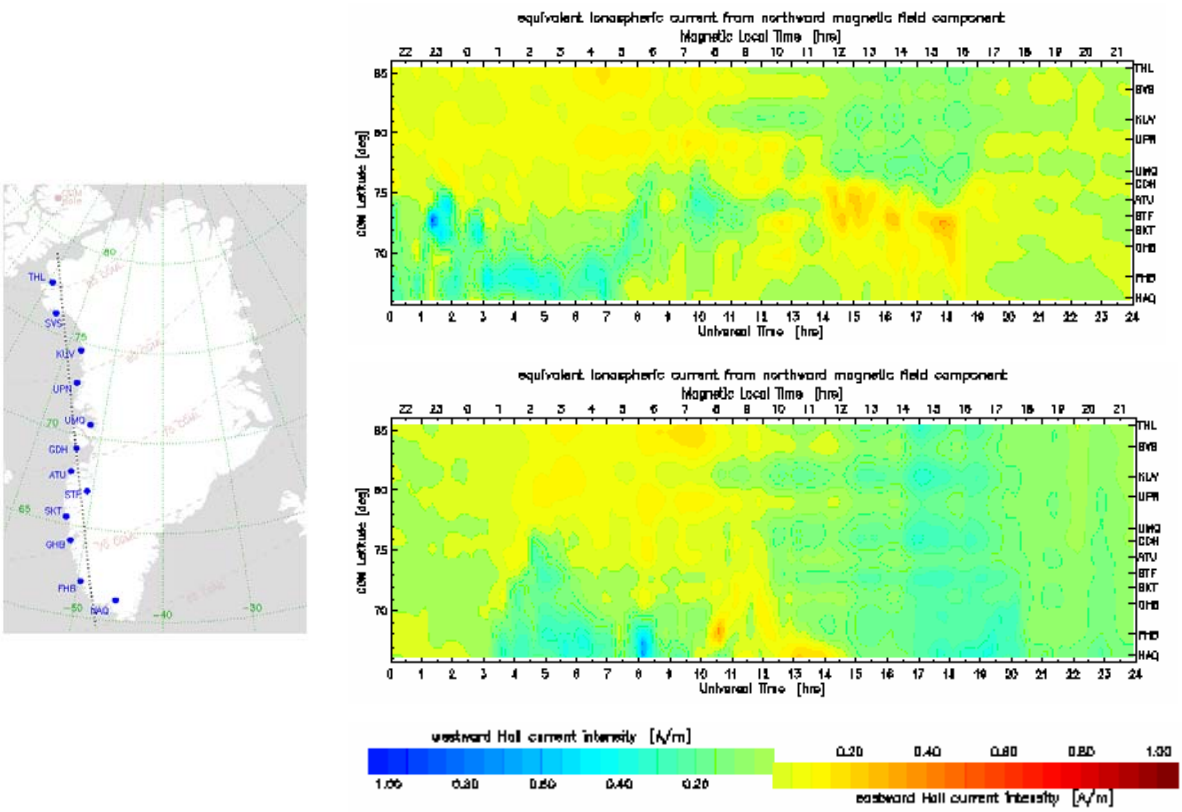

Figure 34. Left: Greenland magnetometers chain. Right: Equivalent ionospheric currents for 19th November 2003 (top) and 20th November 2003 (bottom). Image and plots obtained from the Danish Meteorological Institute Atmosphere Space Research Division web page (http://web.dmi.dk/projects/chain/).

These facts leaded to interpret the small-scale effect observed on the external magnetic field as the effect of the polar ionospheric currents that were displaced equatorward. In figure 35, the position of these currents is depicted. The dashed lines represent the approximate position of the currents and the arrows represent their direction. The electrojet location is estimated using both, the change in the sign in the Z component and the maximum variation in the X

component. It is important to mention that the structure of the currents is more complex than what it is shown here but the purpose to draw them on the map is only descriptive. Note that at the highest part of the map there are only two stations to estimate the position of the westward current.

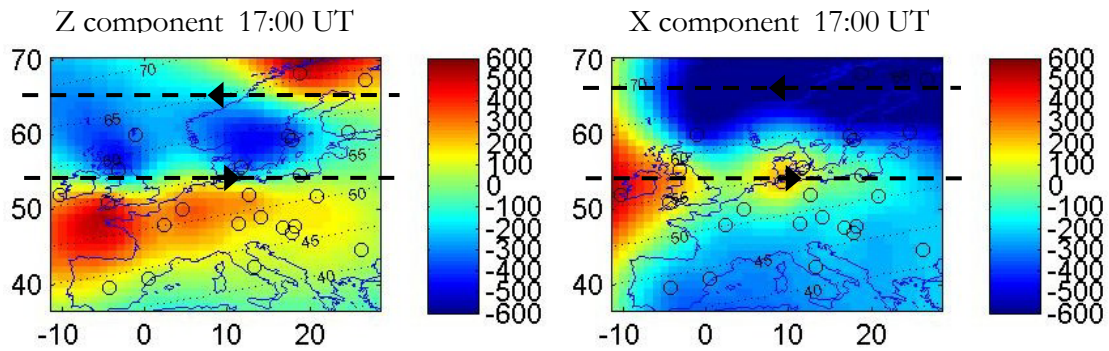

Figure 35. Description of the magnetic variations of the external field at 17:00 UT for Z component (left) and X component (right). Dashed lines represent the currents responsible of these variations.

In figure 36, a zoom of the Z component of the magnetic data for some observatories from high to mid latitudes in the sector of 15º E longitude is shown. From 17:00 to 20:00 UT there are two changes of sing, one between ABK and UPS observatories and other one between BFE and NGK. Close to 17:00 UT it is possible to observe an increase of the magnetic field at ABK station (red rectangle). At lower latitudes (UPS and BFE observatories) it is observed a decrease (blue rectangle) and at NGK and BDV another increase. Same thing is also clearly observed around 18:00 UT. This change of sing in the Z component is explained by the existence of a westward current flowing in the ionosphere between ABK and UPS and an eastward current between BFE and NGK as it has been depicted in figure 35.

The eastward current located at latitudes of 50º is identified as the eastward electrojet, and the westward current at higher latitudes is interpreted as the current closing the system (figure 15). As the auroral oval moved to lower latitudes, it can also explain the large electronic density in the E layer at geomagnetic latitude of 55º N due to particle precipitation.

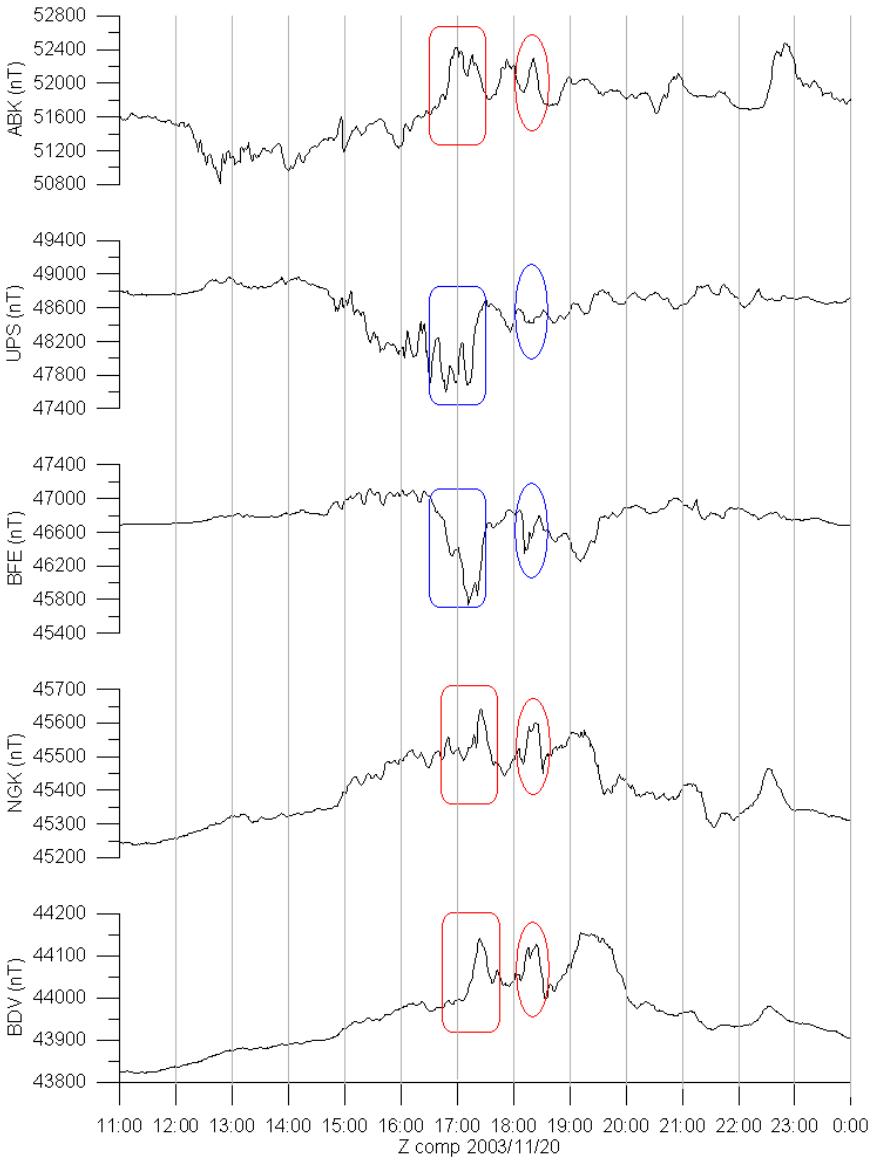

Figure 36. Z component of the magnetic field at different observatories sorted from higher to lower geomagnetic latitude for the 15º E sector.

It should be mention that during the very large geomagnetic storm of 13th March 1989 (Dst reached -589 nT), the eastward electrojet was also located to lower latitudes than usual (Allen et al., 1989). AU index values were also close to 0 or negative and the World Data Center C2 derived special midlatitude auroral electrojet indices using data from North America sites closer to the electrojet (Kamei et al., 1989).

CHAPTER 5: Conclusions

This work has been very useful to understand the mechanisms that produce geomagnetic storms and how the ionosphere responds to those disturbances. From the 20th November 2003 geomagnetic storm it has been observed that the variations on the ionosphere depend on the latitude and altitude and on the storm intensity. Thanks to different instruments and methods to process the data is has been possible to observe:

- A large enhancement of the electron density in the E layer which was evident in the ionograms as a sporadic E layer (auroral, retardation and particle types) down to latitudes of 37ºN. At subauroral latitudes, the sporadic E layer was due to particle precipitation facilitated by the equatorward expansion of the auroral oval. The large electron density blanketed the response of the F layer. At lower latitudes the occurrence of the particle E layer can be attributed to precipitation of energetic neutral particle from the ring current. Aurorae occurred at unusual latitudes as Athens (http://spaceweather.com).

- An uplift of the F region induced by an increase of the equatorward thermospheric circulation which produced an spread of the F layer and an increase of the electron density.

- Two latitudinal belts with anomalous electron density observed from GPS data: one at 55º-45º N with depressed electron density and another at

45º-30º N with enhanced electron density. Both effects were due to changes in the neutral composition driven by the thermospheric circulation.

- The effects of the eastward auroral electrojet at subauroral latitudes which means that it was expanded to latitudes lower than usual.

This analysis showed the benefit of studying the ionosphere from different instruments and the profit to use precise geomagnetic models to estimate the external contributions to the geomagnetic field. From this study it can be shown the necessity of a well distributed network of magnetometers and ionosondes with data of good quality and accessibility.

The next step will be to study the effects of geomagnetic storms on the vertical structure of the ionosphere at Ebre station from ionosonde data during a complete solar cycle to find its standard behavior at different altitudes depending on the onset of the storm, season and storm intensity. This study will be complemented with data from other stations to find the latitudinal dependence of the ionospheric effects in collaboration with the UMLCAR University. Moreover, together with the Institute de Physique du Globe de Paris, POMME3 model will be used for other geomagnetic storms and for a wider area in order to describe the storm-time ionospheric magnetic field. Spherical Cap Harmonic models will be used to represent the equivalent storm-time ionospheric currents.

Plate 1- External magnetic field (X component). 20th November 2003

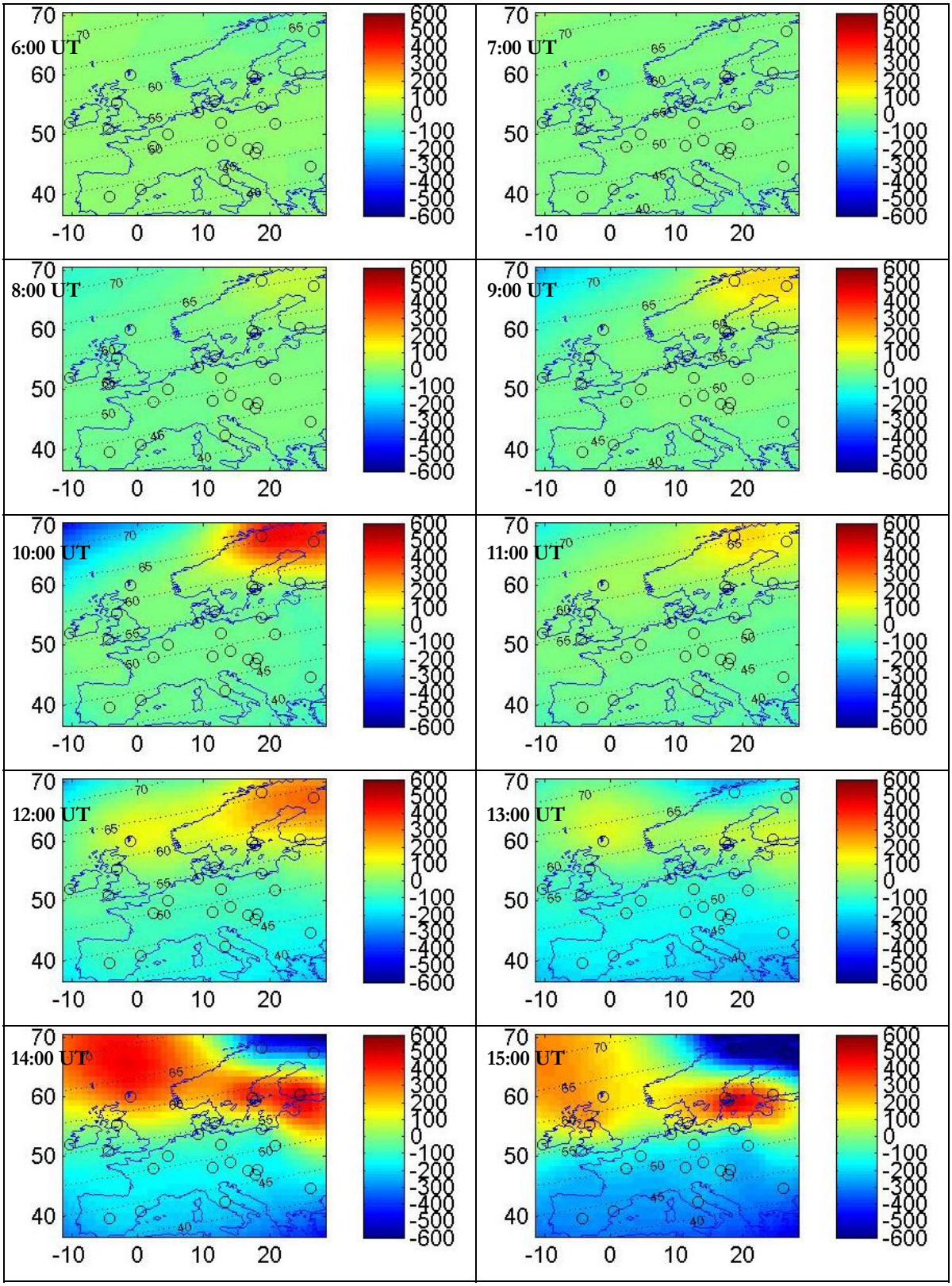

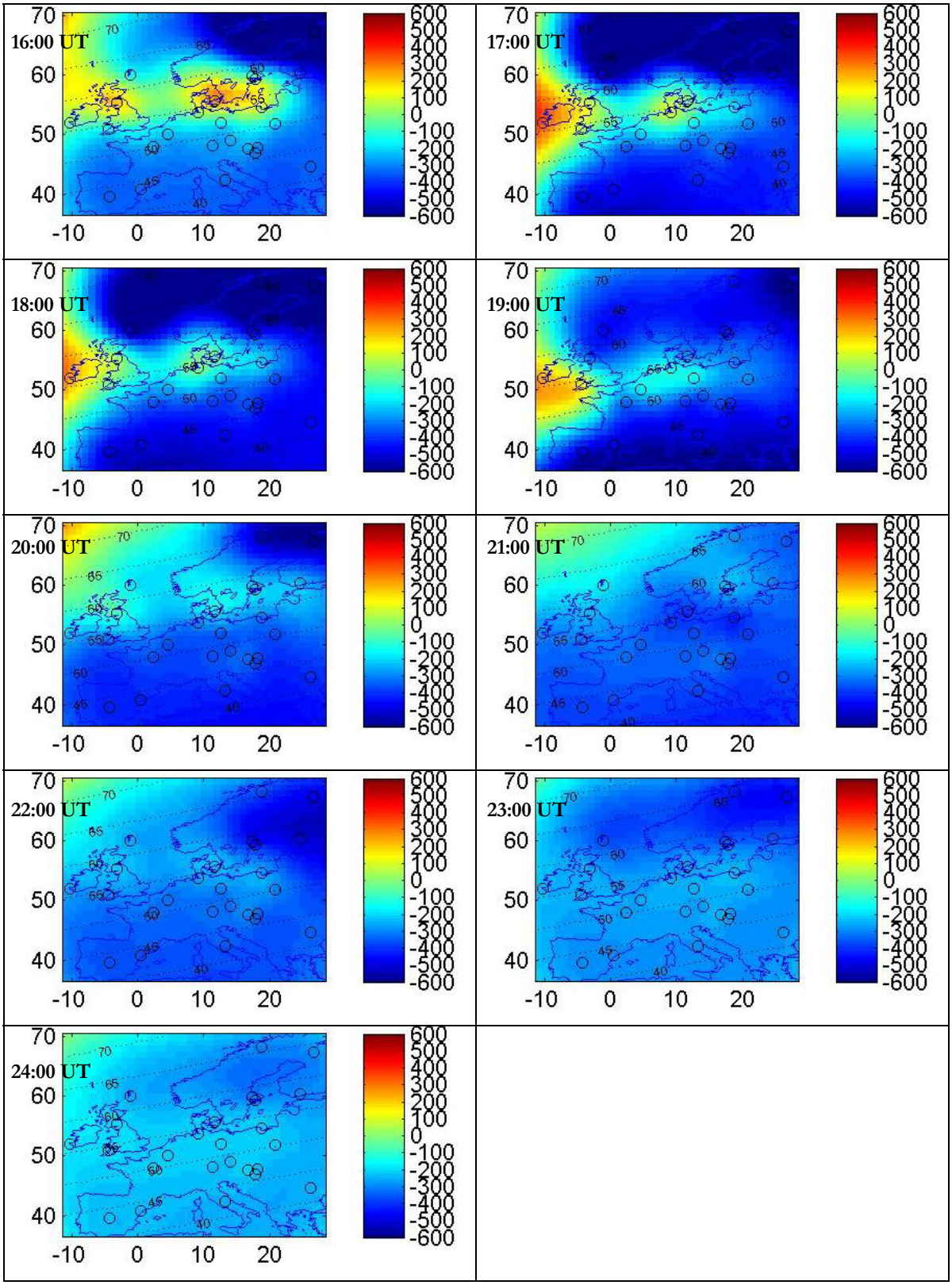
16:00 UT
17:00 UT
18:00 UT
19:00 UT
20:00 UT
21:00 UT
22:00 UT
23:00 UT
24:00 UT
70
60
50
40
-10
0
10
20
600
500
400
300
200
100
0
-100
-200
-300
-400
-500
-600

Plate 2- Magnetospheric magnetic field according to POMME3 model (X component). 20th November 2003

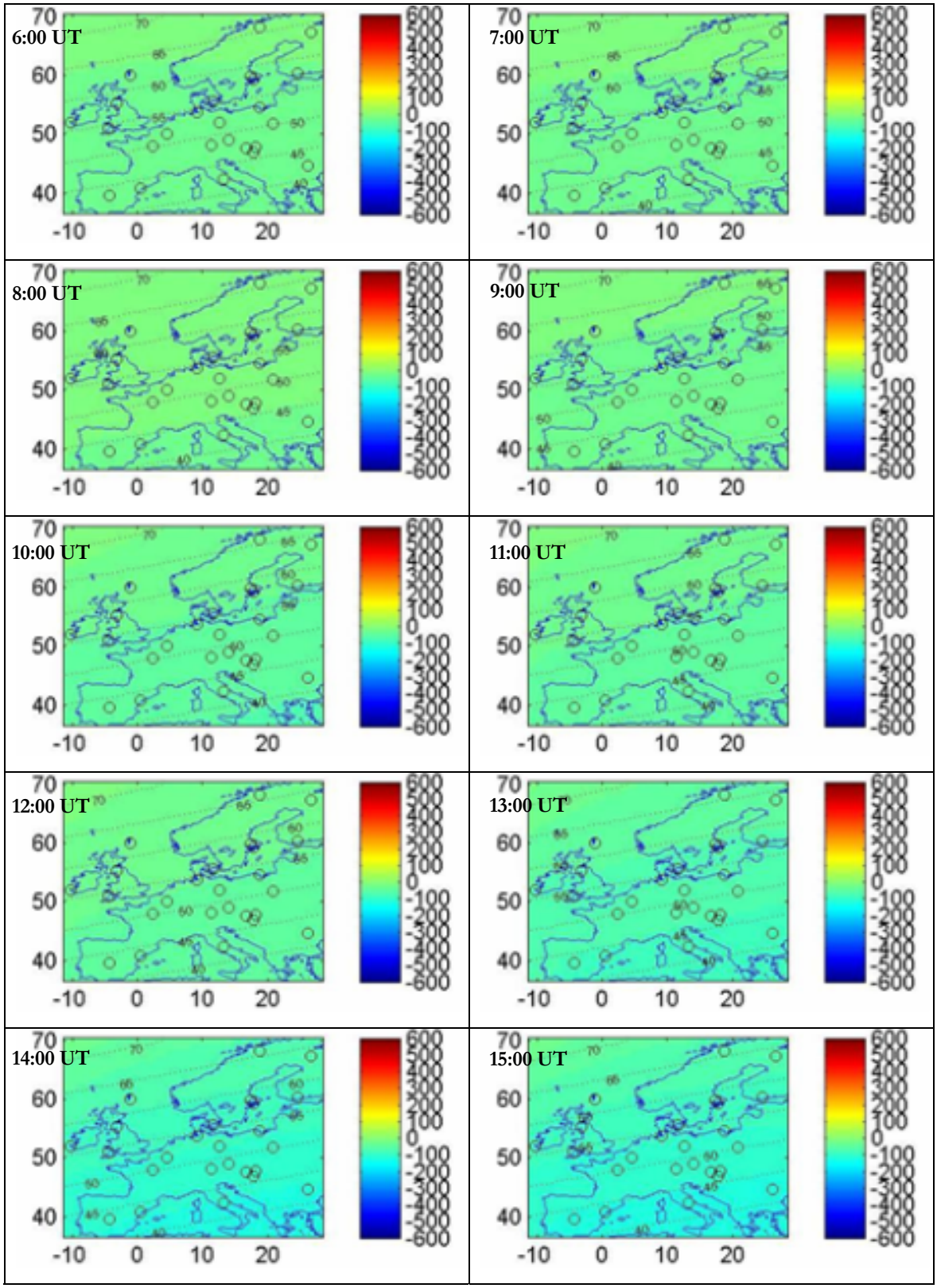

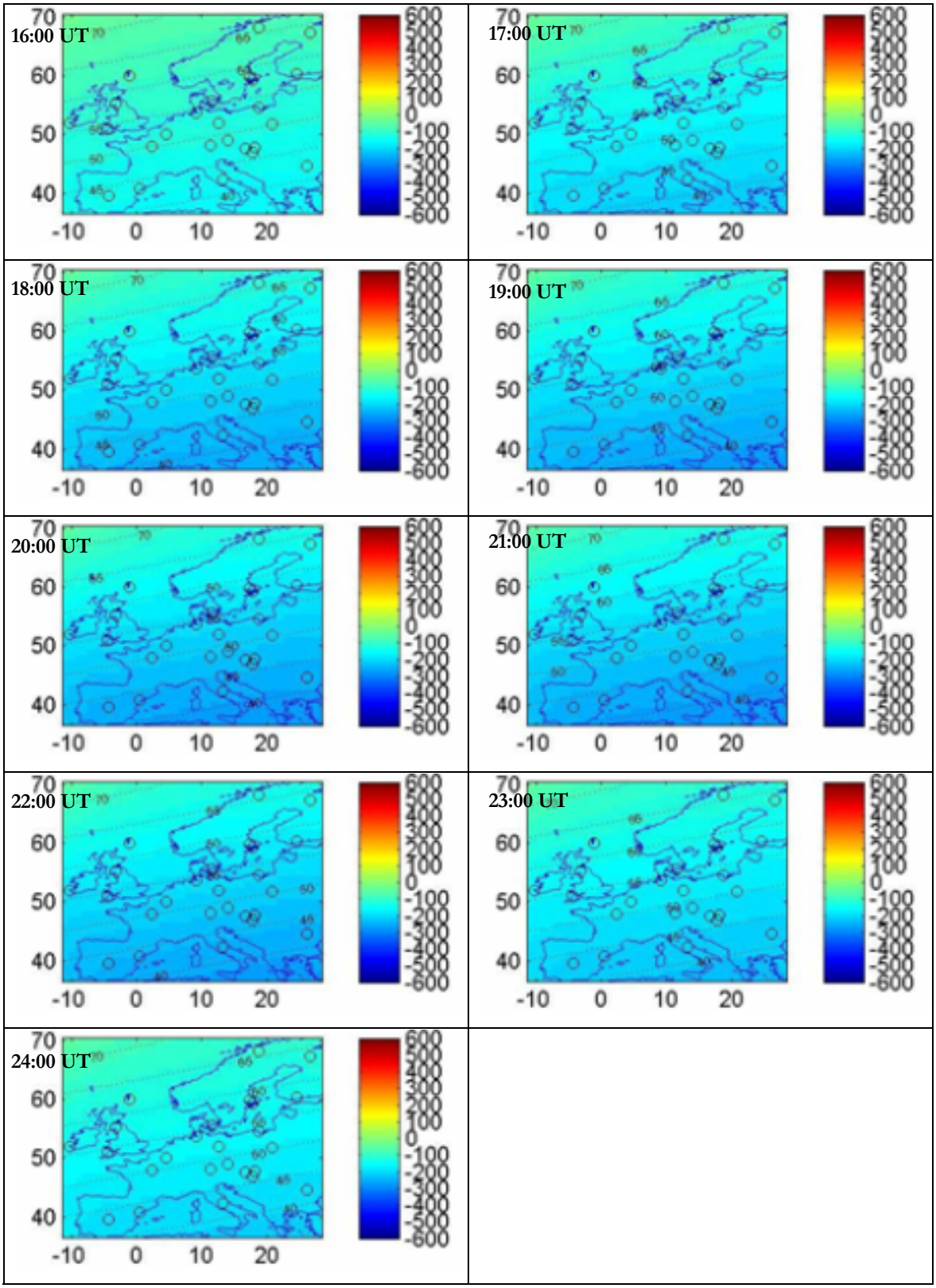
16:00 UT
17:00 UT
18:00 UT
19:00 UT
20:00 UT
21:00 UT
22:00 UT
23:00 UT
24:00 UT
70
60
50
40
-10
0
10
20
600
500
400
300
200
100
0
-100
-200
-300
-400
-500
-600

Plate 3- External magnetic field extracting magnetospheric contribution with POMME3 model (X component). 20th November 2003

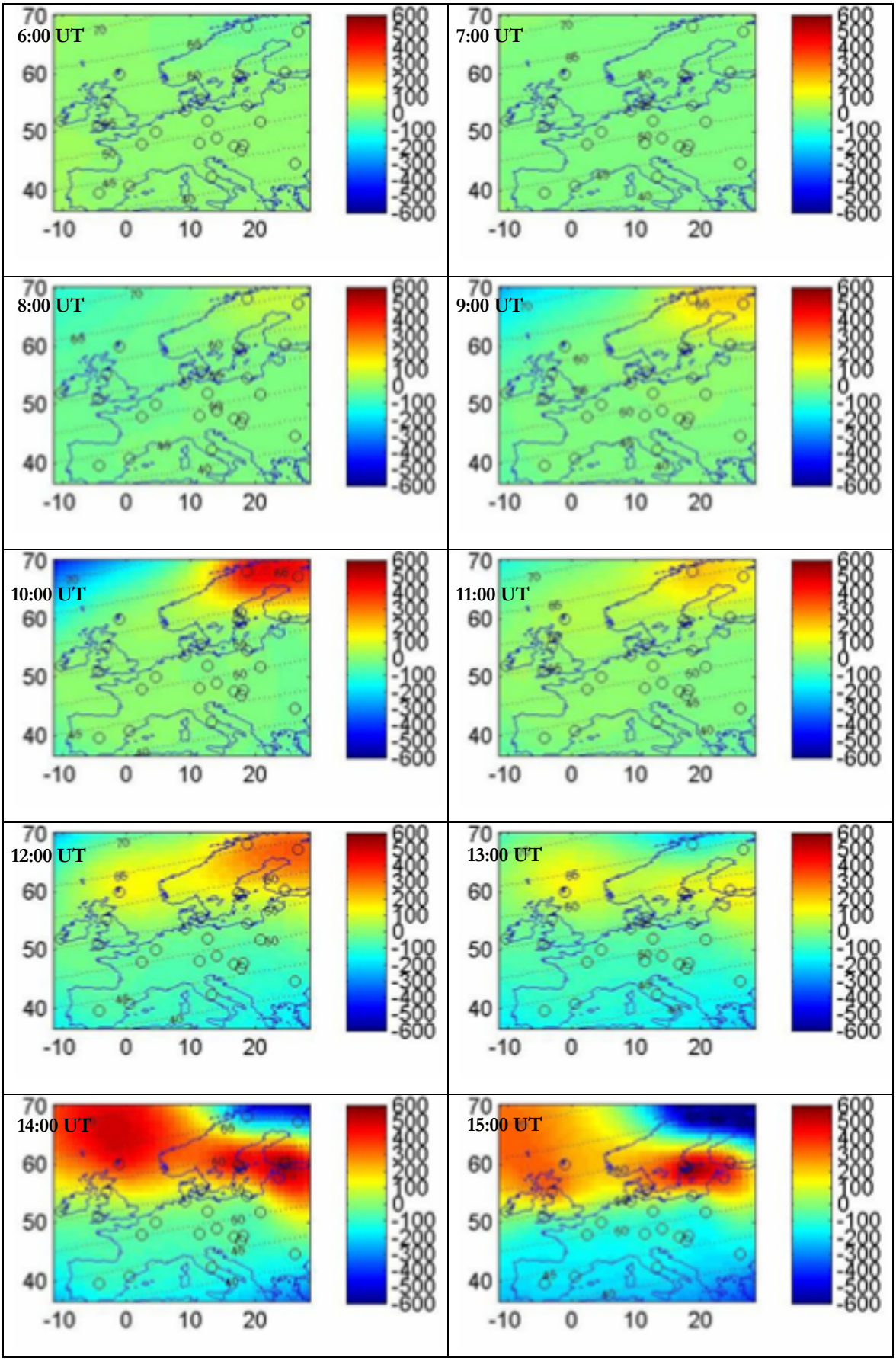

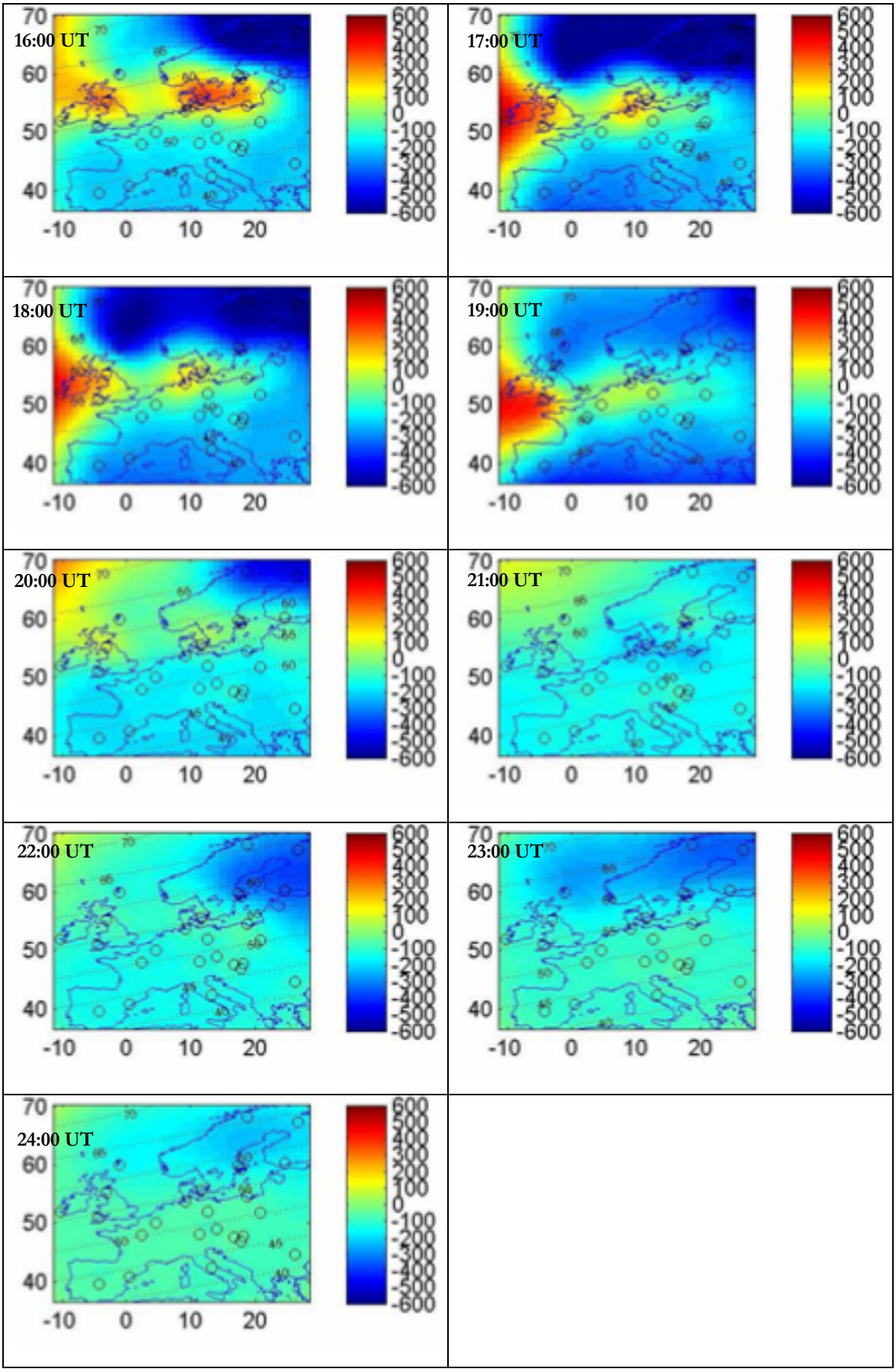
16:00 UT
17:00 UT
18:00 UT
19:00 UT
20:00 UT
21:00 UT
22:00 UT
23:00 UT
24:00 UT
70
60
50
40
-10
0
10
20
600
500
400
300
200
100
0
-100
-200
-300
-400
-500
-600

Plate 4 - External magnetic field extracting magnetospheric contribution with POMME3 model (Z component). 20th November 2003

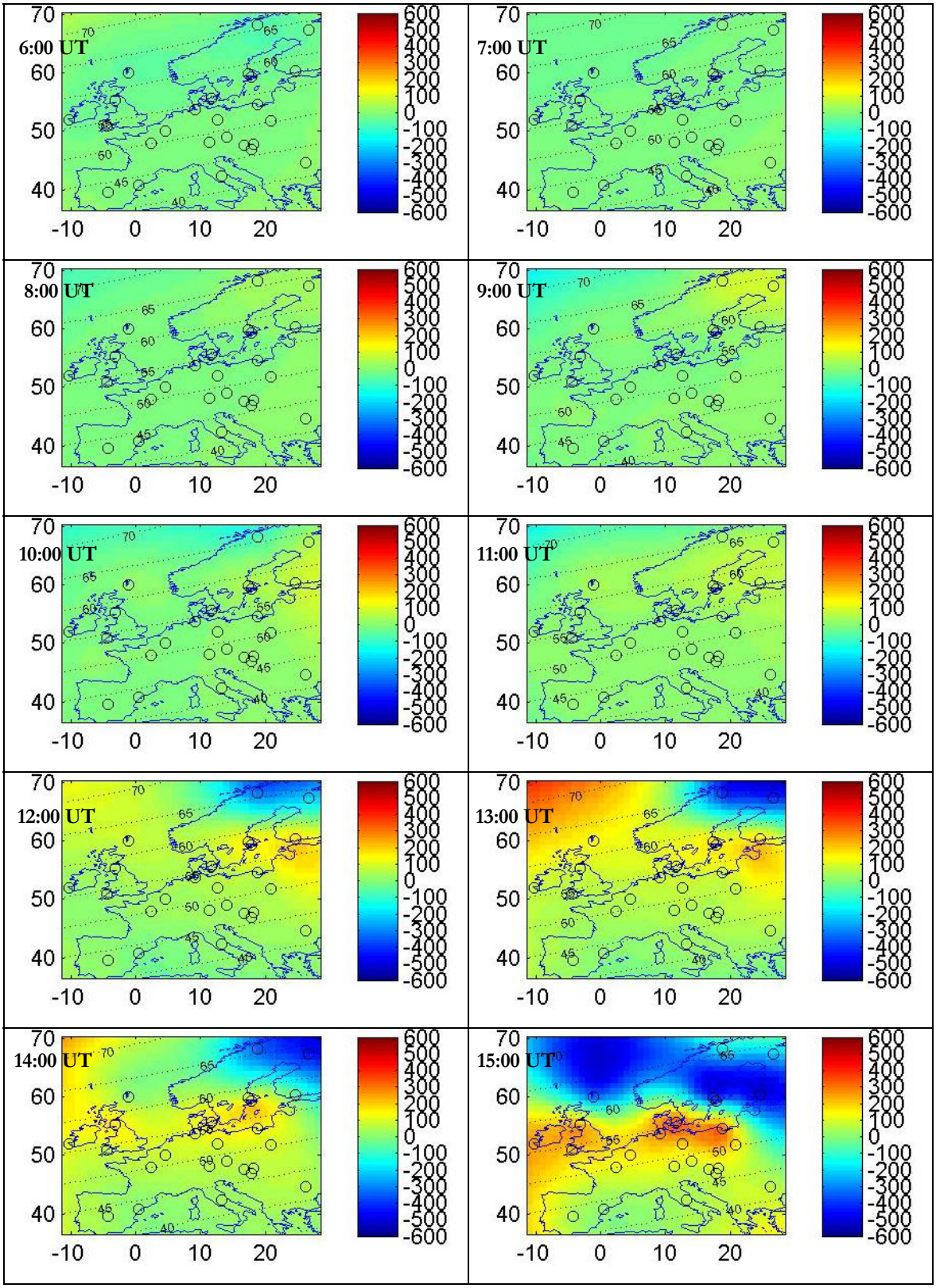

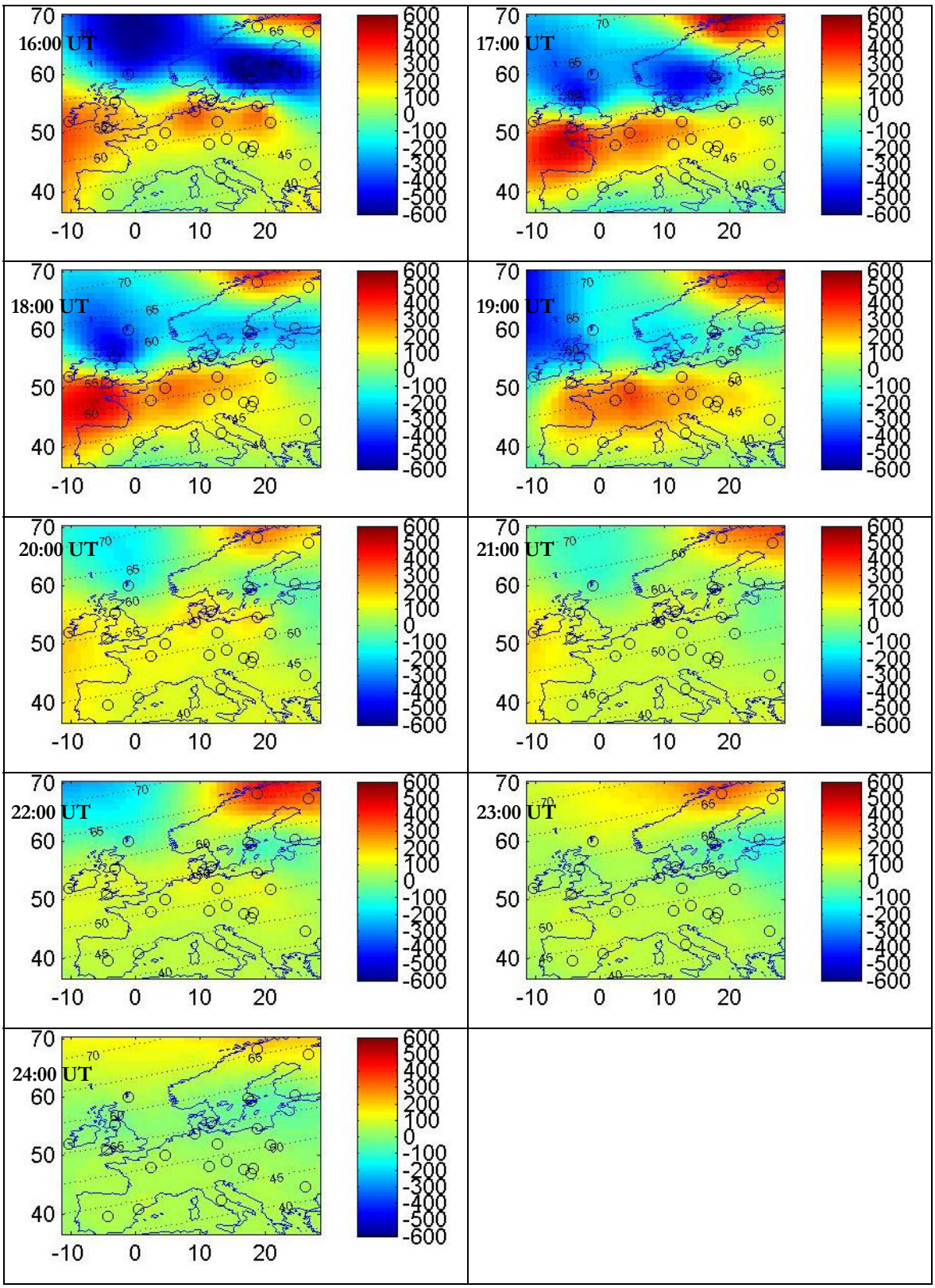
16:00 UT
17:00 UT
18:00 UT
19:00 UT
20:00 UT
21:00 UT
22:00 UT
23:00 UT
24:00 UT
70
60
50
40
-10
0
10
20
600
500
400
300
200
100
0
-100
-200
-300
-400
-500
-600

Plate 5 – Electron density in the E layer. 20th November 2003

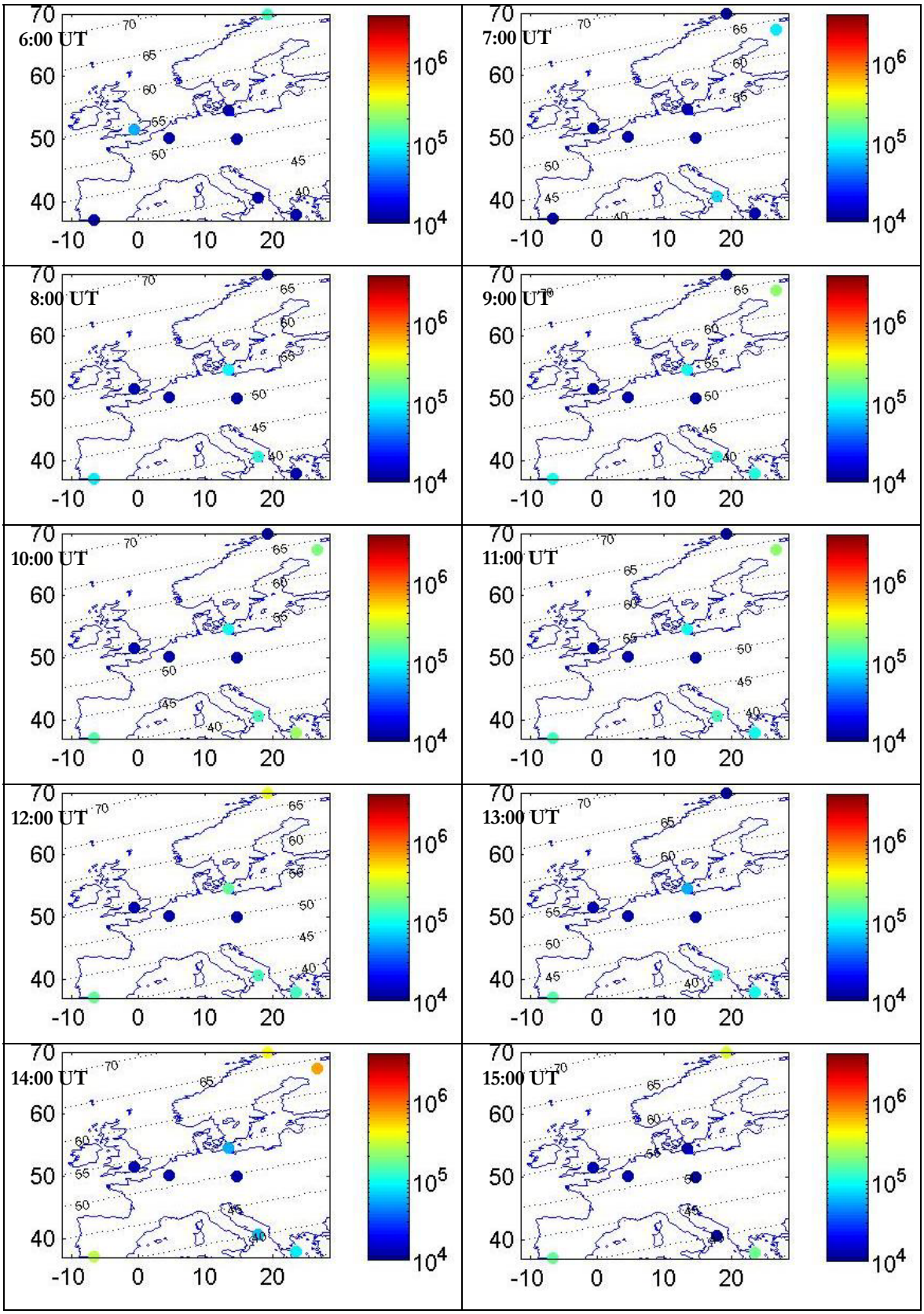

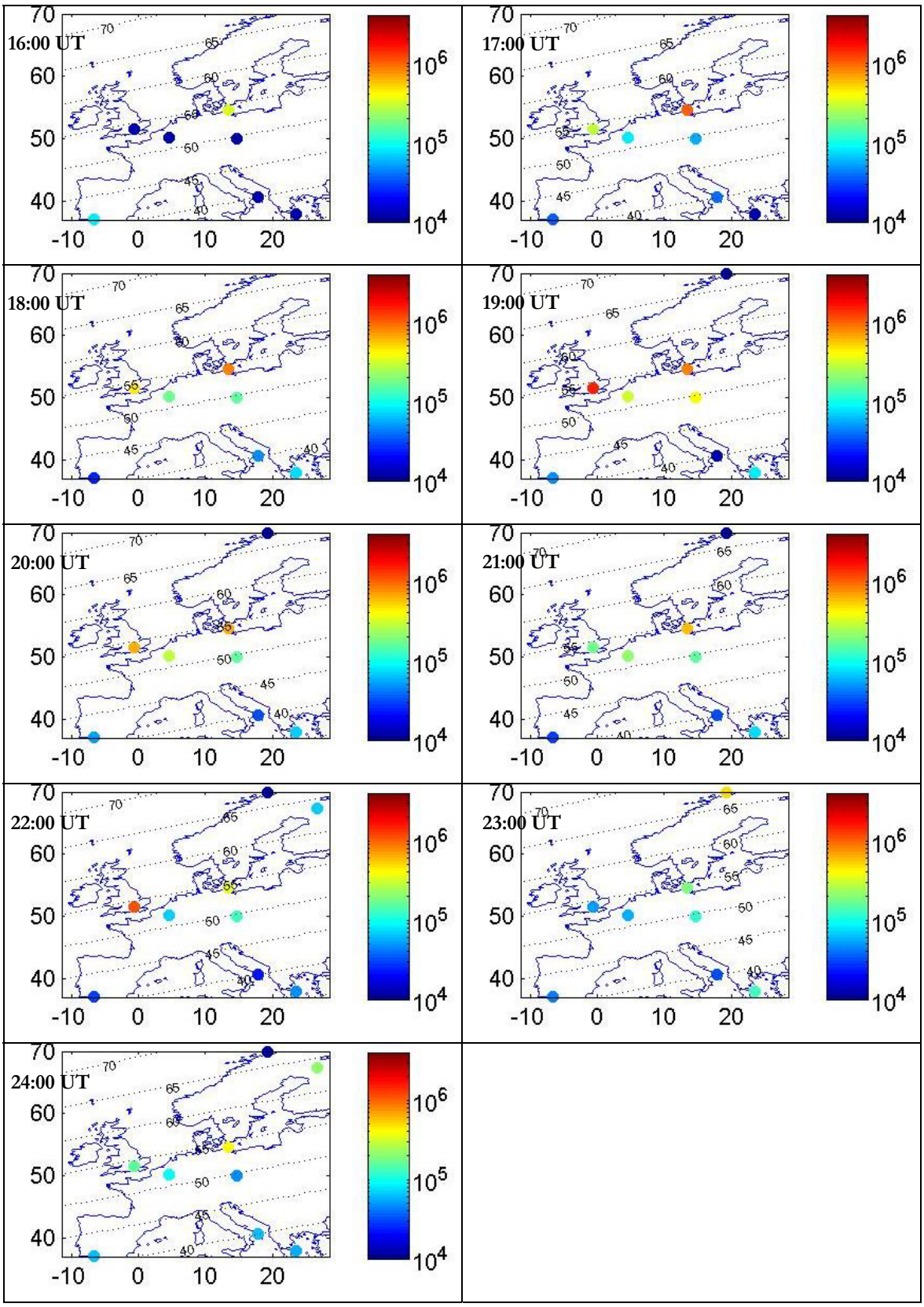
16:00 UT
17:00 UT
18:00 UT
19:00 UT
20:00 UT
21:00 UT
22:00 UT
23:00 UT
24:00 UT
70
60
50
40
-10
0
10
20
10^6
10^5
10^4

Plate 6 – Ground magnetic field (X component) from higher to lower geomagnetic latitude according Appendix C

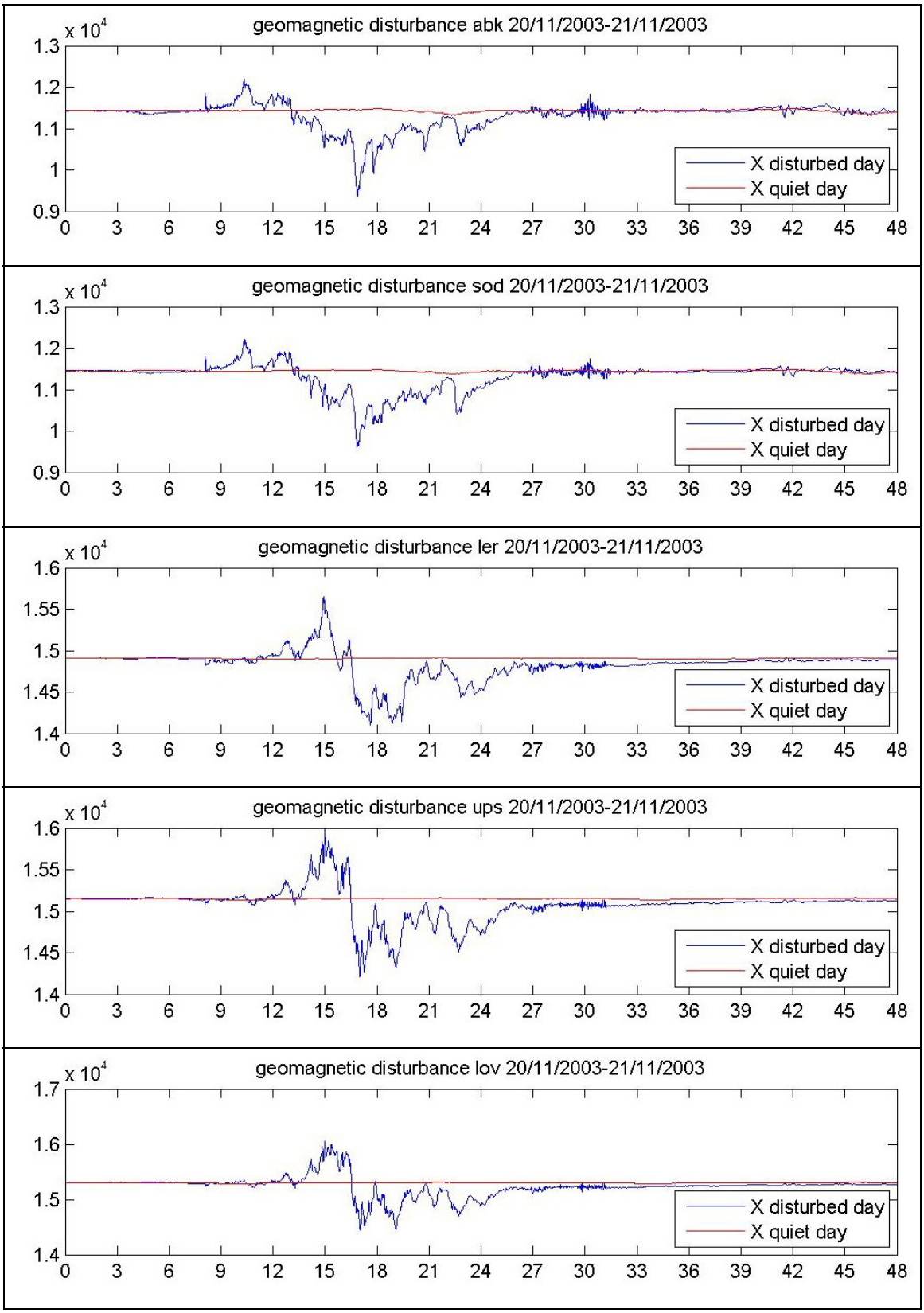

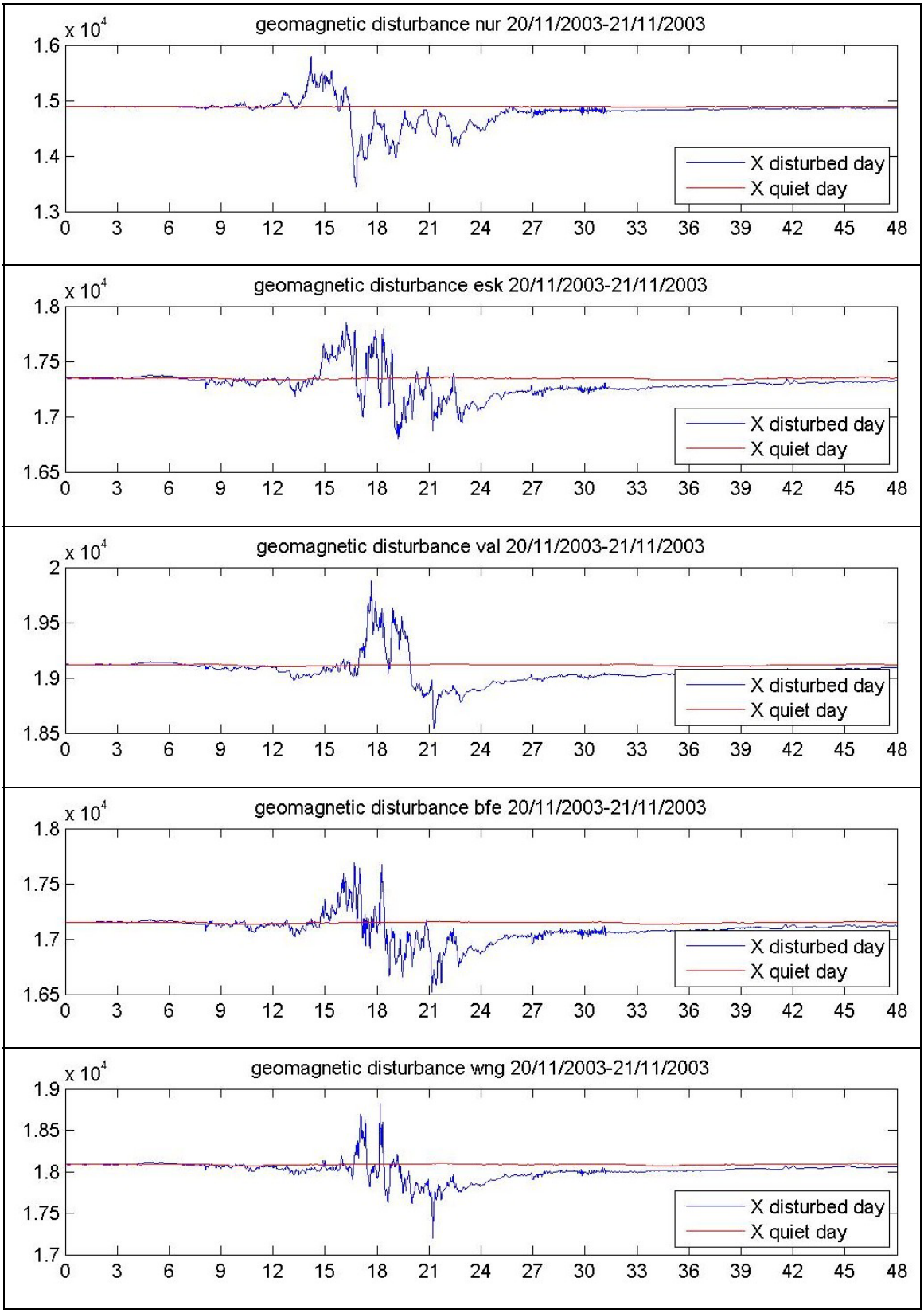
geomagnetic disturbance nur 20/11/2003-21/11/2003
x 10^4
1.6
1.5
1.4
1.3
0 3 6 9 12 15 18 21 24 27 30 33 36 39 42 45 48
X disturbed day
X quiet day
geomagnetic disturbance esk 20/11/2003-21/11/2003
x 10^4
1.8
1.75
1.7
1.65
0 3 6 9 12 15 18 21 24 27 30 33 36 39 42 45 48
X disturbed day
X quiet day
geomagnetic disturbance val 20/11/2003-21/11/2003
x 10^4
2
1.95
1.9
1.85
0 3 6 9 12 15 18 21 24 27 30 33 36 39 42 45 48
X disturbed day
X quiet day
geomagnetic disturbance bfe 20/11/2003-21/11/2003
x 10^4
1.8
1.75
1.7
1.65
0 3 6 9 12 15 18 21 24 27 30 33 36 39 42 45 48
X disturbed day
X quiet day
geomagnetic disturbance wng 20/11/2003-21/11/2003
x 10^4
1.9
1.85
1.8
1.75
1.7
0 3 6 9 12 15 18 21 24 27 30 33 36 39 42 45 48
X disturbed day
X quiet day

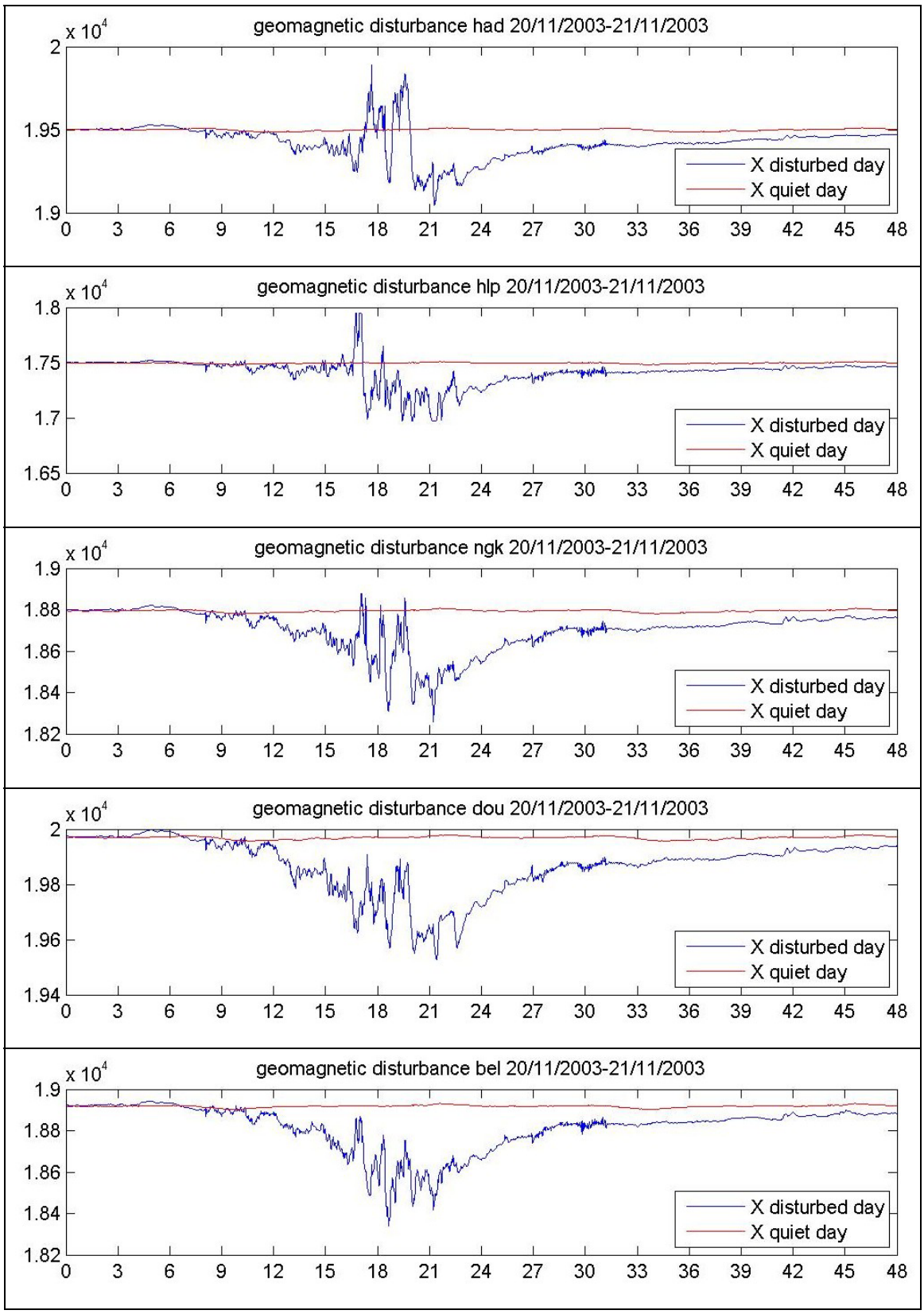
geomagnetic disturbance had 20/11/2003-21/11/2003
x 10^4
2
1.95
1.9
0 3 6 9 12 15 18 21 24 27 30 33 36 39 42 45 48
X disturbed day
X quiet day
geomagnetic disturbance hlp 20/11/2003-21/11/2003
x 10^4
1.8
1.75
1.7
1.65
0 3 6 9 12 15 18 21 24 27 30 33 36 39 42 45 48
X disturbed day
X quiet day
geomagnetic disturbance ngk 20/11/2003-21/11/2003
x 10^4
1.9
1.88
1.86
1.84
1.82
0 3 6 9 12 15 18 21 24 27 30 33 36 39 42 45 48
X disturbed day
X quiet day
geomagnetic disturbance dou 20/11/2003-21/11/2003
x 10^4
2
1.98
1.96
1.94
0 3 6 9 12 15 18 21 24 27 30 33 36 39 42 45 48
X disturbed day
X quiet day
geomagnetic disturbance bel 20/11/2003-21/11/2003
x 10^4
1.9
1.88
1.86
1.84
1.82
0 3 6 9 12 15 18 21 24 27 30 33 36 39 42 45 48
X disturbed day
X quiet day

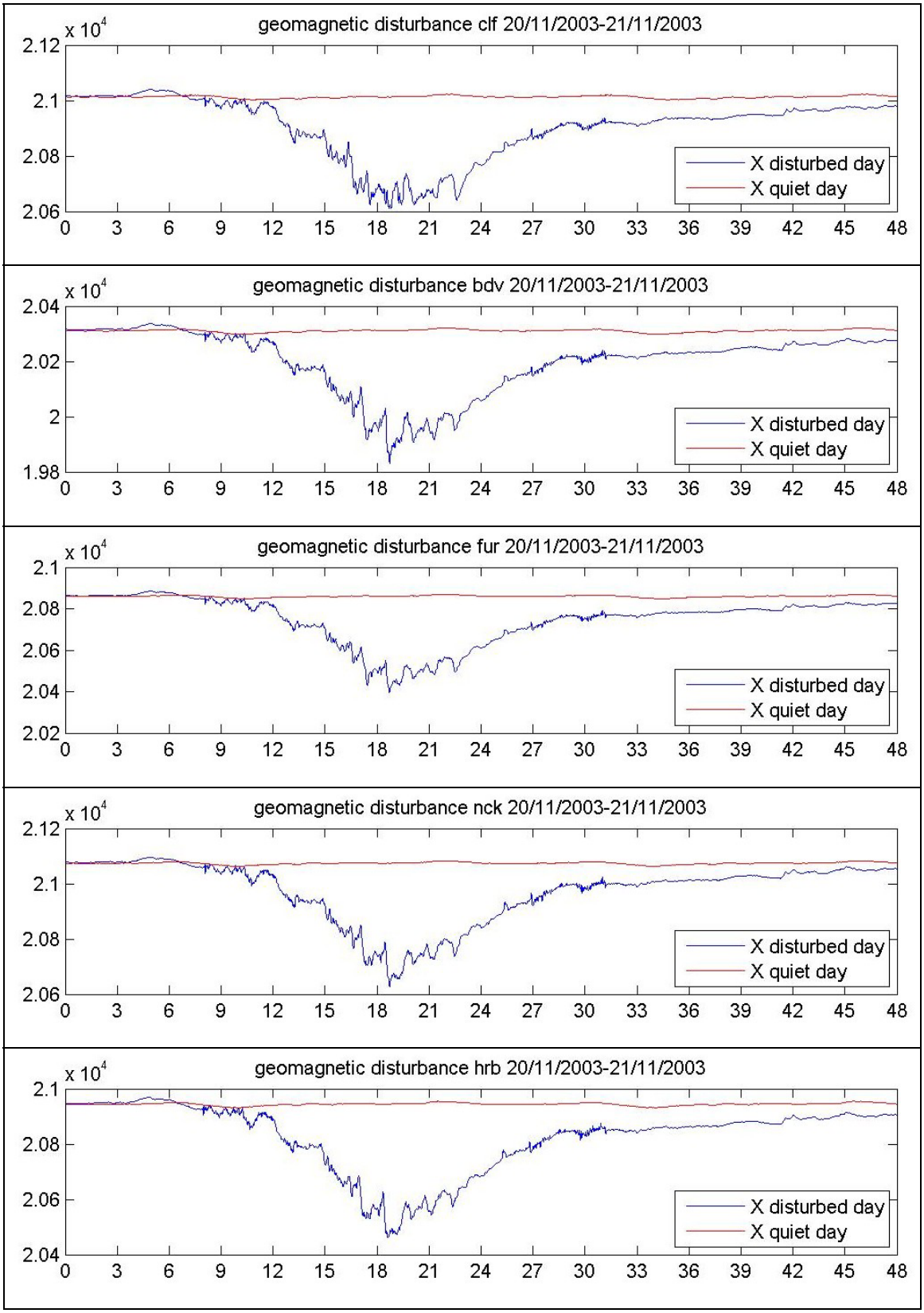
geomagnetic disturbance clf 20/11/2003-21/11/2003
x 10^4
2.12
2.1
2.08
2.06
0 3 6 9 12 15 18 21 24 27 30 33 36 39 42 45 48
X disturbed day
X quiet day
geomagnetic disturbance bdv 20/11/2003-21/11/2003
x 10^4
2.04
2.02
2
1.98
0 3 6 9 12 15 18 21 24 27 30 33 36 39 42 45 48
X disturbed day
X quiet day
geomagnetic disturbance fur 20/11/2003-21/11/2003
x 10^4
2.1
2.08
2.06
2.04
2.02
0 3 6 9 12 15 18 21 24 27 30 33 36 39 42 45 48
X disturbed day
X quiet day
geomagnetic disturbance nck 20/11/2003-21/11/2003
x 10^4
2.12
2.1
2.08
2.06
0 3 6 9 12 15 18 21 24 27 30 33 36 39 42 45 48
X disturbed day
X quiet day
geomagnetic disturbance hrb 20/11/2003-21/11/2003
x 10^4
2.1
2.08
2.06
2.04
0 3 6 9 12 15 18 21 24 27 30 33 36 39 42 45 48
X disturbed day
X quiet day

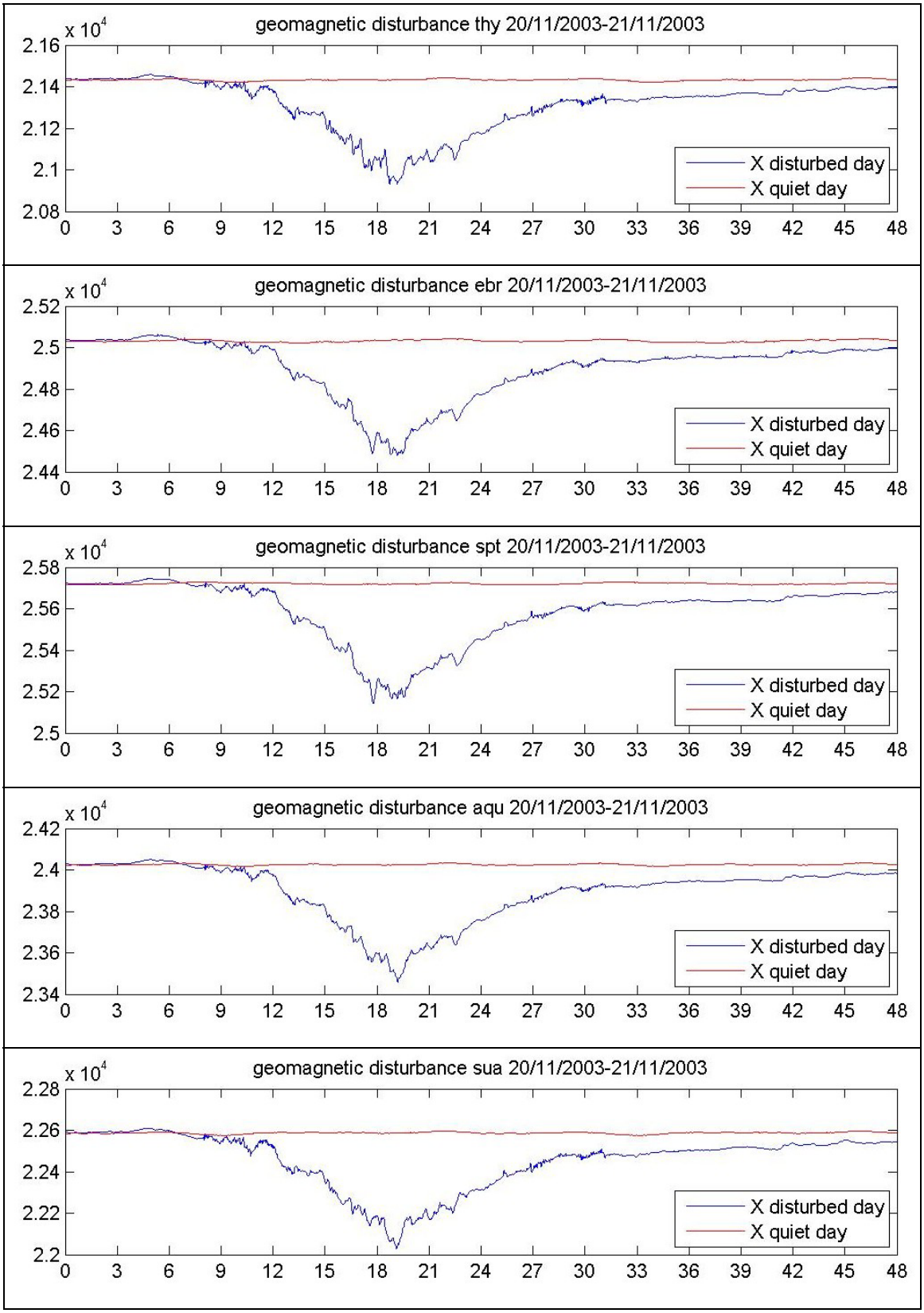
geomagnetic disturbance thy 20/11/2003-21/11/2003
x 10^4
2.16
2.14
2.12
2.1
2.08
0 3 6 9 12 15 18 21 24 27 30 33 36 39 42 45 48
X disturbed day
X quiet day
geomagnetic disturbance ebr 20/11/2003-21/11/2003
x 10^4
2.52
2.5
2.48
2.46
2.44
0 3 6 9 12 15 18 21 24 27 30 33 36 39 42 45 48
X disturbed day
X quiet day
geomagnetic disturbance spt 20/11/2003-21/11/2003
x 10^4
2.58
2.56
2.54
2.52
2.5
0 3 6 9 12 15 18 21 24 27 30 33 36 39 42 45 48
X disturbed day
X quiet day
geomagnetic disturbance aqu 20/11/2003-21/11/2003
x 10^4
2.42
2.4
2.38
2.36
2.34
0 3 6 9 12 15 18 21 24 27 30 33 36 39 42 45 48
X disturbed day
X quiet day
geomagnetic disturbance sua 20/11/2003-21/11/2003
x 10^4
2.28
2.26
2.24
2.22
2.2
0 3 6 9 12 15 18 21 24 27 30 33 36 39 42 45 48
X disturbed day
X quiet day

References

Allen, J., L. Frank, H. Sauer and P. Reiff (1989). Effects of the March 1989 solar activity, EOS (ISSN 0096-3941), vol. 70, Nov. 14, 1989, p. 1479, 1486-1488.

Blanch, E., D. Altadill, J. Boska, D. Buresova and M. Hernández-Pajares (2005). November 2003 event: effects on the Earth's ionosphere observed from ground-based ionosonde and GPS data, Annales Geophysicae, 23, 3027-3034.

Brown, G.M. and R. Wynne (1967). Solar daily disturbance variations in the lower ionosphere, Planet. Space Sci., 15, 1677–1686.

Brunini, C., A. Meza, F. Azpilicueta, M.A Van Zele, M. Gende and A. Díaz (2004). A new ionosphere monitoring technology based on GPS, Astrophysics and Space Science, 290, 415-429.

Buonsanto, M.J. (1999). Ionospheric storms – A review, Space Sci. Rev., 88, 563-601.

Burns, A.G., T.L. Killeen and G.R Carignan (1995). Large enhancements in the O/N2 ratio in the evening sector of the winter hemisphere during geomagnetic storms, J. Geophys. Res., 100, 14 661–14 671.

Danilov, A.D. (2001). F2-region response to geomagnetic disturbances, J. Atmos. Sol.-Terr. Phys., 63, 441-449.

Danilov, A.D. and J. Lastovicka (2001). Effects of geomagnetic storms on the ionosphere and atmosphere, International Journal of Geomagnetism and Aeronomy, vol. 2, n. 3, 209-224.

Davis, K. (1990). Ionospheric Radio, Institution of Electrical Engineers electromagnetic waves series 31, Peter Perengrinus Ltd., London, United Kingdom.

Dungey, J.W. (1961). Interplanetary magnetic field and the auroral zones, Phys. Rev. Lett., 6, 47–48.

Ebihara, Y., M.-C. Fok, S. Sazykin, M.F. Thomsen, M.R. Hairston, D.S. Evans, F.J. Rich and M. Ejiri (2005). Ring current and the magnetosphere-ionosphere coupling during the superstorm of 20 November 2003, J. Geophys. Res., 110, A09S22, doi: 10.1029/2004JA010924.

Fuller-Rowell, T.J., M.V. Codrescu, R.J. Moffett and S. Quegan (1994). Response of the thermosphere and ionosphere to geomagnetic storms, J. Geophys. Res., 99, 3893-3914.

Fuller-Rowell, T.J., M.V. Codrescu, H. Rishbeth, R.J. Moffett, S. Quegan (1996). On the seasonal response of the thermosphere and ionosphere to geomagnetic storms, J. Geophys. Res., 101,n. A2, 2343-2353.

Gombosi, T.I. (1998). Physics of the Space Environment, Cambridge Atmospheric and Space Science Series, Cambridge University Press, Cambridge, United Kingdom.

Hargreaves, J.K. (1992). The solar-terrestrial environment, Cambridge atmospheric and space science series, Cambridge University Press, Cambridge, United Kingdom.

Hernandez-Pajares, M., J.M. Juan and J. Sanz (1999). New approaches in global ionospheric determination using ground GPS data, J. Atmos. Sol.-Terr. Phys., 61, 1237–1247.

Hernandez-Pajares, M., J.M. Juan and J. Sanz (2002). Improving the real-time ionospheric determination from GPS sites at Very Long Distances over the Equator, J. Geophys. Res., 107, 1296–1305.

Huang, C.-S. and J.C. Foster (2005). Long-duration penetration of the interplanetary electric field to the low-latitude ionosphere during the main phase of magnetic storms, J. Geophys. Res., 110, A11309, doi: 10.1029/2005JA011202.

Huang, C.-S., J.C. Foster, L.P. Goncharenko, P.J. Erickson, W. Rideout and A.J. Coster (2005). A strong positive phase of ionospheric storms observed by the Millstone Hill incoherent scatter radar and global GOS network, J. Geophys. Res., 110, A06303, doi: 10.1029/2004JA010865.

Huang, X. and B.W. Reinisch (1996). Vertical electron density profiles from the Digisonde network, Adv. Space Res., 18, 6, 21–29.

Iijima T. and T.A. Potemra (1978). Large-scale characteristics of field-aligned currents associated with substorms, J. Geophys. Res., 83,599.

Juan, J.M, A. Rius, M. Hernández-Pajares and J. Sanz (1997). A two-layer model of the ionosphere using Global Positioning System data, Geophysical Research Letters, 24,n. 4, 393-396.

Kamei, R., M. Sugiura and T. Araki (1989). Provisional Auroral Electrojet Indices (AE 11) for March 1989, WDC-C2 for Geomagnetism, Kyoto, Japan.

King, G. A.M. (1962). The night E-layer, in: “Ionospheric Sporadic E”, edited by: Smith, E. K. and Matsushita, S., 219–231, Pergamon Press, Oxford, UK.

Kivelson, M.G. and C.T. Russel (1995). Introduction to Space Physics, Cambridge University Press, Cambridge, United Kingdom.

Lastovicka, J. (2002). Monitoring and forecasting of ionospheric space weather-effects of geomagnetic storms, J. Atmos. Sol.-Terr. Phys., 64, 697-705.

Lyons, L.R. and A.D. Richmond (1978). Low-latitude E region ionization by energetic ring current particles. J. Geophys. Res., 83, 2201– 2204.

Mandea, M. and B. Langlais (2002). Observatory crustal magnetic biases during MAGSAT and Orsted satellite mission, Geophysical Research Letters, vol. 29, n. 15, 10.1029/2001GL013693,.

Mansilla, G.A. (2004). Mid-latitude ionospheric effects of a great geomagnetic storm, J. Atmos. Sol.-Terr. Phys., 66, 1085-1091.

Maus, S. and H. Lühr (2005). Signature of the quiet-time magnetospheric magnetic field and its electromagnetic induction in the rotating Earth, Geophys. J. Int., 162, 755-763, doi: 10:1111/j.1365-246X.2005.02691.x.

Maus, S., M. Rother, C. Stolle, W. Mai, S. Choi, H. Lühr, D. Cooke and C. Roth (2006). Third generation of the Postdam Magnetic Model of the Earth (POMME), Geochemistry Geophysics Geosystems, vol. 7, n. 7, doi: 10:1029/2006GC001269.

Merrill, R.T., M.W. McElhinny and P.L. McFadden (1996). The Magnetic Field of the Earth: Paleomagnetism, the Core, and the Deep Mantle, International Geophysics Series, Academic Press, San Diego, CA, USA.

Parkinson, W.D. (1983). Introduction to Geomagnetism, Scottish Academic Press, Edinburgh.

Phillips, K.J.H. (1992). Guide to the Sun, Cambridge University Press, Cambridge, United Kingdom.

Popov, V.A, V.O. Papitashvili and J.F. Watermann (2001). Modelling of equivalent ionospheric currents from meridian magnetometer chain data, Earth Planets Space, 53, 129–137.

Prölss, G.W. (1993). On explaining the local time variation of ionospheric storm effects, Ann. Geophys., 11, 1.

Prölss, G.W. (1995). Ionospheric F-Region Storms, Handbook of Atmospheric Electrodynamics, vol. 2 (ed. Volland), CRC Press/Boca Rato, 195-248.

Prölss, G.W. (2004). Physics of the Earth's Space Environment, Springer-Verlag, Berlin, Germany.

Reinisch, B.W. and X. Huang (2001). Deducing topside profiles and total electron content form bottomside ionograms, Adv. Space Res., 27, 23–30.

Richmond A.D. and J.P. Thayer (2000). Ionospheric Electrodynamics: A Tutorial, In: Magnetospheric Current Systems, Geophysical Monograph 118, AGU, pp131-146.

Sabaka, T.J., N. Olsen and M. Purucker (2004). Extending comprehensive models of the Earth's magnetic field with Ørsted and CHAMP, Geophys. J. Int. 159(2), 521-547.

Scherer, K., H. Fichtner, B. Heber, and U. Mall (2005). Space Weather. The Physics Behind a Slogan. Springer-Verlag, Berlin, Germany.

Space Weather Observation, Research and Distribution (2006). Student team project final report, Master Program 2006, International Space University, Strasbourg.

Tinsley, B.A. (1979). Energetic neutral atom precipitation during magnetic storms: Optical emission, ionization, and energy deposition at low and middle latitudes. J. Geophys. Res., 84, 1855– 1864.

U.R.S.I. (1978). Handbook of ionogram interpretation and reduction, edited by: Piggott, W. R. and Rawer, K., WDC A, National Academy of Sciences, Washington, D. C., USA.

U.R.S.I. (1986). Manual of ionogram scaling, Revised Edition, edited by: Wakai, N., Ohyama, H., and Koizumi, T., Radio Research Laboratory, Japan.

World Data Center for Geomagnetism, Kyoto (2005). Data Catalogue No. 27, Feb.

Internet Resources

ACE Science Center (solar wind data),
http://www.srl.caltech.edu/ACE/ASC/

CIRES University of Colorado (ionospheric conductivity tutorial),
http://geomag.colorado.edu/geomagTutorials/Maus_ionospheric_conductivity.pdf

Danish Meteorological Institute Atmosphere Space Research Division (equivalent ionospheric currents),
http://web.dmi.dk/projects/chain/

Germany's National Research Centre for Geosciences (POMME3 software),
http://www.gfz-potsdam.de/pb2/pb23/SatMag/pomme3.html

Goddard Space Flight Center Space Physics Data Facility (Interplanetary Magnetic Field data),
http://omniweb.gsfc.nasa.gov

Institute of Atmospheric Physics ASCR (Pruhonice ionosonde data),
http://www.ufa.cas.cz/

Instituto Nacional de Técnica Aeroespacial (El Arenosillo ionosonde data),
http://www.inta.es/iono/

INTERMAGNET (geomagnetic data),
http://www.intermagnet.org/

International GNSS Service,
http://igscb.jpl.nasa.gov/

International Service of Geomagnetic Indices (Ap, Dst indices),
http://isgi.cetp.ipsl.fr/

MIT Haystack Observatory,
http://www.haystack.mit.edu/

National Geophyical Data Center (Est, Ist indices),
ftp://ftp.ngdc.noaa.gov/STP/GEOMAGNETIC_DATA/ INDICES/EST_IST/

Observatori de l'Ebre,
http://www.obsebre.es/

Sodankylä Geophysical Observatory (Sodankylä ionosonde data),
http://www.sgo.fi/Data/Ionosonde/ionData.php

Space Environment Center data (GOES satellite data),
http://sec.noaa.gov/Data/

Space Weather (aurora gallery),
http://www.spaceweather.com

University of Massachusetts Lowell Center for Atmospheric Research (ionosonde data and ionogram editing tools),
http://umlcar.uml.edu/

World Data Center C1 data (Chilton ionosonde data),
ftp://wdcc1.bnsc.rl.ac.uk/

World Data Center for Geomagnetism Kyoto (AU, AL, SYM-H indices and geomagnetic coordinates),
http://swdcwww.kugi.kyoto-u.ac.jp/index.html

Appendix A. Main ionospheric parameters

fmin	The lowest frequency of reflection wave recorded in the ionogram
foE	Critical frequency of the E region
h’E	Minimum virtual height of the E region
foEs	Critical frequency of the sporadic E layer
h'Es	Minimum virtual height of the sporadic E layer
fbEs	Blanketing frequency of the Es layer: frequency at which the Es layer first allows reflections from upper layers
foF1	Critical frequency of the F1 layer
h'F	Minimum virtual height of the F region. h'F=h’F1 in the daytime
h'F2	Minimum virtual height of the F2 layer. h'F2=h’F in the nighttime
foF2	Critical frequency of the F2 layer
hmF2	Virtual height of the maximum electron density
TEC	Total Electron Content. The integral with height of the ionospheric electron density profile
MUF(D)	Maximum Frequency Usable for ground distance D

Appendix B. Ionospheric stations coordinates

Station	Code	Geographic		Geomagnetic*	
		Lat.	Long.	Lat.	Long.
Athens	AT138	37.86	23.45	36.4	102.9
Chilton	RL052	51.53	-0.62	53.7	84.4
Dourbes	DB049	50.12	4.57	51.5	88.9
El Arenosillo	EA036	37.13	-6.7	40.8	72.8
San Vito	VT139	40.6	17.75	39.9	98.2
Juliusruh	JR055	54.61	13.39	54.2	99.6
Sodankylä	SGO	67.4	26.6	63.9	120.
Tromsø	TR169	69.6	19.29	67.1	116.4
Průhonice	PQ052	49.99	14.6	49.5	98.5

* Geomagnetic dipole coordinates (2005.0) obtained from World Data Center for Geomagnetism, Kyoto, Data Catalogue.

Appendix C. Magnetic observatories coordinates

Observatory	Code	Geographic		Geomagnetic*	
		Lat.	Long.	Lat.	Long.
Abisko	ABK	68.36	18.82	66.06	114.66
L'Aquila	AQU	42.38	13.32	42.42	94.5
Budkov	BDV	49.08	14.02	48.76	97.61
Belsk	BEL	51.84	20.79	50.23	105.17
Brorfelde	BFE	55.63	11.67	55.45	98.48
Chambon la Forêt	CLF	48.02	2.27	49.84	85.69
Dourbes	DOU	50.1	4.6	51.43	88.9
Ebre	EBR	40.82	0.49	43.18	81.31
Eskdalemuir	ESK	55.32	-3.2	57.8	83.75
Fuerstenfeldbruck	FUR	48.17	11.28	48.38	94.61
Hartland	HAD	51.0	-4.48	53.88	80.16
Hel	HLP	54.61	18.82	53.23	104.62
Hurbanovo	HRB	47.86	18.19	46.87	101.1
Lerwick	LER	60.13	-1.18	61.98	88.98
Lovo	LOV	59.34	17.82	57.9	106.38
Nagycenk	NCK	47.63	16.72	46.9	99.62
Niemegk	NGK	52.07	12.68	51.88	97.64
Nurmijarvi	NUR	60.51	24.66	57.87	113.17
Sodankylä	SOD	67.37	26.63	63.93	120.0
San Pablo-Toledo	SPT	39.55	-4.35	42.79	75.98
Surlari	SUA	44.68	26.25	42.39	107.57
Tihany	THY	46.9	17.89	45.99	100.47
Uppsala	UPS	59.9	17.35	58.5	106.29
Valentia	VAL	51.93	-10.25	55.79	74.63
Wingst	WNG	9.07	53.74	54.12	95.0

* Geomagnetic dipole coordinates (2005.0) obtained from World Data Center for Geomagnetism, Kyoto, Data Catalogue.

Appendix D.

Annales Geophysicae, 23, 3027–3034, 2005
SRef-ID: 1432-0576/ag/2005-23-3027

Annales Geophysicae

November 2003 event: effects on the Earth's ionosphere observed from ground-based ionosonde and GPS data

E. Blanch[1], D. Altadill[1], J. Boška[2], D. Burešová[2], and M. Hernández-Pajares[3]

[1]Observatori de l'Ebre, URL – CSIC, Roquetes, Spain
[2]Institute of Atmospheric Physics, Academy of Sciences CR, Prague, Czech Republic
[3]Technical University of Catalonia, UPC/gAGE, Barcelona, Spain

Received: 9 February 2005 – Revised: 2 September 2005 – Accepted: 22 September 2005 – Published: 22 November 2005

Part of Special Issue "1st European Space Weather Week (ESWW)"

Abstract. Intense late-cycle solar activity during October and November 2003 produced two strong geomagnetic storms: 28 October–5 November 2003 (October) and 19–23 November 2003 (November); both reached intense geomagnetic activity levels, K_p=9, and K_p=8+, respectively. The October 2003 geomagnetic storm was stronger, but the effects on the Earth's ionosphere in the mid-latitude European sector were more important during the November 2003 storm. The aim of this paper is to discuss two significant effects observed on the ionosphere over the mid-latitude European sector produced by the November 2003 geomagnetic storm, using data from ground ionosonde at Chilton (51.5° N; 359.4° E), Pruhonice (50.0° N; 14.6° E) and El Arenosillo (37.1° N; 353.3° E), jointly with GPS data. These effects are the presence of well developed anomalous storm E_s layers observed at latitudes as low as 37° N and the presence of two thin belts: one having enhanced electron content and other, depressed electron content. Both reside over the mid-latitude European evening sector.

Keywords. Ionosphere (Mid-latitude ionosphere; Ionospheric Disturbances; Particle Precipitation)

1 Introduction

A geomagnetic storm is the most important space weather phenomenon from the point of view of the impact on the global magnetosphere-ionosphere-thermosphere system. The storm is supplied by solar wind energy, captured by the magnetosphere, and transformed and dissipated in the high-latitude upper atmosphere. It affects the complex morphology of the electric fields, winds, temperature and composition, and it causes changes in the state of ionospheric ionization. One of the main characteristics of the disturbed ionosphere is a great degree of variability. Due to many interacting factors, each storm could show a different course. During geomagnetic storms the electron density can either increase (positive ionospheric storm) or decrease (negative ionospheric storm). The electric fields, thermospheric meridional winds, a "composition bulk" and high latitude particle precipitation have been suggested as probable physical mechanisms to explain the ionospheric response to storm-induced disturbances observed at different altitudes and latitudes (Fuller-Rowell et al., 1994; Prölls, 2004). Severe ionospheric disturbances originated by solar flares have significant effects on the propagation of radio waves over the entire radio spectrum, which is crucial for radio communications and navigation systems (Ondoh and Marubashi, 2001; Thomson et al., 2004). Studies of the ionospheric reaction to geomagnetic storms are of great importance and there are numerous publications on the topic (e.g. Buonsanto, 1999; Danilov, 2001; Lastovicka, 2002; Mansilla, 2004; and many others). Nevertheless, many features of this phenomenon are still not clear due to many different processes interacting in the Earth's atmospheric system.

Between 18 October and 5 November of 2003, in a descending phase 11-year solar sunspot cycle, two periods of a suddenly enhanced solar activity, primary caused by two different, large, sunspot groups, occurred. There were eleven large X-class flares during this period. On 28 October 2003, a powerful solar flare X17 erupted from giant sunspot 486. It struck the Earth on 29 October, and was responsible for the 28 October–5 November 2003 geomagnetic storm (also known as the Halloween event). In the middle of November, all sunspots that caused intense space weather effects in October were again visible on the Earth-facing side of the Sun. In this case it was the solar flare X28 coming from sunspot 484 that was responsible for the 19–23 November 2003 geomagnetic storm. The X28 flare has been the largest one since

Correspondence to: E. Blanch
(eblanch@obsebre.es)